Time-lapse fluorescence microscopy of the effects of antimicrobial peptides on single, live *Escherichia coli* cells

By

Nambirajan Rangarajan

A dissertation submitted in partial fulfillment of

the requirements for the degree of

Doctor of Philosophy

(Chemistry)

at the

UNIVERSITY OF WISCONSIN MADISON

2015

Date of final oral examination: 08/24/2015

The dissertation is approved by the following members of the Final Oral Committee:

James C. Weisshaar, Professor, Chemistry

Alessandro Senes, Associate Professor, Biochemistry

Douglas B. Weibel, Professor, Biochemistry

M. Thomas Record, Professor, Chemistry and Biochemistry

Aaron Hoskins, Assistant Professor, Biochemistry

Acknowledgements

Life in graduate school has been a roller coaster ride! I cannot think of a single day that passed without anything new and exciting to learn, discuss and ponder over. Over the years, the experiences I gained within and outside the laboratory go way beyond the chapters of my thesis. A lot of people contributed directly and indirectly to my work and life, and I am deeply grateful to all of them.

I would not have survived graduate school without the support of my advisor, Prof. Jim Weisshaar. Jim accepted me in his group and gave me a great opportunity to pursue research in cell biology and biophysics. Over the years, he has mentored me patiently, giving me all the time I required to learn and always being accessible whenever the need arose. I will always remember Jim's unique ability to absorb knowledge from multiple sources (publications, books, presentations or discussions) and condense it into a cohesive story for himself and his students. His clarity in thought and writing, emphasis on simple narrative to discuss scientific concepts, 'hourglass' styled presentations and above all, the unabashed curiosity about seemingly trivial aspects of data, are a few things I hope to remember and take forward with me. I am truly grateful to Jim for guiding me through graduate school.

Kem Sochacki mentored me during my initial months in the Weisshaar group. She introduced me to experimental protocols, analysis methods, literature reading and discussed open problems in the field. Although Kem graduated soon after I joined and we were out of touch for a few years, we managed to reconnect recently. She has been a great support during my contemplations regarding my next career move. Thanks for everything, Kem!

Ben Bratton and Izzy Smith, Kem's contemporaries, made up the trio of graduating students in the Weisshar group in 2011. Together, these three were a big motivating factor for me to join the group. Renee Dalrymple was a great friend over four years of my graduate career. I am thankful to her for offering help with microscope alignment, advice regarding career choices and, above all, for being a flower-sniffing bulldog! Kenneth Barns was my fellow comrade in the antimicrobial world. From discussing our latest results to questions regarding laser alignment to being the only pair of ears for Ken's wisecracks and one-liners – being office-mates with him meant there was always a funny moment round the corner!

Somenath Bakshi has been a huge inspiration to me. With his zeal for almost everything in life, knowledgeable insights into science and passionate conversations on Indian politics, music, films and photography – Somenath Da enriched my experience in graduate school a lot. Heejun and Wenting have overlapped with me over the past five years in graduate school. Heejun's appetite for science has been bewildering and inspiring at the same time. No conversation with him has passed without me learning something new, in and outside science! Wenting has been a great friend, a helpful colleague and a generous humanitarian who makes sure no hungry soul entering 4225 leaves with an empty stomach! Many thanks to Nikolai, Soni and Zhilin for their company in the group during the last two years. Anurag and Mainak joined the group in 2014. Anurag and I have shared some great times doing science, with a couple of 'Eureka' moments thrown in! Outside the lab, I have the pleasure of hanging out with them, and I wish both the very best for their graduate experience ahead. Enjoy the ride, folks!

Thanks to Prof. Bill Wimley for the opportunity to collaborate on the synthetic antimicrobial peptide project. His group's peptides have proved to be quite productive for me. I also thank Prof. Wimley for supporting my post-doctoral applications.

I am grateful to the faculty members in my thesis committee for their valuable time and feedback during such a crucial phase of my career. Prof. Alessandro Senes has been a valuable mentor for the last five years. What began as an unofficial meeting for some career advice soon developed into formal mentorship when he agreed to join my dissertation committee. More recently, we have started to collaborate on some projects and I hope to take them to fruition. I am grateful for Alessandro's support in my post-doctoral applications and for his generosity in helping me out during tight situations. Thanks, Alessandro! I thank Prof. Doug Weibel for all the help and collaboration I received from him and his group in my research. I also thank Prof. Tom Record and Prof. Aaron Hoskins for taking time out of their busy schedules to guide me during my thesis submission. Prof. John Wright was part of dissertation committee in years 2 and 3 of graduate school and provided crucial mentorship to me, especially during years 1 and 2. I learned the principles of chemical instrumentation, design and control in his amazing Chem 621 class in 2009. Prof. Wright is one of the most inspiring teachers I have had!

The Chemistry department staff has been outstanding with their support and care. Matt, Sue, Stephenie, Teresa, April, Phil, Denis, Mike, Jeff, Alan… the list is endless and I am bound to miss out on a few names. A collective thanks to you all!

I thank all my friends in Madison for their company, support and above all, for providing a home away from home! Together, we have shared the highs and lows of grad school, celebrated special momenths and cared for each other during low phases. Unknowingly, we have become family to each other, and forged bonds that will stay for life. I will always look back fondly to my grad life, and a lot of the credit goes to you guys! Saaz, IGSA – we have had a blast with all those great events, rehearsals, jam sessions and showtimes. I owe you a lot of the fun I had outside lab.

I wouldn't have been able to survive away from India without the constant love, support and understanding of my parents – my idols and my greatest teachers. Thanks, Ma, Pa! As a high school student, I was inspired by my brother Gopi to further study chemistry and biology. So, there you go – it's all your fault, bhai! On a more serious note, I can't help reminiscing about the days when he would explain concepts of biology and physics with such impeccable clarity; and stress on understanding the concepts instead of mere rote learning. I think at least some of that has stuck! Thanks for everything, Gopi! Ania and li'l Z have provided yet another layer of comfort and love and their summer'15 visit made this Madison chapter complete! Thanks also to all my extended family members in the US and India for being there through thick and thin!

My wife, best friend and fellow-grad Rika has enriched my life and work in Madison in all ways possible! Collaborating with her in the sciences and arts has been such a joy. Thanks Rika, for being there always, for understanding me and for completing me! I couldn't have reached here without you. A special mention has to go to Riggles, my pet hamster, for staying up with me whenever I would work late into the night. I am also fortunate to have received the love and support of Rika's parents, Kuku, Tonu and their extended families that's always rooting for our success.

Many thanks to you all!

Table of Contents

List of Figures

Chapter One

Chapter Two

Chapter Three

Chapter Four

Tables

Summary

Antimicrobial peptides (AMPs) are a diverse group of molecules found in the innate immune systems of various organisms. They form the first line of defense against invading pathogens by causing direct microbial killing and by signaling the host immune responses. AMPs are being studied as templates for the development of the next generation of antibiotics. It is crucial to understand how AMPs exert their antimicrobial effects on bacteria. This thesis presents detailed mechanistic insights into the effects of AMPs on single *Escherichia coli* cells. Both natural and artificially engineered AMPs have been studied in this work. The primary method used is time-lapse, widefield fluorescence microscopy.

Chapter 1 provides a brief description of the *E. coli* cell envelope, which is a common theme in this work. Further, this chapter introduces the importance of studying AMPs as templates for novel, potent antibiotic therapies. A brief history of AMP discovery follows. Mechanistic insights obtained from AMP studies on model lipid bilayers and vesicles are highlighted. The need for studying AMPs in biologically relevant conditions is described. In this context, some recent single cell studies of AMPs from our and other research groups are highlighted. This chapter concludes with a brief description of the time-lapse fluorescence microscopy method used in this thesis.

The antimicrobial effects of Cecropin A (AMP found in moths) and LL-37 (a human AMP) are described in Chapter 2. Loss of periplasmic GFP reports on permeabilization of the outer membrane (OM). DNA staining by the dye SYTOX Green reports permeabilization of both the OM and cytoplasmic membrane (CM). Simultaneous measurements of the tip-to-tip cell length are used as a proxy for monitoring cell growth. Both Cecropin A and LL-37 cause

localized permeabilization of the OM and CM within 30 min. Detailed sequence of events, kinetics of permeabilization and estimates of the degree of permeabilization are discussed.

Various research groups have used natural AMPs as templates to develop more potent, synthetic analogs. In Chapter 3, the time-resolved assays previously introduced in Chapter 2 have been used to investigate the antimicrobial action of two synthetic AMPs on *E. coli*. Both AMPs were previously discovered by our collaborators in a high throughput screen for the ability to permeabilize LUVs. The kinetics, spatial patterns of permeabilization and sequence of events caused by these AMPs are described in detail. A new model of cell membrane permeabilization is proposed.

Chapter 4 describes future directions in which the current body of work can be extended. Section 1 of this chapter considers adapting the assays described in chapters 2 and 3 to study AMP action on cells from stationary phase cultures. Modifications to the experimental protocol are suggested and preliminary data is presented. Section 2 proposes a hypothesis to explain the localized membrane permeabilization caused by Cecropin A and LL-37. Section 3 concludes this thesis with a broad discussion about various future explorations that could push this field forward.

While membrane permeabilization is an important effect of AMPs, upon gaining access to the cytoplasmic space, AMPs can affect several downstream targets. To understand the post-permeabilization effects of AMPs, we studied the action of LL-37 and Cecropin A on the spatial distribution of DNA and ribosomes in actively growing cells. This work is described in Appendix 1.

Appendix 2 was prepared for the WISL award for communicating graduate Chemistry research to the public. It aims to describe the importance of this thesis to the general public via a question-answer format.

CHAPTER ONE

Introduction

ABBREVIATIONS

CDC: Centers for Disease Control and Prevention, AMP: Antimicrobial Peptide, mCRAMP: murine Cathelicidin-related Antimicrobial Peptide, ONPG: ortho-Nitrophenyl-β-galactoside, $diSC_3(5)$: 3,3'-Dipropylthiadicarbocyanine iodide, SMAP-29: Sheep Myeloid Antimicrobial Peptide-29, hBD2: human β-Defensin 2, CL: Cardiolipin, PG: Phosphatidylglycerol, MIC: Minimum Inhibitory Concentration, OM: Outer Membrane, CM: Cytoplasmic Membrane, MBC: Minimum Bactericidal Concentration, $HD5_{ox}$: Human Defensin 5 (oxidized), TEM: Transmission Electron Microscopy, EMCCD: Electron Multiplying Charge Coupled Device.

OUTLINE

This introductory chapter comprises three parts. Part 1 describes the structure and composition of the *E. coli* cell envelope, which is a common theme for all chapters in this thesis. Part 2 introduces the field of antimicrobial peptides (AMPs). This part also provides a brief history of AMP research, relevance of AMPs in today's world and mechanistic insights into AMP action. Part 3 provides a short summary of the microscopy technique used for the work described in this thesis.

PART I: THE *E. COLI* CELL ENVELOPE

The cell envelope of *E. coli* consists of three principal layers. Starting from the outside, proceeding inward, these are the outer membrane (OM), peptidoglycan layer and cytoplasmic membrane (CM)[1]. The OM and CM enclose an aqueous compartment known as the periplasm. The peptidoglycan layer is present in the periplasm and is bound to the OM via lipoproteins. The CM encloses the cell cytoplasm, which houses the DNA, ribosomes, proteins, and other ions and solutes. Both the OM and CM are lipid bilayers, however, they differ in the structures of lipids involved. A schematic of the *E. coli* cell envelope is provided in Figure 1.1.

The outer membrane is an asymmetric bilayer consisting of phospholipids in the inner leaflet and glycolipids, mainly lipopolysaccharide (LPS), in the outer leaflet. Additionally, it also contains lipoproteins that are peripherally attached to the inner leaflet; and transmembrane outer membrane proteins (OMPs) that form β-barrel secondary structures. Some of these OMPs such as the porins OmpF and OmpC, allow passive diffusion of ions and hydrophilic solutes smaller than ~600-700 Da.

The Peptidoglycan layer consists of layers of repeating disaccharide units (N-Acetyl muramic acid and N-Acetyl glucosamine) cross-linked by pentapeptide chains. This meshwork arrangement results in a highly rigid layer that withstands the internal turgor pressure of the cell. It also confers shape and rigidity to the cell envelope. Without the peptidoglycan, cells assume a spherical shape, referred to as spheroplasts. New peptidoglycan material is inserted as 'hoops' into the preexisting meshwork at the division septum[2]. Using cryo-TEM, the thickness of the peptidoglycan layers was estimated to be ~6 nm[3].

The cytoplasmic membrane is a symmetric phospholipid bilayer consisting of three major phospholipids: Phosphatidylethanolamine or PE (~80%), Phosphatidylglycerol or PG (~15%)

and Cardiolipin or CL (~5%)[4]. PE is zwitterionic, while PG is anionic (-1 charge). CL is a dimer of PG and carries two negative charges. While PE and PG have one polar head and two tails, CL has two heads and four tails. In *E. coli* cells, lipid chains are synthesized in a wide variety of acyl chains, chain lengths, degree and positions of unsaturation, and presence of cyclopropyl groups.

PART II: ANTIMICROBIAL PEPTIDES

Antibiotic resistance: A global health threat

Since the 1940s, antibiotics have been used to treat patients suffering from life-threatening bacterial infections. Over the last 70 years, these drugs have greatly reduced health concerns posed by infectious diseases. However, excessive use of antibiotics has allowed the target bacteria to adapt and develop resistance. Infections caused by such 'antibiotic-resistant' pathogens are one of the leading causes of disease and death today. In the United States alone, over 2 million people get infected by drug-resistant bacteria annually, and as a result, at least 23,000 die each year[5]. In an assessment of the domestic impact of antibiotic resistant bacteria within the U.S.A., the Centers for Disease Control and Prevention (CDC) classified pathogenic bacteria as *urgent*, *serious* or *concerning* (Table 1.1) based on factors affecting impact and epidemiology (List 1.1). Of these, particularly concerning are infections caused by multi-drug resistant bacteria, which have adapted to most of the potent antibiotics. These 'superbugs' are spreading in hospitals and healthcare facilities across continents at an alarming rate[6], and pose serious challenges to global health. Such infections result in excess health care costs due to prolonged, expensive drug treatments in the range of $20 billion per year[5], and loss of productivity up to $35 billion per year[5].

Although the emergence of antibiotic resistance is a natural phenomenon, it is rapidly accelerated by the excessive and prolonged use of antibiotics in humans and food animals. An antibiotic dose may kill most of the germs in the sample, except a handful of resistant bacteria that contain a resistance gene. Over multiple cell cycles, these 'survivors' are able to proliferate and eventually confer resistance to the entire population.

Historically, resistance to antibiotics emerged in parallel to their discovery, and was addressed by modifying existing antibiotics to produce superior analogs. Development of whole new classes of antibiotics (such as β-lactams, aminoglycosides, fluoroquinolones and tetracyclines) also accelerated the pace of drug development[7]. However, antibiotic discovery has slowed over the last few decades. No new antibiotic families have been introduced since Daptomycin, a membrane-targeting lipopeptide discovered in 1986. It has become clear that antibiotic resistance is fast outpacing drug development efforts. Therefore, it is crucial to explore alternative research platforms to develop more potent drugs. In this context, antimicrobial peptides (AMPs) are promising templates for developing new, improved antibiotic therapies.

Antimicrobial peptides (AMPs): Next-generation antibiotics?

The earliest studies of natural antimicrobial factors were first performed on blood serum and leukocyte extracts in the late nineteenth century[8]. Bactericidal and hemolytic activity were investigated by mixing extracts with blood samples and bacteria to study the thermolability of the antimicrobial/hemolytic action. Between 1920 and 1960, various antimicrobial components were demonstrated to be present in blood (beta-lysin), tissue, mucus (lysozyme)[9] and extracts from phagocytic granules (phagocytin)[10]. However, this overlapped with the discovery of penicillin by Fleming in 1928, and its subsequent development as a therapeutic drug by Howard Florey, Ernst Chain and Norman Heatley in the early 1940s. This ‘Golden Age of Antibiotics’ shifted research interests away from the potential of lysozyme and other host-defense agents. By the 1960s, however, the rise of multidrug resistant pathogens reawakened research efforts on host-defense molecules.

Thionins, distributed widely across the plant family, were one of the earliest antimicrobial peptides to be studied and isolated from natural sources[11]. Originally discovered in 1942, the representative peptide of this family was renamed Plurothionin in the mid-1970s. Antimicrobial components in frog skin (Bombinin), milk (Lactoferrin)[12] and moth larvae[13] were identified in the 1960s. This was soon followed by landmark studies involving isolation and characterization of antimicrobial peptides from insects (Cecropin)[14], frogs (Magainin)[15] and humans (Defensins)[16]. Since then, AMP discovery has progressed rapidly and as of August 2015 more than 2500 natural AMPs have been filed in the Antimicrobial Peptide Database[17,18]. Although AMPs have diverse sequences and structures, they are generally up to 50 amino acids in length, possess high charge (up to +12), are rich in cationic and hydrophobic residues, and form amphipathic structures. The broad structural classes of AMPs are summarized in Table 1.2[19] and examples of secondary structures of some AMPs are provided in Figure 1.2.

AMPs are important for host-defense

Antimicrobial peptides form the first line of defense against invading pathogens in various organisms such as humans, animals, plants, insects and microbes. They are found in neutrophils and macrophages (types of white blood cells), epithelial cells, mucus, saliva, tear, skin, etc. of various organisms[20]. In addition to direct microbial killing, AMPs have been found to modulate host immune responses at physiological conditions[21].

In humans, white blood cells deficient in secretory granules and prone to severe bacterial infections were shown to lack Defensins and related Serine proteases that were responsible for formation of mature AMPs[22]. In mice, Defensins and Cathelicidins have been shown to be important for host defense against *Salmonella Typhimurium* infections (rod-shaped gram-

negative bacteria, causative agent of Typhoid fever). Mice deficient in proteases essential for processing intestinal α-Defensins and mCRAMP; and macrophages lacking mCRAMP were found to be hypersusceptible to *S. typhimurium* infections[23,24].

Studies of AMPs in lipid bilayers and vesicles

Since bacterial membranes pose a physical barrier for AMP entry into cells, studying AMP-membrane interactions is crucial to understanding their antimicrobial action. There is a rich history of biophysical studies of the effects of AMPs on the membrane integrity of lipid bilayers and vesicles[19]. Lipids are chosen keeping in mind the overall charge on the bilayer/vesicle membrane – anionic for mimicking bacterial cytoplasmic membranes and zwitterionic to resemble eukaryotic membranes. The overall charge on the vesicle membrane modulates the initial binding of cationic AMPs. The interaction between AMPs and model lipid membranes can be described as a two-step process:

Binding. The initial attraction and binding of AMPs to bacterial cell surfaces is mediated by electrostatic interactions. Various physicochemical factors may govern the orientation of membrane-bound peptide molecules; such as temperature, extent of hydration of the bilayer, nature of lipid headgroups, bilayer thickness; and peptide charge distribution and hydrophobicity. Among the most important factor governing peptide orientation is the peptide concentration at the bilayer surface[25]. At low peptide:lipid ratio, the AMP molecules are oriented parallel to the bilayer axis. The amphipathicity of secondary structures adopted by AMPs allows the hydrophobic and charged portions to mix with the lipid tails and headgroups of the bilayer, respectively.

Insertion. As more AMP molecules associate with the bilayer surface, the peptide: lipid ratio increases. Above a critical value, which varies with the AMP and lipid composition of the bilayer[26], peptide molecules begin to re-orient perpendicular to the bilayer axis. This change in orientation of the majority of bound AMP molecules at low and high surface concentrations has been observed in oriented circular dichroism studies[27]. In this perpendicular orientation, AMPs insert themselves into the bilayer to permeabilize the membrane via transmembrane pores or channels. Neutron in-plane and off-plane scattering has been used to detect and estimate the sizes of transmembrane pores[28,29].

There are two structural models of 'pores' formed by AMPs in lipid bilayers and vesicles. In the 'barrel-stave' model, AMP molecules associate to form a bundle with a central water channel, like a barrel with AMP molecules as staves. Although initially thought as the prototype of peptide-induced pores, it is now accepted that only Alamethicin (AMP from the fungus *Trichoderma viride*)[25] forms pores of this geometry. Alamethicin is a 20-residue peptide, has only one charged residue (Glu-18), and carries a net neutral charge (when the C-terminal is amidated) at physiological pH. Using oriented circular dichroism, neutron scattering and synchrotron-based X-ray scattering, it has been shown that 5-10 Alamethicin molecules form a barrel-stave pore with inside and outside diameters of ~1.8 nm and ~4.0 nm, respectively[30].

In the 'toroidal pore' model, polar faces of AMP molecules associate with anionic lipid head groups, causing them to tilt from their usual orientation parallel to the lamellar normal of the bilayer. A continuous bend re-orientation of the lipid molecules is formed, resulting in a pore lined by the inserted peptide molecules and re-orientated lipid head groups. As opposed to the barrel-stave pore in which adjacent AMP molecules interact laterally with one another and use the lipid bilayer as a template for self-assembly, the toroidal pore model involves the disruption

of normal segregation of polar heads and non-polar tails of lipids molecules within the bilayers. This model has been invoked for membrane active peptides such as Melittin (bee venom peptide, 26-residue, +5 charge) and Magainin 2 (found in frog skin, 23-residue, +6 charge). It is thought that the toroidal pore may be preferred by highly cationic AMPs due to charge shielding by intervening anionic head groups. Such screening would be absent from barrel-stave pores, which may be favored by neutral AMPs like Alamethicin.

Additionally, there are other AMP-bilayer combinations wherein permeabilization has been observed without strong evidence for finite pores. Various terms such as 'carpet model', 'detergent model' and 'sinking-raft model' have been used to classify such interactions. These serve more to provide convenient terminology than a molecular level understanding of the membrane disruption. It is important to note that AMPs can also cause other perturbations such as vesicle aggregation, vesicle fusion, formation of non-bilayer phases, lipid 'flip-flop' (trans-bilayer exchange of lipids), and complete solubilization of membranes. The wide variety of experimental conditions used by various research groups (choice of lipids, degree of bilayer hydration, temperature, peptide:lipid ratios and buffer conditions) has made it difficult to directly compare results from such studies.

Lack of correlation between membrane permeabilization and antimicrobial action

While investigations of AMP efficacy on lipid vesicles and bilayers have yielded detailed insights into the mechanisms of membrane permeabilization, the biological relevance of these results is not certain. Recent studies have found a lack of correlation between vesicle permeabilization and antimicrobial potency[31]. By iteratively screening large peptide libraries for solubility and for LUV permeabilizing activity, highly potent membrane permeabilizing peptides

were identified. The most active hits from the second round of screening showed a 20-fold increase in the ability to permeabilize vesicles, as compared to the consensus sequence from the first round of screening. However, only negligible improvements were observed in antimicrobial potency. The degree of correlation between LUV-permeabilizing and antimicrobial activities is still unclear. Hence, it is important to complement vesicle-based screens with antimicrobial assays on live bacterial cultures, to realize the eventual goal of developing potent, broad-spectrum antibiotic lead compounds.

Studies of AMPs in bacterial cell cultures

Membrane permeabilization to dye molecules. AMP effects on the membrane integrity of bacterial cells have been studied using various cell-based spectrophotometric assays. The ML-35p strain of *E. coli* was specifically constructed to monitor permeabilization of the inner and outer membranes[32]. This strain contains a periplasmic β-lactamase encoded on a plasmid. Additionally, it contains chromosomally expressed cytoplasmic β-galactosidase. The membranes pose barriers to the entry of chromogenic reporter molecules to the periplasm and cytoplasm. Nitrocefin, a chromogenic cephalosporin, can access the periplasmic space only after permeabilization of the outer membrane. Upon entering the periplasm, it gets cleaved by β-lactamase to yield a chromophore that absorbs at 486 nm. Similarly, the cytoplasmic membrane permeabilization is monitored with another pro-chromophore. This strain is deficient in lactose permease. Therefore, it cannot transport substrates of β-galactosidase across intact membranes. To monitor permeabilization of both the outer and cytoplasmic membranes, this assay uses ortho-Nitrophenyl- β-galactoside (ONPG), a pro-chromophore. Once both membranes are

disrupted and ONPG gets into the cytoplasm, it gets cleaved by β-galactosidase to ortho-Nitrophenol, which absorbs at 420 nm.

Membrane permeabilization to K^+ ions. Another consequence of membrane disruption in cells is equilibration of ions such as K^+ and H^+ across the cytoplasmic membranes. These species contribute to the net proton-motive force that is essential for cellular homeostasis. K^+ release from the cytoplasm of *E. coli* cells has been monitored in real time directly by using K^+ sensitive electrodes[33,34], and indirectly by monitoring the fluorescence of $diSC_3(5)$, a membrane potential sensitive dye[34,35]. This dye partitions into cells with intact membrane potential and its fluorescence is quenched at intracellular concentrations. If the AMP permeabilizes the cytoplasmic membrane, the dye is released to the surrounding medium causing an increase in the total fluorescence of the suspension. Using these methods, it has been shown that AMPs such as Protegrin-1 (porcine leukocytes) and SMAP-29 (ovine leukocytes) cause partial release of K^+ within 5 minutes, and the extent of release increases with the bulk peptide concentration[33].

Other antimicrobial symptoms. Upon entry into the cytoplasm, AMPs can affect various cellular processes such as biosynthesis of peptidoglycan and the cell wall[36], nucleic acids and proteins, DNA replication and ATP synthesis[19] . In some cases, these effects are caused without extensive damage to the cytoplasmic membrane[37]. Certain [R,W]-rich, cationic AMPs accumulate in cell membranes and cause depolarization, inhibit cellular respiration and delocalize essential membrane proteins without detectable membrane permeabilization[38].

Single-cell snapshots of antimicrobial action of AMPs

While the above mentioned bulk antimicrobial assays on bacterial cells provide detailed insights into the various effects of AMP, they suffer from population averaging of the readout,

which is measured on a suspension containing millions of cells. A bacterial culture contains millions of cells that respond to the AMP treatment on their individual, independent timescales. Therefore, the individual responses are expected to be widely heterogeneous. By collectively measuring the output from all the cells in a sample simultaneously and attributing a single readout value, the diversity in cell response is blurred out. In contrast to bulk measurements, single cell imaging methods enable us to monitor the behavior of individual cells without ensemble averaging of data. In the context of AMP studies, such methods have provided rich, spatially resolved data. In this section, some recent works using single cell measurements for AMP studies are discussed.

Using a combination of fluorescence microscopy on living cells, and immunoelectron and immunofluorescence microscopy on permeabilized cells; it has been shown that Human β-Defensin 2 (hBD2) binds to the cell membranes of *Enterococcus faecalis* cells at discrete foci[39]. This interaction also disrupts the regular localization of enzymes essential for secretion (SecA, ATP-binding translocase) and attachment (SrtA, sortase) of cell-surface proteins. In another study, fluorescently labeled Bacteriocin protein (BacL1), a bacterial antimicrobial protein, was shown to localize specifically to cell division sites and induce lysis in actively dividing *E. faecalis* cells[40]. The nascent septum is enriched in anionic phospholipids such as Cardiolipin (CL) and Phosphatidylglycerol (PG), and might cause AMPs to bind and localize specifically to these sites[4]. There is some evidence that short, highly cationic AMPs rich in Arginine residues might be preferentially interacting with membrane domains rich in anionic phospholipids[41].

While such approaches have provided detailed insights into the mechanism of AMP action, most of them involve recording static snapshots, and fail to provide information on how the observed symptoms evolve over time. The limited temporal resolution of these methods

assumes significance in the present discussion since AMP effects have been observed within a few seconds or minutes of mixing AMPs with cells (or vesicles)[42–44].

Time-lapse, single cell imaging of AMP effects in bacteria

Observing AMP effects on single, living cells in real time provides a detailed view of antimicrobial symptoms with high spatiotemporal resolution. Time lapse imaging of antimicrobial effects has been widely used to study anti-fungal peptides, probably owing to the larger size of fungal cells and their non-motile nature[45]. Live cell imaging of AMP effects in bacteria is a more recent, growing field. Table 1.3 summarizes some recent studies involving time-lapse imaging of AMP action on single, live bacterial cells.

The antimicrobial action of LL-37, the only human cathelicidin AMP, was studied on single *E. coli* cells using two color imaging[46]. To monitor peptide localization on the cells, LL-37 was labeled with a red-fluorescing Rhodamine dye. Outer membrane permeabilization caused by 8 μM LL-37 (MIC = 1-2 μM) was monitored with intracellular GFP that was expressed in the cytoplasm and exported to the periplasm (henceforth, referred to as 'periplasmic GFP'). Disruption of the cytoplasmic membrane was studied with SYTOX Green, a 300-500 Da small molecule that fluoresces brightly upon binding to DNA. Fluorescence due to GFP would disappear when the outer membrane (OM) is permeabilized. SYTOX signal would be observed when both the OM and the cytoplasmic membrane (CM) are permeabilized. Thus, GFP and SYTOX serve as reporters of membrane permeabilization in this assay. Intervening white light images allowed cell length measurements on the same timescale as fluorescence measurements. LL-37 first permeabilized the OM to GFP, and then permeabilized the CM to SYTOX within 10-40 min. Halting of cell growth coincided with OM permeabilization. There was a substantial

delay of ~10 min between halting of growth and CM permeabilization, as evidenced by SYTOX fluorescence. This result was different from previous understanding that suggested CM disruption to be the lethal step in AMP-mediated growth inhibition of bacteria.

The action of LL-37 was also studied on the Gram positive bacterium *Bacillus subtilis*[47] using single-cell time-lapse imaging. LL-37 exerts a concentration dependent effect on the growth rate and membrane integrity of single *B. subtilis* cells. The bulk MIC of LL-37 for *B. subtilis* is 1 μM, similar to the MIC on *E. coli*[46]. At this concentration, LL-37 had no visible effect on growth rate of single cells observed under the microscope for 1 hour. At 2 μM LL-37, cell growth slowed down over time without membrane permeabilization to SYTOX. The growth inhibitory effect was observed within 10 min, and became more apparent as growth rate plateaued after 20-30 min. At even higher concentration (4 μM), LL-37 caused rapid halting of growth and cell shrinkage within 5 min, and permeabilized the membrane to SYTOX on similar timescales. In a unique 'recovery' assay, LL-37 was rinsed out of the flow chamber with fresh growth medium lacking the AMP, after observation of cell shrinkage and/or membrane permeabilization. For the next 60-90 min, fresh growth medium lacking AMP was flowed through the chamber and the same set of cells was imaged to check if the cells recovered from the AMP treatment. This can be considered as a single-cell analog of the bulk Minimum Bactericidal Concentration (MBC) assay. Cells initially treated with 2 μM LL-37 resumed normal growth upon removal of the AMP. However, at 4 μM LL-37, cells that were already permeabilized did not show clear signs of recovery and never regained their pre-shrinkage length.

Antimicrobial effects of the oxidized form of Human Defensin 5 (HDF_{ox}), containing all three disulfide bonds, have been studied on *E. coli*[48]. A combination of time-lapse fluorescence

microscopy and static Transmission Electron Microscopy (TEM) was employed to show that HDF_{ox} targets the cell division sites in *E. coli* and forms ~1 µm wide blebs at the division septum. Blebbing was considered to be a specific effect of this peptide, and was not observed for other AMPs such as Cryptidin-4, LL-37, Mellitin and Colistin. Studies with fluorescently labeled HDF_{ox} demonstrated that the peptide localizes at cell poles and the division septum. Time-lapse microscopy on *E. coli* expressing cytoplasmic GFP showed significant cell-to-cell variation in the timepoint of appearance of blebs. Blebbing coincided with decrease in GFP fluorescence from the cell body, indicating transfer of GFP molecules to the bleb.

The hybrid AMP CM-15, whose primary sequence is composed of segments from Cecropin and Melittin, was demonstrated to permeabilize the cytoplasmic membrane of *E. coli* within 2-5 min[49]. On similar timescales, CM-15 also caused oxidative stress within as measured by the fluorescence signal of CellROX, an ROS-sensitive dye. In anaerobic conditions, the bulk MIC, growth inhibitory effects and production of reactive oxygen species caused by CM-15 are diminished, indicating that active respiration may be a pre-requisite for the antimicrobial action.

CONCLUDING REMARKS

With the growing threat of antibiotic infections and slowing down of the antibiotic discovery pipeline, the research community is now looking for alternative platforms to develop the next family of antibiotics. AMPs are attractive candidates in this regard due to their rapid microbicidal activity, low hemolytic tendency, and affinity for multiple intracellular targets. To this date, several AMPs have entered clinical trials with limited success[50,51]. No AMP has yet been approved by the FDA for clinical use. Admittedly, there are considerable challenges posed to the research community in developing AMPs for clinically relevant applications. These include susceptibility to proteolytic degradation, loss of activity at physiological salt concentrations and serum conditions, and high production costs.

In parallel with efforts to improve on these parameters, it is crucial to develop powerful methods that will provide mechanistic cues into the action of AMPs on bacteria. The single-cell time-lapse microscopy assays used in this thesis provided detailed information on the early events in the interaction of AMPs with live bacteria. The experimental workflow can be adapted to most commercial and home-built microscopes, and involves relative simple instrumentation. Such single cell studies could be applied to several AMP-bacteria-phenotype combinations. Eventually, this approach will significantly contribute to developing a detailed understanding of the diverse effects of AMPs on bacterial infections.

PART III – MICROSCOPE SETUP

All the microscopy experiments for this thesis were performed on an inverted epifluorescence microscope equipped with a 100X 1.3 NA phase contrast objective. Post-microscope images were further magnified 1.45X in a home-built magnification box. Depending on the choice of fluorophore, laser illumination was carried out at 488 nm or 561 nm. A schematic of the excitation (blue) and emission (green) beam paths is provided in Figure 1.3. A dichroic mirror reflects a collimated blue excitation beam to the objective, which then focuses the beam on to the sample. In 'epi' mode, emitted light at longer wavelengths (green) is collected by the same objective and passed through an emission filter, which passes a select wavelength range. A final tube lens focusses the emitted light onto the detector in an EMCCD camera (Electron Multiplying Charge Coupled Device). White light from a separate source is focused by a condenser lens on to the sample from above.

The sample consists of single *E. coli* cells bound to a poly-L-lysine coated glass coverslip, and housed in a temperature-controlled flow chamber. A typical 50 µm X 50 µm field of view contains up to 50 single cells. In time-lapse mode, the cells are alternately excited with laser and white light using shutters controlled by a TTL pulse generator. In a typical experiment, alternate laser and white light snapshots are acquired once every 3 seconds, resulting in an overall cycle time of 6 s. This translates to 600 imaging cycles for a 30 min experiment. Faster imaging was performed at an acquisition rate of 2-10 snapshots per second. Cell images were acquired using custom software and stored for post-processing.

REFERENCES

(1) Silhavy, T. J., Kahne, D., and Walker, S. (2010) The bacterial cell envelope. *Cold Spring Harb. Perspect. Biol. 2*.

(2) Gan, L., Chen, S., and Jensen, G. J. (2008) Molecular organization of Gram-negative peptidoglycan. *Proc. Natl. Acad. Sci.* pnas.0808035105.

(3) Vollmer, W., and Seligman, S. J. (2010) Architecture of peptidoglycan: more data and more models. *Trends Microbiol. 18*, 59–66.

(4) Oliver, P. M., Crooks, J. A., Leidl, M., Yoon, E. J., Saghatelian, A., and Weibel, D. B. (2014) Localization of anionic phospholipids in *Escherichia coli* cells. *J. Bacteriol. 196*, 3386–3398.

(5) Antimicrobial resistance threats in the United States, 2013. Centers for Disease Control and Prevention.

(6) McKenna, M. (2013) Antibiotic resistance: The last resort. *Nature 499*, 394–396.

(7) Lewis, K. (2013) Platforms for antibiotic discovery. *Nat. Rev. Drug Discov. 12*, 371–387.

(8) Skarnes, R. C., and Watson, D. W. (1957) Antimicrobial factors of normal tissues and fluids. *Bacteriol. Rev. 21*, 273–294.

(9) Fleming, A. (1922) On a remarkable bacteriolytic element found in tissues and secretions. *Proc. R. Soc. Lond. B Biol. Sci. 93*, 306–317.

(10) Hirsch, J. G. (1956) Phagocytin: A bactericidal substance from polymorphonuclear leucocytes. *J. Exp. Med. 103*, 589–611.

(11) Stec, B. (2006) Plant thionins – the structural perspective. *Cell. Mol. Life Sci. 63*, 1370–1385.

(12) Groves, M. L., Peterson, R. F., and Kiddy, C. A. (1965) Polymorphism in the red protein isolated from milk of individual cows. *Nature 207*, 1007–1008.

(13) Stephens, J. M., and Marshall, J. H. (1962) Some properties of an immune factor isolated from the blood of actively immunized wax moth larvae. *Can. J. Microbiol. 8*, 719–725.

(14) Steiner, H., Hultmark, D., Engström, å., Bennich, H., and Boman, H. G. (1981) Sequence and specificity of two antibacterial proteins involved in insect immunity. *Nature 292*, 246–248.

(15) Zasloff, M. (2002) Antimicrobial peptides of multicellular organisms. *Nature 415*, 389–395.

(16) Ganz, T., Selsted, M. E., and Lehrer, R. I. (1990) Defensins. *Eur. J. Haematol. 44*, 1–8.

(17) Wang, Z. (2004) APD: The antimicrobial peptide database. *Nucleic Acids Res. 32*, 590D–592.

(18) Wang, G., Li, X., and Wang, Z. (2009) APD2: The updated antimicrobial peptide database and its application in peptide design. *Nucleic Acids Res. 37*, D933–D937.

(19) Brogden, K. A. (2005) Antimicrobial peptides: pore formers or metabolic inhibitors in bacteria? *Nat. Rev. Microbiol. 3*, 238–250.

(20) Yeung, A. T. Y., Gellatly, S. L., and Hancock, R. E. W. (2011) Multifunctional cationic host defence peptides and their clinical applications. *Cell. Mol. Life Sci. 68*, 2161–2176.

(21) Hilchie, A. L., Wuerth, K., and Hancock, R. E. W. (2013) Immune modulation by multifaceted cationic host defense (antimicrobial) peptides. *Nat. Chem. Biol. 9*, 761–768.

(22) Ganz, T., Metcalf, J. A., Gallin, J. I., Boxer, L. A., and Lehrer, R. I. (1988) Microbicidal/cytotoxic proteins of neutrophils are deficient in two disorders: Chediak-Higashi syndrome and "specific" granule deficiency. *J. Clin. Invest. 82*, 552–556.

(23) Wilson, C. L. (1999) Regulation of intestinal-Defensin activation by the metalloproteinase Matrilysin in innate host Ddfense. *Science 286*, 113–117.

(24) Rosenberger, C. M., and Finlay, B. B. (2003) Phagocyte sabotage: disruption of macrophage signalling by bacterial pathogens. *Nat. Rev. Mol. Cell Biol. 4*, 385–396.

(25) Yang, L., Harroun, T. A., Weiss, T. M., Ding, L., and Huang, H. W. (2001) Barrel-stave model or toroidal model? A case study on Melittin pores. *Biophys. J. 81*, 1475–1485.

(26) Lee, M.-T., Chen, F.-Y., and Huang, H. W. (2004) Energetics of pore formation induced by membrane active peptides †. *Biochemistry (Mosc.) 43*, 3590–3599.

(27) Bürck, J., Roth, S., Wadhwani, P., Afonin, S., Kanithasen, N., Strandberg, E., and Ulrich, A. S. (2008) Conformation and membrane orientation of amphiphilic helical peptides by oriented circular dichroism. *Biophys. J. 95*, 3872–3881.

(28) Ludtke, S. J., He, K., Heller, W. T., Harroun, T. A., Yang, L., and Huang, H. W. (1996) Membrane pores induced by magainin. *Biochemistry (Mosc.) 35*, 13723–13728.

(29) Yang, L., Harroun, T. A., Heller, W. T., Weiss, T. M., and Huang, H. W. (1998) Neutron off-plane scattering of aligned membranes. I. Method Of measurement. *Biophys. J. 75*, 641–645.

(30) He, K., Ludtke, S. J., Worcester, D. L., and Huang, H. W. (1996) Neutron scattering in the plane of membranes: structure of alamethicin pores. *Biophys. J. 70*, 2659–2666.

(31) He, J., Krauson, A. J., and Wimley, W. C. (2014) Toward the de novo design of antimicrobial peptides: Lack of correlation between peptide permeabilization of lipid vesicles and antimicrobial, cytolytic, or cytotoxic activity in living cells. *Biopolymers 102*, 1–6.

(32) Lehrer, R. I., Barton, A., and Ganz, T. (1988) Concurrent assessment of inner and outer membrane permeabilization and bacteriolysis in *E. coli* by multiple-wavelength spectrophotometry. *J. Immunol. Methods 108*, 153–158.

(33) Orlov, D. S., Nguyen, T., and Lehrer, R. I. (2002) Potassium release, a useful tool for studying antimicrobial peptides. *J. Microbiol. Methods 49*, 325–328.

(34) Bolintineanu, D., Hazrati, E., Davis, H. T., Lehrer, R. I., and Kaznessis, Y. N. (2010) Antimicrobial mechanism of pore-forming protegrin peptides: 100 pores to kill *E. coli*. *Peptides 31*, 1–8.

(35) Wu, M., Maier, E., Benz, R., and Hancock, R. E. W. (1999) Mechanism of interaction of different classes of cationic antimicrobial peptides with planar bilayers and with the cytoplasmic membrane of *Escherichia coli* †. *Biochemistry 38*, 7235–7242.

(36) Yount, N. Y., and Yeaman, M. R. (2013) Peptide antimicrobials: cell wall as a bacterial target. *Ann. N. Y. Acad. Sci. 1277*, 127–138.

(37) Patrzykat, A., Friedrich, C. L., Zhang, L., Mendoza, V., and Hancock, R. E. W. (2002) Sublethal concentrations of Pleurocidin-derived antimicrobial peptides inhibit macromolecular aynthesis in *Escherichia coli*. *Antimicrob. Agents Chemother. 46*, 605–614.

(38) Wenzel, M., Chiriac, A. I., Otto, A., Zweytick, D., May, C., Schumacher, C., Gust, R., Albada, H. B., Penkova, M., Kramer, U., Erdmann, R., Metzler-Nolte, N., Straus, S. K., Bremer, E., Becher, D., Brotz-Oesterhelt, H., Sahl, H.-G., and Bandow, J. E. (2014) Small cationic antimicrobial peptides delocalize peripheral membrane proteins. *Proc. Natl. Acad. Sci. 111*, E1409–E1418.

(39) Kandaswamy, K., Liew, T. H., Wang, C. Y., Huston-Warren, E., Meyer-Hoffert, U., Hultenby, K., Schröder, J. M., Caparon, M. G., Normark, S., Henriques-Normark, B., Hultgren, S. J., and Kline, K. A. (2013) Focal targeting by human β-defensin 2 disrupts localized virulence factor assembly sites in *Enterococcus faecalis*. *Proc. Natl. Acad. Sci. 110*, 20230–20235.

(40) Kurushima, J., Nakane, D., Nishizaka, T., and Tomita, H. (2015) Bacteriocin protein BacL $_1$ of *Enterococcus faecalis* targets cell division loci and specifically recognizes l-Ala$_2$-cross-bridged peptidoglycan. *J. Bacteriol.* (Christie, P. J., Ed.) *197*, 286–295.

(41) Scheinpflug, K., Krylova, O., Nikolenko, H., Thurm, C., and Dathe, M. (2015) Evidence for a Novel Mechanism of Antimicrobial Action of a Cyclic R-, W-Rich Hexapeptide. *PLoS ONE 10*, e0125056.

(42) Rathinakumar, R., and Wimley, W. C. (2008) Biomolecular engineering by combinatorial design and high-throughput screening: small, soluble peptides that permeabilize membranes. *J. Am. Chem. Soc. 130*, 9849–9858.

(43) Rathinakumar, R., Walkenhorst, W. F., and Wimley, W. C. (2009) Broad-spectrum antimicrobial peptides by rational combinatorial design and high-throughput screening: the importance of interfacial activity. *J. Am. Chem. Soc. 131*, 7609–7617.

(44) Fantner, G. E., Barbero, R. J., Gray, D. S., and Belcher, A. M. (2010) Kinetics of antimicrobial peptide activity measured on individual bacterial cells using high-speed atomic force microscopy. *Nat. Nanotechnol. 5*, 280–285.

(45) Muñoz, A., and Read, N. D. (2012) Live-cell imaging and analysis shed light on the complexity and dynamics of antimicrobial peptide action. *Front. Immunol. 3*.

(46) Sochacki, K. A., Barns, K. J., Bucki, R., and Weisshaar, J. C. (2011) Real-time attack on single *Escherichia coli* cells by the human antimicrobial peptide LL-37. *Proc. Natl. Acad. Sci. 108*, E77–E81.

(47) Barns, K. J., and Weisshaar, J. C. (2013) Real-time attack of LL-37 on single *Bacillus subtilis* cells. *Biochim. Biophys. Acta BBA - Biomembr. 1828*, 1511–1520.

(48) Chileveru, H. R., Lim, S. A., Chairatana, P., Wommack, A. J., Chiang, I.-L., and Nolan, E. M. (2015) Visualizing attack of *Escherichia coli* by the antimicrobial peptide Human Defensin 5. *Biochemistry (Mosc.) 54*, 1767–1777.

(49) Choi, H., Yang, Z., and Weisshaar, J. C. (2015) Single-cell, real-time detection of oxidative stress induced in *Escherichia coli* by the antimicrobial peptide CM15. *Proc. Natl. Acad. Sci. 112*, E303–E310.

(50) Fox, J. L. (2013) Antimicrobial peptides stage a comeback. *Nat. Biotechnol. 31*, 379–382.

(51) Jenssen, H., Hamill, P., and Hancock, R. E. W. (2006) Peptide antimicrobial agents. *Clin. Microbiol. Rev. 19*, 491–511.

(52) Schittek, B., Hipfel, R., Sauer, B., Bauer, J., Kalbacher, H., Stevanovic, S., Schirle, M., Schroeder, K., Blin, N., Meier, F., Rassner, G., and Garbe, C. (2001) Dermcidin: a novel human antibiotic peptide secreted by sweat glands. *Nat. Immunol. 2*, 1133–1137.

(53) Radermacher, S. W., Schoop, V. M., and Schluesener, H. J. (1993) Bactenecin, a leukocytic antimicrobial peptide, is cytotoxic to neuronal and glial cells. *J. Neurosci. Res. 36*, 657–662.

(54) Selsted, M. E., Novotny, M. J., Morris, W. L., Tang, Y. Q., Smith, W., and Cullor, J. S. (1992) Indolicidin, a novel bactericidal tridecapeptide amide from neutrophils. *J. Biol. Chem. 267*, 4292–4295.

(55) Lehrer, R. I. (2004) Primate defensins. *Nat. Rev. Microbiol. 2*, 727–738.

(56) Kokryakov, V. N., Harwig, S. S. L., Panyutich, E. A., Shevchenko, A. A., Aleshina, G. M., Shamova, O. V., Korneva, H. A., and Lehrer, R. I. (1993) Protegrins: leukocyte antimicrobial peptides that combine features of corticostatic defensins and tachyplesins. *FEBS Lett. 327*, 231–236.

(57) Leptihn, S., Har, J., Chen, J., Ho, B., Wohland, T., and Ding, J. (2009) Single molecule resolution of the antimicrobial action of quantum dot-labeled Sushi peptide on live bacteria. *BMC Biol. 7*, 22.

(58) Rangarajan, N., Bakshi, S., and Weisshaar, J. C. (2013) Localized permeabilization of *E. coli* membranes by the antimicrobial peptide Cecropin A. *Biochemistry (Mosc.) 52*, 6584–6594.

(59) Bakshi, S., Choi, H., Rangarajan, N., Barns, K. J., Bratton, B. P., and Weisshaar, J. C. (2014) Nonperturbative imaging of nucleoid morphology in live bacterial cells during an antimicrobial peptide attack. *Appl. Environ. Microbiol. 80*, 4977–4986.

(60) Raetz, C. R., Whitfield, C. (2002) Lipopolysaccharide endotoxins. *Annu. Rev. Biochem. 71*, 635-700.

List 1.1

Factors taken into account for determining threat levels of resistant infections:

(1) Clinical impact

(2) Economic impact

(3) Incidence

(4) Transmissibility

(5) Barriers to prevention

(6) Ten year projection of incidence

(7) Availability of effective antibiotics

Table 1.1: Classification of threat levels of various bacterial pathogens (CDC Threat Report 2013)

Hazard level	**Urgent**	**Serious**	**Concerning**
Details	• Significant risks identified • Could become widespread • Need urgent public health attention	• Significant resistance threats • Low/declining domestic incidence • May become urgent	• Low threat • Multiple therapies available • Rapid incident/outbreaks possible
Examples	*Clostridium difficile*	Multi drug-resistant *Pseudomonas aeruginosa*	Vancomycin-resistant *Staphylococcus aureus*
	Carbapenem-resistant *Enterobactereriaceae*	Multidrug-resistant *Acinetobacter baumannii*	Erythromycin-resistant *Streptococcus* Group A
	Cephalosporin resistant *Neisseria gonnorhea*	Multi drug-resistant Tuberculosis	Clindamycin-resistant *Streptococcus* Group B

Table 1.2: Classification of AMPs based on composition and structure

AMP characteristics	Examples	Reference(s)
Anionic Require Zn^{2+} as a co-factor	Dermicidin (humans)	52
Linear, cationic Form α-helices	Cecropin A, Melittin (insects) LL-37 (humans)	14,52
Cationic Enriched for Arg/Pro/Trp	Bactenecin, Indolicidin (cattle)	53,54
Closed loop Form disulfide bonds, β-sheets	Defensins (humans, primates, insects, plants) Protegrin (pigs)	55,56

Table 1.3: Timeline of single-cell AMP studies on bacteria

Year	Bacterium	Microscopy Technique	Peptide studied	Labeling strategy	Reference
2009	*E. coli*	TIRF, single particle tracking	Sushi 1	Sushi 1-Qdot655 (Quantum dot)	57
2011	*E. coli*	Widefield	LL-37	Rhodamine-LL37, SYTOX Green, Periplasmic GFP	46
2013	*B. subtilis*	Widefield	LL-37	SYTOX Green, Periplasmic GFP	47
2013	*E. coli*	Widefield	Cecropin A	SYTOX Green, Periplasmic GFP	58
2014	*E. coli*	Widefield	Cecropin A, LL-37	SYTOX Orange, Ribosome-YFP	59
2015	*E. coli*	Widefield	CM-15	CellROX, Amplex Red	49

Figure 1.1

A schematic of the *E. coli* cell envelope (reproduced from Reference 60)

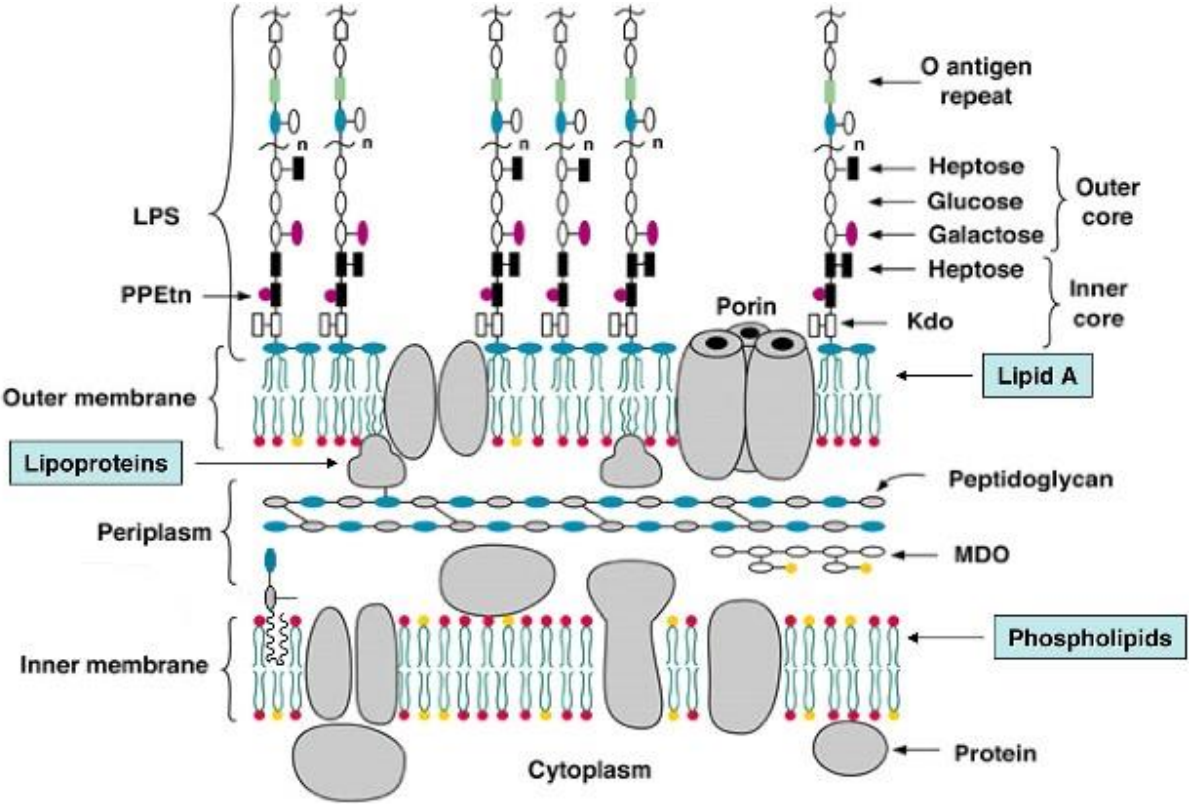

Figure 1.2

Ribbon diagrams illustrating the secondary structures adopted by various antimicrobial peptides.

LL-37 **CM-15** **Indolicidin** **Human β-Defensin 1**

Figure 1.3

A schematic of the epifluorescence microscope setup used for image acquisition in this thesis.

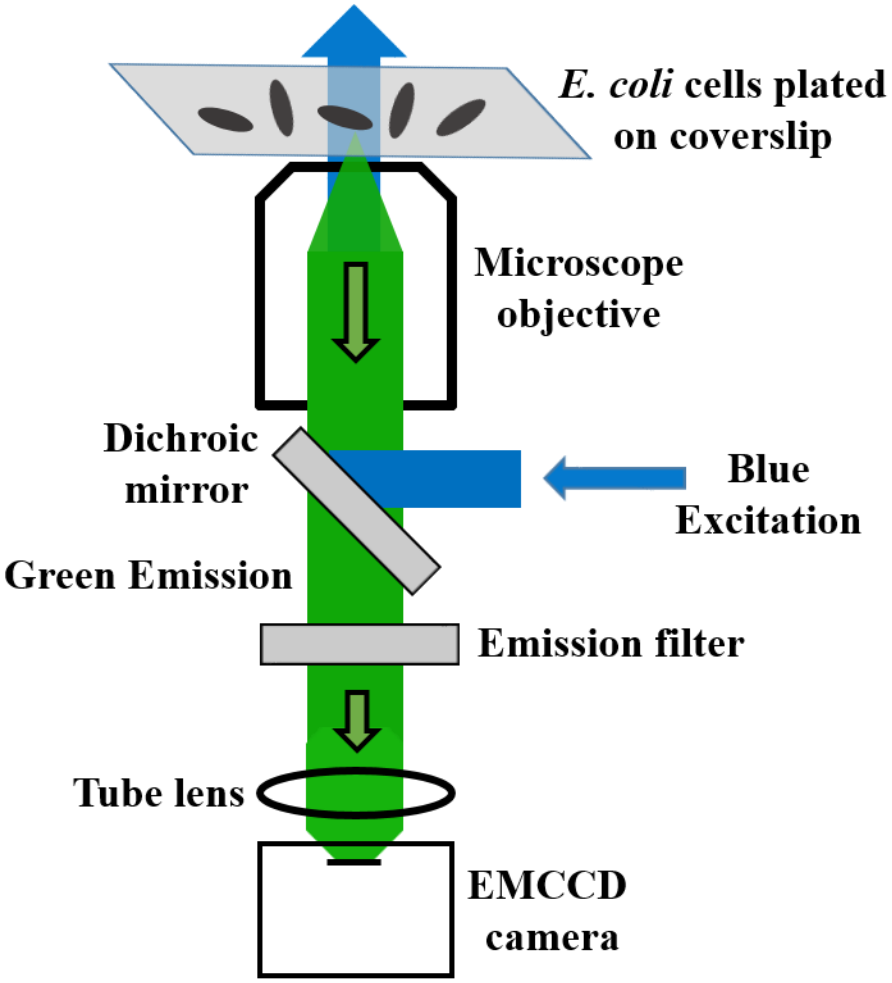

(Not drawn to scale)

CHAPTER TWO

Localized Permeabilization of *E. coli* Membranes by the Antimicrobial Peptide Cecropin A

Reproduced verbatim from:

Rangarajan, N., Bakshi, S., and Weisshaar, J. C. (2013) Localized Permeabilization of *E. coli* Membranes by the Antimicrobial Peptide Cecropin A. *Biochemistry (Mosc.) 52*, 6584–6594.

ABBREVIATIONS

AMP, antimicrobial peptide, OM: outer membrane; CM, cytoplasmic membrane; GUV, giant unilamellar vesicle; LUV, large unilamellar vesicle; MIC, minimum inhibitory concentration; GFP, green fluorescent protein; ROI, region of interest.

ABSTRACT

Fluorescence microscopy enables detailed observation of the effects of the antimicrobial peptide Cecropin A on the outer membrane (OM) and cytoplasmic membrane (CM) of single *E. coli* cells with sub-second time resolution. Fluorescence from periplasmic GFP decays and cell growth halts when the OM is permeabilized. Fluorescence from the DNA stain Sytox Green rises when the CM is permeabilized and the stain enters the cytoplasm. The initial membrane disruptions are localized and stable. Septating cells are attacked earlier than non-septating cells, and curved membrane surfaces are attacked in preference to cylindrical surfaces. Below a threshold bulk Cecropin A concentration, permeabilization is not observed over 30 minutes. Above this threshold, we observe a lag time of several minutes between Cecropin A addition and OM permeabilization and ~30 s between OM and CM permeabilization. The long lag times and the existence of a threshold concentration for permeabilization suggest a nucleation mechanism. However, the roughly linear dependence of mean lag time on bulk peptide concentration is not easily reconciled with a nucleation step involving simultaneous insertion of multiple peptides into the bilayer. Monte Carlo simulations suggest that within seconds the OM permeability becomes comparable to that of a pore of 100-nm diameter, or of numerous small pores distributed over a similarly large area.

Introduction

Antimicrobial peptides (AMPs) are ubiquitous host defense agents essential to the immune system of a variety of organisms, from microbes to insects, plants, and animals.[1] These peptides may prove effective in combating multi-drug resistant pathogens. Literally thousands of AMPs have been discovered in nature, and dozens of synthetic variants have been developed and tested for antibacterial efficacy. They vary in sequence length (up to 50 residues), net charge (often highly cationic), secondary structure (α-helix, β-hairpin), and the fraction, sequence, and composition of hydrophobic and hydrophilic residues.[2, 3] The selectivity of attack on bacterial cells vs eukaryotic cells presumably arises from electrostatic attraction of the cationic peptides to the anionic outer layer of both Gram negative and Gram positive bacteria. While it is known that AMPs at sufficiently high concentration disrupt bacterial membranes, the detailed mechanism by which they halt growth and kill bacterial cells is not certain, and may well vary from case to case. A clear relationship between peptide sequence and function has not yet emerged. A balance between hydrophobic and hydrophilic resides is important, but amphipathicity is evidently not essential.[2, 4] Experiments that mix bulk bacterial cultures with AMPs have revealed information about the timing of antibacterial action as well as biochemical mechanisms.[3] Suggested mechanisms of AMP activity against bacterial cells include interference with cell wall biosynthesis, loss of key periplasmic or cytoplasmic components after permeabilization of membranes, and triggering of signaling pathways that alter the bacterial metabolic state.[2]

There is a long history of biophysical studies of the interaction of AMPs with model lipid bilayers, including large unilamellar vesicles (LUVs) and giant unilamellar vesicles (GUVs).[2] Kinetics studies have monitored release of LUV content[2,5,6] and the thinning and bursting of GUVs vs time after addition of the AMP.[7-11] In some cases there is evidence of transient membrane disruption (“graded” content release), while in other cases permeability persists until

all content is released ("all or none" release).[12] Structural studies have used x-ray and neutron diffraction,[13] oriented circular dichroism,[14] and NMR[15] to study AMPs bound to multilayers, LUVs, or micelles. Many AMPs fold into amphipathic helices on binding to lipid bilayers.[16] At low surface coverage, helical AMPs bind with the long axis parallel to the membrane surface; the resulting tension leads to membrane thinning.[9] At higher surface coverage, helices insert into the bilayer with the axis perpendicular to the membrane surface.

The nature of the membrane disruptions induced by antimicrobial peptides has been controversial.[2] One standard concept is the formation of discrete pores, either "barrel-stave" or "toroidal". In lipid multilayers, x-ray diffraction provides direct evidence of pore-like structures at high peptide surface density.[13, 14] However, recent molecular dynamics simulations argue against a well-defined geometry comprising a fixed number of AMPs.[17, 18] Membrane disruptions are likely to be much more disordered and fluxional than depicted by typical cartoons of toroidal pores.[19] A seemingly different concept is the "carpet" model and its variants, all of which involve detergent-like solubilization or micellization of lipids by the AMP.[20, 21] Carpets could be localized or global. Recent structural studies found a correlation between the activity of antimicrobial oligomers and their ability to form a three-dimensional, inverted hexagonal phase in mixtures with lipids.[22, 23] This highly curved phase is perhaps reminiscent of the micelle-like structures proposed in the carpet mechanism. In our view, the distinctions among pores, chaotic pores, localized carpets, and localized "hexagonal phase precursor states" are blurry.

Cecropin A is a well-studied AMP isolated from the moth *Hyalophora cecropia*.[24] Its 37-amino acid sequence contains seven Lys, one Arg, one Glu, and one Asp for a net charge of +7 at neutral pH. (The N-terminus contributes +1, while the C-terminus is amidated.) On binding to lipid bilayers, it adopts a helix-break-helix motif, with amphipathic helical segments formed by residues 5-21 and 24-37. At low surface concentrations, both helical segments lie

parallel to the lipid bilayer. [25, 26] Cecropin A induces content release from lipid vesicles.[27] Both *L*- and *D*- optical isomers of Cecropin A show comparable ability to kill bacterial cells.[28] Evidently the killing mechanism is related to interactions with bacterial membranes, not to binding to specific enzymatic targets.

The detailed nature of the membrane disruptions induced by Cecropin A is unclear. Early studies showed that Cecropin A releases encapsulated dye from liposomes and inhibits *E. coli* growth within 10 min of incubation.[29] Cecropin A forms pore-like ion-channels on planar lipid bilayers.[30] In liposomes, Cecropin A disrupts ion gradients at low concentrations, while much higher concentrations are required to release encapsulated probes.[31] On the other hand, in bacterial cells Cecropin A exerts its bactericidal effect, disrupts membrane potential and permeabilizes membranes at the same concentration.[32] Both "pore-like" and "carpet-like" models have been proposed to explain different experimental results.[21, 27] The strength of the connection between studies of model membranes and the mechanisms by which AMPs disrupt real bacterial cell membranes remains to be seen.

Fluorescence microscopy of AMP interactions with single, live bacterial cells provides a completely new level of real-time mechanistic detail that is not discernible from bulk measurements.[33, 34] Here we present a study of the interaction of Cecropin A with single *E. coli* cells in real time with sub-second resolution. Fast movies at 2 frames/s show that the initial OM permeabilization event occurs preferentially in specific membrane regions that depend on whether or not the cell is septating. The event is local and persistent. We directly observe a lag time of several minutes between injection of Cecropin A and disruption of the outer membrane (OM) and a second lag time of ~30 s between entry of Cecropin A into the periplasm and disruption of the cytoplasmic membrane (CM). Comparisons with Monte Carlo simulations

indicate that the initial degree of permeabilization is large and expands over several seconds. While superficially similar in length, charge, and structure, LL-37 and Cecropin A show different propensities for which membrane locations are attacked and for the degree of permeability induced.

Experimental Procedures

Materials. Cecropin A (Anaspec, catalog no. 24010, > 95% purity) and LL-37 (Anaspec, catalog no. 61302, 95% purity) were purchased as lyophilized powders and used without further purification. All peptide stock solutions were made in sterile, ultrapure (18 MΩ) water. A 5 mM solution (in DMSO) of Sytox Green was purchased from Molecular Probes (S7020). Cell cultures were grown in EZ Rich Defined Medium (EZRDM),[35] which consists of MOPS buffer (M2130, Teknova), nucleic acids (M2103, Teknova), amino acids (M2104, Teknova), glucose (2 mg/mL), K_2HPO_4 (1.32 mM) and NaCl (76 mM).

Bacterial strains and cell cultures. The *E. coli* strain is K12 (MG1655). For experiments monitoring periplasmic GFP, TorA-GFP was expressed from the plasmid pJW1 as previously described.[36] TorA-GFP consists of a short sequence (43 residues) from trimethylamine N-oxide (TMAO) reductase that signals the twin-arginine translocase (TAT) pathway.[37] The TorA signal sequence is cleaved from GFP in the periplasm. The 12-hr MIC of Cecropin A is 0.5 μM.

Cell cultures were grown overnight at 30ºC to stationary phase. Sub-cultures were grown to exponential phase (optical density ~ 0.5 at 600 nm) and injected into the flow chamber for imaging. We select a region that has at least 10 cells lying flat within the 50 μm diameter observation region prior to initiation of image acquisition and injection of Cecropin A.

Flow chamber. The flow chamber has been described earlier.[30] It consists of two silicone gaskets (Warner Instruments, catalog no. 64-0335, thickness 375 μm per gasket) sandwiched between two poly-L-Lysine-coated glass coverslips (Fisher Scientific). The chamber volume is ~72 μL. The base plate is maintained at 30ºC by a TC-344B dual channel temperature controller and CC-28 heating cables attached to RH-2 heater blocks (all from Warner

Instruments). Solutions are injected into the flow chamber by hand using 1 mL NORM-JECT injection syringes. Typically, ~400 μL of peptide solution is injected over the course of ~5 s. By imaging solutions of fluorescent dyes, we have shown that this volume and flow rate fill the chamber uniformly. After injection of the peptide solution, the observation volume remains static throughout the course of the experiment.

Fluorescence imaging. The flow chamber, microscopy protocol, and the minimum inhibitory concentration (MIC) assay employed in this work have been described earlier.[33] We image Cecropin A-induced permeabilization of the outer membrane to GFP and permeabilization of the cytoplasmic membrane to the DNA the stain Sytox Green as follows. The *E. coli* cells export GFP to the periplasm.[36] At $t = 0$, growth medium containing Cecropin A and also 5 nM Sytox Green is injected into the flow chamber over a period of ~5 s. Sytox Green in buffer is non-fluorescent, but it fluoresces green on binding to chromosomal DNA. On excitation at 488 nm, each single cell exhibits a thin shell of GFP fluorescence. When the outer membrane becomes permeabilized to GFP, the thin shell of fluorescence gradually disappears. In the absence of Cecropin A, we detect no Sytox Green staining of DNA under our conditions. When both the outer membrane and cytoplasmic membrane become permeabilized to Sytox Green, we observe the onset of fluorescence from Sytox Green in a nucleoid staining pattern. To observe localized loss of periplasmic GFP and nucleoid staining by Sytox Green, images were acquired at a frame rate of 2 frames/s with an exposure time of 50 ms/frame.

Cells were typically imaged for 10 min at 2 μM Cecropin A (four times the MIC) and 20 min at 1 μM (twice the MIC). The cost of the peptide precludes studies under flow conditions that would stabilize the bulk concentration. The stated Cecropin A concentrations are only

nominal. The actual bulk concentration is likely smaller than that of the injected solution due to unquantified losses at the walls of the flow chamber.

To monitor cell length vs time (a proxy for growth) in the presence of Cecropin A, the cells were alternately excited by 488 nm and white light at a rate of 1 frame every 3 seconds with an exposure time of 50 ms/frame. The interleaved fluorescence and white light images were separated during image processing. An elliptical mask was made in MATLAB that matched the cell boundaries. The major axis length of this mask was measured to estimate the cell length vs time for correlation with events in the same cell signaled by changes in fluorescence intensity vs time.

Data Analysis. Images were acquired using Andor Solis (version 4.8.30002.0) and data analyses were performed in ImageJ (version 1.47a), Microcal Origin (version 9.0) and MATLAB (version 7.11.0). To measure the total fluorescence intensity in a single cell, a region of interest (ROI) enclosing the cell was drawn in ImageJ. Background signal was measured by duplicating the same ROI on a region of the image that did not contain a cell. The fluorescence intensity of the ROI corresponding to the cell was measured and background was subtracted. This process was repeated for each frame of the entire 10-20 min movie. All cells that remain in focus long enough for antimicrobial effects to be observed are included in the analysis. Plots of axial intensity projections are obtained as described in Supporting Information.

Results

Attack on Septating Cells. Late in the cell cycle, as *E. coli* prepares to divide into two daughter cells, the previously straight cylindrical flank of the cell begins to septate at the cell midplane. The parent cell will eventually pinch off two daughter cells, and the septal region will become two new hemispherical endcaps. The early stages of septation are directly observable in phase contrast images and in periplasmic GFP images as a slight depression in the previously straight cell body. In this study, we classify cells as "septating" or "non-septating" based on visual inspection of the phase contrast and periplasmic GFP images; compare Figs. 1 and 2. All cells labeled as septating are surely in the process of septation, but some cells in the very early stages of septation will be categorized as non-septating.

Cecropin A at nominal concentration of 2 μM, four times the MIC, attacks the membranes of septating cells earlier than non-septating cells, as described in detail below. The sequence of events in the antimicrobial action of Cecropin A at 2 μM on a septating cell is illustrated in Fig. 1. For this particular cell, there is a lag time of ~1 min after injection of Cecropin A during which no effects on GFP are observed. Cecropin A has permeabilized the OM at the nascent septum at t = 1.08 min after addition of the AMP, as shown by the dark septal region due to loss of periplasmic GFP fluorescence. Evidently the loss of periplasmic GFP to the surround is sufficiently rapid that diffusion cannot keep up.

The expanded time scale with images spaced by 0.5 s (Fig. 1) shows clearly that the initial loss of GFP causes a *localized* dark patch on one side of the septal region, clear evidence of radially asymmetric loss of GFP. Over 3–5 s, the dark patch spreads around the circumference of the septum, as shown by the images gradually becoming axially symmetric. Over 10-15 s, the dark region spreads axially outward towards the endcaps. The outward flux of GFP is evidently

diffusion-limited. About 15 s after the onset of GFP loss (t = 1.25 min), the thin shell of GFP fluorescence has been lost entirely. All septating cells exhibit a central dark patch, but only a few septating cells exhibit the radially asymmetric dark patch. Some localized dark patches may occur near the top or bottom of the cell rather than on the side, and thus appear less asymmetric.

For the same cell, after an additional lag time of ~30 s Cecropin A permeabilizes the CM to Sytox Green, as evidenced by an increase in green fluorescence (t = 1.7 min). The expanded time scale shows that nucleoid staining by Sytox Green begins near one endcap as a bright dot, indicating *localized* entry into the cytoplasm. Evidently binding to DNA is sufficiently strong that the earliest Sytox Green molecules diffuse only a short distance within the nucleoid region before binding. Subsequent entry and binding of more Sytox Green causes the bright initial dot to spread. In this particular cell, the staining pattern suggests that a second localized disruption of the CM occurs in the other half of the cell beginning at t = 1.85 min. In many cases, only one bright dot is observed.

Attack on Non-septating Cells. When Cecropin A at nominal concentration of 2 μM attacks non-septating cells, permeabilization of the OM and loss of periplasmic GFP almost always begin near one endcap. The lag time is 2–8 min, much longer than for septating cells. As illustrated in Fig. 2, periplasmic GFP is lost from one end of the cell. For this particular cell, OM permeabilization occurs almost 4 min after injection of Cecropin A. The dark patch spreads across the entire cell periphery in ~15 s, as shown in the expanded view. In five examples, the non-septating cell under study had remained adhered to its sister cell prior to the Cecropin A attack, enabling us to distinguish the new pole from the old pole. The OM permeabilization always occurs at the new pole.

The subsequent permeabilization of the CM to Sytox Green occurs 32 s after the OM is permeabilized to GFP. CM permeabilization is again fairly localized in space, as evidenced by an initial bright dot of fluorescence that gradually spreads across both nucleoid lobes. The location of CM permeabilization varies from cell to cell, as described next.

Distribution of Permeabilization Events along the Cell Axis. In Fig. 3, the axial locations of each pair of OM and CM permeabilization events are plotted using a relative axial coordinate scale. Here $x_{rel} = 0$ is defined as one tip of the cell and $x_{rel} = 1$ is defined as the other tip. The septum lies near $x_{rel} = 0.5$. In septating cells, $x_{rel} = 0$ is chosen arbitrarily at one tip. In non-septating cells, $x_{rel} = 0$ is defined as the tip near which GFP loss begins. Details regarding cell coordinates and determination of the values of x_{rel} at which GFP leaves and Sytox Green enters are given in Supporting Information (Fig. S2).

In visibly septating cells, GFP is always lost from the septal region, while Sytox Green tends to enter the cytoplasm near one endcap. This occurs in spite of the fact that the concentration of Cecropin A within the periplasm must initially be highest near the septum, where entry into the periplasm occurs. For non-septating cells, permeabilization of the OM to GFP occurs preferentially near one endcap ($x_{rel} \sim 0.1$). The subsequent site for permeabilization of the CM to Sytox Green is broadly distributed along the cell axis, but tends to occur on the half of the cell distal to the OM permeabilization site. There is a preference for the opposite endcap.

Timing of Membrane Permeabilization Events and Cell Shrinkage Events vs Cecropin A concentration. We have also measured the distribution of timings of specific membrane permeabilization events across cells and correlated these events with the halting of cell growth. An example of total green fluorescence intensity vs time for a single, non-septating cell, obtained at an acquisition rate of 1 frame every 6 s and corrected for background intensity,

is shown in Fig. 4 (green trace). We define $t = 0$ as the time of injection of Cecropin A at nominal 2 μM concentration. As evidenced by the transverse intensity linescan (Figure S1), the green fluorescence intensity prior to addition of Cecropin A is due primarily to periplasmic GFP, with small contributions from cytoplasmic autofluorescence and from GFP that has not been exported to the periplasm. At t_{OM} = 4.8 min, the outer membrane is permeabilized to GFP and the cell length shrinks abruptly. The cell loses all fluorescence intensity over the next 18 s. At t_{CM} = 5.2 min, the CM is permeabilized to Sytox Green and the fluorescence abruptly rises, this time in a nucleoid-staining pattern. The Sytox Green signal plateaus when all binding sites are saturated and then slowly decreases due to photobleaching. Analogous measurements were carried out for Cecropin A at nominal concentrations of 1 μM and 4 μM (twice and eight times the MIC). Data from multiple experiments (four experiments at 1 μM, seven at 2 μM, and one at 4 μM, with each experiment involving 5-15 unique cells) was pooled to obtain cell-averaged results.

In Fig. 5A, we compare histograms of t_{OM} for septating vs non-septating cells at 2 μM Cecropin A. The mean value $< t_{OM} >$ is 100 ± 39 s (± one standard deviation) for septating cells, compared with 225 ± 94 s for non-septating cells. Both distributions are broad, with standard deviations about half the mean. This ensemble data clearly indicates that the membranes of septating cells are permeabilized earlier than those of non-septating cells, as in the examples of Figs. 1 and 2.

The bulk Cecropin A concentration significantly affects the distribution of t_{OM}. In Fig. 5B we compare 1 μM and 2 μM in histograms including all cells, both septating and non-septating. At 1 μM, the distribution has a long tail. As the nominal concentration increases from 1 μM to 2 μM to 4 μM, the mean value $< t_{OM} >$ for all cells combined decreases from 540 ± 300 s to 183 ±

99 s to 108 ± 51 s. In Fig. 5C, we show a histogram of the lag time between OM permeabilization and CM permeabilization, ($t_{CM} - t_{OM}$), at 1 μM and 2 μM bulk Cecropin A. The two histograms are similar, except for several outliers at long delay times for the 1 μM data. The breadth of the distribution of t_{OM} is quite similar to that of t_{CM} (Figs. S3, S4, S5), while the breadth of the distribution of ($t_{CM} - t_{OM}$) is much smaller. Most of the variability in t_{CM} is due to variability in t_{OM}.

Table 1 summarizes $< t_{OM} >$, $< t_{CM} >$, and $< t_{CM} - t_{OM} >$ for septating, non-septating, and all cells combined at all three Cecropin A concentrations. Additional histograms partitioning the data into septating and non-septating cells are included as Figs. S3 and S4.

Finally, we measured cell length vs time from the interspersed phase contrast images, enabling us to correlate the apparent halting of cell growth with the membrane permeabilization events. An example for a septating cell at 2 μM Cecropin A is included in Fig. 4 (black trace). Prior to injection of Cecropin A, cell length gradually increases with time. Cell growth halts abruptly at t = 4.7 min, some 6 s before the onset of GFP loss, and the cell gradually shrinks in length by 12% over the next 40 s. This is the general pattern for both septating and non-septating cells at all three concentrations studied. After shrinkage, cell length levels off and does not recover. Significantly, permeabilization of the CM to Sytox Green (and presumably loss of the transmembrane potential) consistently occurs about 30 s *later* than the start of cell shrinkage. We suggest that the abrupt shrinkage is an osmotic effect that occurs at the same time as entry of Cecropin A into the periplasm, but the detailed mechanism is unclear. Similar abrupt shrinkage events were observed for LL-37 on *E. coli* and on *B. subtilis* in earlier work.[33, 34]

There is mild evidence that Cecropin A at 2 μM sometimes decreases the cell growth rate shortly after injection and well before the OM permeabilization event. In Fig. S6, the plot of

length vs time is curving upward prior to injection of Cecropin A but the curvature decreases immediately after injection. This decrease in the *rate* of growth is evident in 4 of 6 cases examined closely. Perhaps a stress signal transmitted through both membranes has slowed growth before Cecropin A permeabilizes the OM.[38] Alternatively, some Cecropin A molecules may translocate across the OM and affect cell wall growth prior to forming GFP-sized disruptions. A similar slowing of growth of *B. subtilis* was observed on injection of sub-lethal concentrations of LL-37.[34]

Time Scale of GFP Release and of Sytox Green Entry. We can infer something of the nature and magnitude of the membrane disruption from the time course of the release of GFP from the periplasm (Δt_{GFP}, Fig. 4) and the entry of Sytox Green into the cytoplasm (Δt_{Sytox}). Because each curve may have a different shape, we define Δt_{GFP} as the time required for the GFP signal to decay from 90% to 10% of its initial value and Δt_{Sytox} as the time required for the Sytox Green signal to rise from 10% to 90% of its final value. Histograms of the distribution of these values are given in Figs. S3, S4, and S5. Means and standard deviations are provided in Table 1 for the three Cecropin A concentrations studied. The values of Δt_{GFP} will constrain Monte Carlo simulations of GFP loss, as described below.

The rate of release of GFP shows distinct behavior for different cells, as shown in Fig. 6 for two septating cells at 2 μM Cecropin A. In most cells, the GFP loss is quite abrupt, while in a few cells the loss is initially gradual. The more gradual release events seem somewhat more likely for septating cells (4 out of 13 examples) than for non-septating cells (2 out of 15). In cells that exhibit the more gradual GFP loss, the dark patch occurs first on one half of the cell, but it is more delocalized and less sharply delineated at early times. The slower the GFP loss, the more effectively diffusion competes with efflux. The Monte Carlo simulations described next provide

quantitative insights into the magnitude of membrane permeability and how it changes in time after the initial disruption event.

Simulations of GFP Loss from the Periplasmic Space. The spatial and temporal course of GFP release from the periplasm is governed by the diffusion coefficient of GFP and the size, location, and permeability of the OM disruption. We have carried out Monte Carlo (random walk) simulations of diffusion to an absorbing patch on the outer membrane in a model geometry chosen to mimic the periplasm: a thin space between two nested spherocylinders (Fig. 7A). The GFP population is modeled as 20,000 point particles, initially randomly distributed in the periplasmic space. The permeable region of the outer membrane is modeled as a perfectly absorbing patch.[39] A particle is removed from the simulation whenever it crosses the absorbing surface patch. No "re-crossings" of the surface patch are permitted, meaning that the model yields the fastest possible leakage of GFP through a hole in the OM. In comparison, both a pore of finite thickness and a carpet patch would transmit GFP less efficiently. Parameters of the simulation include the GFP diffusion coefficient D_{peri}, the periplasm thickness d, and the geometry and location of the absorbing patch. Details are given in Supporting Information.

For septating cells, we experimented with circular absorbing patches of varying diameter placed at the septum and with an absorbing annular ribbon that circumscribes the entire cylinder (Fig. 7A). The diameter of the circular patch (w_{pore}) and the width of the ribbon (w_{ribbon}) were varied along with the value of D_{peri} (Figs. S8 and S9). For non-septating cells, we use a circular patch centered at one cell tip (Fig. 7A). In each simulation, the size and shape of the absorbing patch is held constant in time. To simulate fluorescence images, the particle positions are first blurred by the diffraction limit. Simulated images in space and time can then be projected onto two dimensions (as in Fig. 7C, mimicking the microscopy experiments of Figs. 1 and 2) or integrated over the short cell axis to produce simulated axial intensity profiles (as in Fig. 7C).

They can also be integrated over space to yield the time course of total GFP leakage and Δt_{GFP} (as in Figs. 4 and 7B and in Table 1). For both septating and non-septating cells, our simulations indicate that the permeable region must already be large within ~2 s and must grow even larger over the subsequent 5–10 s.

In Fig. 7C we compare the simulation results with the data from the same septating cell shown in Fig. 1. The simulations match experiment best when D_{peri} is chosen in the narrow range 0.5–1.0 μm^2-s^{-1}. For smaller diffusion coefficients Δt_{GFP} becomes too long, and for larger diffusion coefficients the observed spatial hole never becomes deep enough due to fast equilibration of the GFP distribution. Remarkably, the simulations show that in order to absorb GFP on the experimental time scale of Δt_{GFP} ~ 10-20 s (Fig. 7B), a single circular patch must have a very large diameter, ~100-200 nm. An absorbing ribbon at the septal region also matches the time scale well with D_{peri} = 0.5 μm^2-s^{-1}, independent of the value of w_{ribbon} (Fig. S8). Models tuned to match Δt_{GFP} decay more rapidly than experiment at t = 0 but less rapidly than experiment at later times. The model thus suggests that the OM permeability is increasing in time over the first several seconds, even in cases of nominally abrupt GFP loss curves (Fig. 6).

In addition, neither a static circular patch nor a static annular ribbon mimics the time-dependent spatial distribution well (Fig. 7C). The circular patch mimics the radial asymmetry at early times, but the asymmetry persists too long and the depth of the axial hole remains too shallow. The static ribbon cannot explain the radial asymmetry, but it captures the longer-term depth of the axial hole much better than the circular patch. We have not carried out simulations with time-evolving permeable patches. However, for the septating cell in Fig. 1 it seems likely that the observations could be well matched by a large, localized initial patch that evolved over the first few seconds into an annular ribbon.

For non-septating cells, the experimental results show $<\Delta t_{GFP}>$ ~ 10–20 s. Again with D_{peri} = 0.5-1.0 μm^2-s^{-1} and a circular patch at the tip of the cell of diameter as large as 100-200 nm, the simulation can match the experimental GFP loss times and approximate the time-dependent GFP spatial distribution (Fig. S10). We discuss possible interpretations of such large permeable patches below.

Simulations of Sytox Green entry into the cytoplasm would depend on the permeability of both OM and CM to Sytox Green as well as the effective binding strength of Sytox Green to DNA and its diffusion coefficient within the cytoplasm. Such a large parameter space is not well constrained by the present data. The fact that Δt_{Sytox} is consistently larger than Δt_{GFP} does not necessarily indicate that the disruptions of the cytoplasmic membrane are less permeable than those of the outer membrane. The nucleoid binding capacity is large; it may absorb a very large number of Sytox Green molecules on the way to the maximum of the green fluorescence signal.

Comparison Study of LL-37. The length and charge of LL-37 (LLGDFFRKSKEKIGKEFKRIVQRIKDFLRNLVPRTES-NH_2) and Cecropin A (KWKLFKKIEKVGQNIRDGIIKAGPAVAVVGQATQIAK-NH_2) are similar,[40] so it is of interest to compare their effects on *E. coli* in some detail. Our previous study of LL-37 focused primarily on Rhodamine-labeled LL-37. Using the fast image acquisition scheme introduced here, we have studied membrane permeabilization events for unlabeled LL-37 for comparison with Cecropin A. The 12-hour MIC for LL-37 is 1 μM. The timing results for permeabilization events and for the loss of GFP and the rise of Sytox Green signal are summarized in Table S1. As for Cecropin A, the LL-37-induced disruption of both OM and CM is localized, and there is a substantial lag time before each step. However, there are both qualitative and quantitative differences between LL-37 and Cecropin A. Like Cecropin A, LL-37 attacks septating cells earlier and disrupts the OM at the septal region, leading to complete loss of GFP. However,

LL-37 then also disrupts the CM at the septal region (Fig. S11). In contrast, Cecropin A tends to attack the CM at one endcap. For non-septating cells, LL-37 locally disrupts the OM at one endcap (like Cecropin A) and then locally disrupts the CM *at the same endcap*. In contrast, for Cecropin A the location of the second event seems polarized towards the opposite end of the cell (Fig. 3). These differences in mode of attack are illustrated in Fig. 8 for a typical non-septating case and in Fig. S11 for a typical sepatating example.

Comparisons of timing events between LL-37 and Cecropin A should be made with caution. The most appropriate comparison would be carried out at equal adsorbed surface concentration of the two peptides. However, in this work with unlabeled peptides, we can only compare the action of the two peptides at equivalent bulk concentrations relative to the MIC. Bulk peptide concentrations are only nominal due to unquantifiable losses of AMP at the surfaces of the chamber. Nevertheless, LL-37 at nominal bulk concentration of 4 μM (four times the MIC) takes much longer to disrupt the OM than Cecropin A at nominal bulk concentration of 2 μM (again four times the MIC). For all cells combined, $\langle t_{OM} \rangle$ = 670 ± 540 s for LL-37 vs 180 ± 100 s for Cecropin A. The same holds for the lag time between disruption of the OM to GFP and disruption of the CM to Sytox Green ($\langle t_{CM} - t_{OM} \rangle$ = 320 ± 280 s for LL-37 vs 39 ± 17 s for Cecropin A). Surprisingly, although LL-37 preferentially attacks septating cells first, the time lag $\langle t_{CM} - t_{OM} \rangle$ is fourfold *longer* for septating cells vs non-septating cells.

Alternatively, we can compare LL-37 at 8 μM with Cecropin A at 2 μM, so that the lag times $\langle t_{OM} \rangle$ become comparable for the two AMPs (220 ± 170 s vs 180 ± 100 s). Averaged over all cells, the second lag time $\langle t_{CM} - t_{OM} \rangle$ remains substantially longer for LL-37 (130 ± 150 s vs 39 ± 17 s), and again the difference is dominated by the long lag times for LL-37 to disrupt the CM of septating cells. Perhaps LL-37 binds to elements within the periplasm more strongly than Cecropin A, and is thus less available for attack on the CM.

As evidenced by Δt_{GFP}, the degree of OM permeability induced by LL-37 is smaller than that produced by Cecropin A. Again comparing 8 μM LL-37 with 2 μM Cecropin A (to make $<t_{OM}>$ comparable), $<\Delta t_{GFP}>$ over all cells is 60 ± 64 s for LL-37 vs 15 ± 10 s for Cecropin A, a factor of four slower. Comparing 4 μM LL-37 with 1 μM Cecropin A, GFP loss is a factor of six slower for LL-37. In contrast, $<\Delta t_{Sytox}>$ is comparable for LL-37 and Cecropin A.

In summary, at comparable concentration relative to the MIC, LL-37 permeabilizes the OM and CM much slower than Cecropin A. In salty solution like growth medium, LL-37 folds into helical bundles and forms oligomers, [41] while Cecropin A exists primarily as monomers. [26] The slow kinetics of LL-37 mediated attack on *E. coli* could be related to the stability of oligomeric bundles within the lipopolysaccharide layer.

Discussion

Localized, Persistent Membrane Disruption Events. For the action of Cecropin A on both the outer and cytoplasmic membranes of *E. coli*, we find clear evidence of *localized* membrane disruption events *that persist and are stable in time*. In some studies of content release from LUVs, membrane disruptions evidently heal over time (graded release kinetics).[2, 27] This may be due to the ability of the LUV to equilibrate the AMP concentration and relieve differential surface pressure across the two leaflets before all content is released. However, experiments on single GUVs have not revealed membrane disruptions that heal over time.[7-11] Such a healing mechanism is presumably not available for the OM of *E. coli*. Cecropin A molecules that translocate into the periplasm may bind to periplasmic components such as the peptidoglycan layer or to the outer leaflet of the cytoplasmic membrane, thus maintaining differential AMP concentration between the outer and inner leaflets of the OM.

Localized permeabilization of the OM of *E. coli* by Cecropin A and LL-37 is inferred from the initial radial asymmetry of the dark patch that gradually symmetrizes and spreads axially as well (Fig. 1). Comparison of the time evolution of the shape of the axial intensity distribution with Monte Carlo simulations indicates that the permeability of the membrane disruption gradually increases over several seconds (Fig. 7B, C). Complete leakage of the periplasmic GFP to the surrounding medium and subsequent entry of Sytox Green across the OM demonstrates that the OM disruption remains for at least several minutes.

For the cytoplasmic membrane, localized disruption is inferred from the small initial spot of Sytox Green fluorescence, which then slowly spreads across the nucleoids. The CM remains permeable to Sytox Green for at least ~2 min, the time scale of Sytox Green staining of the nucleoid, and probably for much longer. The earliest discernible images of Sytox Green are not diffraction limited. For Cecropin A and LL-37 on *E. coli*, we estimate the initial full width at

half-maximum intensity (FWHM) to be 330-440 nm, significantly larger than the diffraction limit of 200 nm FWHM at the emission wavelength of 540 nm. The same was true for LL-37 on *B. subtilis.*[34] The breadth of the initial Sytox Green spots may be due in part to the breadth of the initial membrane disruption, consistent with the inferences from the Monte Carlo simulations. However, the structure of the cytoplasm also plays a role. Under these growth conditions, *E. coli* shows strong segregation of the two nucleoid lobes from three interspersed ribosome-rich regions (cell center and two endcaps).[42] When Sytox Green enters the cytoplasm at either the septal region or an endcap, it must first diffuse through a ribosome-rich region before encountering dense DNA. Some spreading during this transit will inevitably occur.

Our data do not enable us to classify the observed membrane disruptions as pores or carpets. Neither our observations nor the Monte Carlo models can distinguish a well-defined pore[14] from a chaotic pore[19] from a localized "carpet patch"[21] from a leaky hexagonal phase analogue.[22] The simulations of GFP efflux from the periplasmic space demonstrate that within a few seconds, the outer membrane acquires permeability comparable to that of a single pore of ~100 nm diameter. A toroidal pore can in principle expand to any size; in fact, micron-sized, AMP-induced pores were recently observed by AFM in a planar lipid bilayer.[43] However, we expect that rapid formation of such a large pore in the OM would lead to blebbing of the cytoplasm, which is not observed. The GFP loss data are equally consistent with the abrupt formation of *many* smaller pores in a ~100 nm diameter region of space. As is well known in the theory of diffusion to absorbing patches,[39] a sparse set of small absorbers will capture molecules almost as rapidly as a completely absorbing patch covering the same area. In a pore-like model, the increasing OM permeability over several seconds inferred from comparisons with the Monte Carlo simulations would be due to a rapid increase in the number of pores and perhaps also in the area they cover. The permeable region may evolve from a localized patch to a ribbon

surrounding the septal region, as suggested in the examples in Figs. 1 and 7B, C. The GFP release data are also consistent with formation of a localized, highly permeable "carpet patch" of at least 100 nm diameter that subsequently spreads.

Formation of the initial membrane disruption takes minutes, but the subsequent enhancement of the permeability occurs over only a few seconds. This suggests that successful nucleation of the initial localized permeabilization site lowers the free energy barrier to formation of a larger permeabilization region, a kind of "cooperativity of permeabilization".

Preferential Attack at Curved Membrane Surfaces. Both Cecropin A and LL-37 attack septating cells earlier than non-septating cells. For septating cells, both AMPs always permeabilize the OM in the septal region. This is the region of active biosynthesis of curved cell wall, including the lipopolysaccharide layer, underlying membrane, and the peptidoglycan layer. For non-septating cells, both Cecropin A and LL-37 permeabilize the OM at one endcap, where no cell wall synthesis is occurring. Intriguingly, in the five cells observed for sufficient time, Cecropin A permeabilizes the *new* pole (the site of the most recent septation) of non-septating cells in preference to the old pole. The septal region of septating cells and the new pole of non-septating cells both contain elements of the divisome machinery. Labeling studies have shown that in newborn cells, the poles and division septum are enriched in anionic phospholipids such as cardiolipin.[44] The septal region is also the site of initiation of DNA replication by DnaA.[45] It is possible that a cardiolipin-rich domain at the septum recruits the DNA replication machinery, and subsequent tly, the early cell division proteins such as FtsZ, FtsA and ZipA.[46] Following cell division, cardiolipin might persist at the new pole before eventually migrating to the next division site. Cardiolipin is known to be present on the outer leaflet of the OM. Our data suggest that the special composition of the curved outer membrane at a septum or a new pole somehow facilitates permeabilization by Cecropin A. In a pore model of membrane disruption, the

positively curved cardiolipin might alleviate strain at the curved edge of a toroidal pore.[47] It might also be useful in nucleating a highly curved hexagonal-like phase.

The axial distribution of OM and CM permeabilization events is quite different for LL-37 and Cecropin A (Figs. 8 and S11). Evidently peptide sequence strongly affects the point of attack. For septating cells, LL-37 typically permeabilizes the CM at the septal region, the same location as the OM permeabilization. For non-septating cells, LL-37 permeabilizes both the OM and CM near the same end cap. In contrast, Cecropin A permeabilizes the CM far from the initial entry point into the periplasm (Fig. 3, 8, S11). The explanation is not obvious. While the length and net charge of the two peptides are similar, the distribution of charges along the sequence is quite different. In LL-37, positive and negative charges are widely distributed, while in Cecropin A the helix nearest to the N-terminus (residues 8-21) contains most of the charges and the other helix (residues 25-37) is mainly hydrophobic.

Kinetics of Membrane Disruption. This study of unlabeled Cecropin A lacks key ingredients necessary to build a quantitative kinetics model of membrane disruption, so the discussion that follows is necessarily speculative. Without flowing Cecropin A through the observation chamber, the bulk concentration remains ill-defined. More importantly, we lack information about the time-dependent concentration of Cecropin A *at the cell surface*, within the lipopolysaccharide (LPS)/outer membrane layer. Finally, we do not know the diffusion coefficient of Cecropin A within the LPS layer.

Nevertheless, the present results allow us to infer several qualitative features of the membrane disruption mechanism. Disruption of the OM by Cecropin A is a rare event that occurs only after a mean lag time of 2–9 min. A possibly analogous lag time has been observed in kinetics measurements of the disruption of GUVs by various AMPs.[10, 11, 16] Above a threshold bulk Cecropin A concentration, the mean lag time $<t_{OM}>$ to OM permeabilization decreases with

increasing bulk concentration, but only roughly linearly (Table 1). The mean lag time $<(t_{OM} - t_{CM})>$ between OM permeabilization and CM permeabilization is also weakly dependent on bulk Cecropin A concentration and shows no threshold. This suggests that any Cecropin A concentration sufficiently high to permeabilize the OM quickly creates a periplasmic Cecropin A concentration that lies well above the threshold for permeabilization of the CM.

The long lag time to OM permeabilization might arise from slow uptake of AMPs by the LPS layer. However, our earlier study of Rhodamine-labeled LL-37[33] and unpublished data on Rhodamine-labeled Cecropin A indicate that for both septating and non-septating cells the AMP equilibrates between the lipopolysaccharide layer (LPS) and the bulk in less than 1 min. Disruption of the OM typically occurs only after a much longer lag time. Evidently the lag time to OM permeabilization is not primarily due to slow accumulation of Cecropin A within the LPS layer. Alternatively, slow diffusion within the LPS layer might severely limit the ability of Cecropin A to reach the membrane and disrupt it. Future studies using fluorescently labeled Cecropin A will provide quantitative data on the rate of equilibration of the bulk and surface-bound populations and also the diffusion constant of Cecropin A within the LPS layer.

The long lag times to OM and CM permeabilization combined with the existence of a threshold concentration for OM permeabilization suggest that membrane disruption involves a nucleation step that is rare and difficult due to a large free energy barrier. Suppose nucleation of a pore-like structure involved cooperative, simultaneous insertion of *multiple* Cecropin A monomers into the bilayer. Then classical nucleation theory predicts that the mean lag time to formation of a multi-peptide disruption from monomers scales as $[M]^n$, where [M] is the surface concentration of monomer and n is the number of monomers in the critical nucleus configuration.[48] Yet the observed mean lag time to OM permeabilization decreases only roughly

linearly with *bulk* Cecropin A concentration, not as some higher power as suggested by nucleation theory. A remarkably similar combination of observations was made for Bax-mediated pore formation in isolated mitochondrial outer membranes.[49] The lag time to membrane disruption was highly variable, but the mean rate of pore formation depended only linearly on the Bax concentration.

It is possible that for Cecropin A, the threshold surface concentration for pore formation in the OM is not much smaller than the saturation limit for binding of peptide to the LPS layer. If so, then the equilibrium surface concentration would change only slowly with bulk concentration in the regime that induces pores. The critical number *n* could still be substantial and nucleation theory could still hold. Future measurement of lag time distributions vs *surface* Cecropin A concentration using labeled peptide are an important next step. If a linear dependence of mean lag time on surface concentration is observed, it may prove useful to consider "lipocentric" models of pore formation, in which the peptide serves as a kind of catalyst that induces tension within the bilayer and then stabilizes the resulting transient pores.[50]

Acknowledgments

A helpful discussion with Prof. Qiang Cui is gratefully acknowledged.

Supporting Information

Supporting Information includes: (1) Explanation of how axial and transverse intensity profiles are created. (2) Definition of the relative axial coordinate system x_{rel} and explanation of how we estimate the axial positions at which the OM is permeabilized to GFP and the CM is permeabilized to Sytox Green. (3) Additional histograms of the timing and duration of permeabilization events at nominal 1 μM and 2 μM bulk Cecropin A concentration. (4) Figure S6 showing the subtle slowing of growth rate immediately after Cecropin A addition. (5) Further details of how the Monte Carlo simulations are carried out, plus figures showing one model trajectory and how the model outcomes depend on input parameters. (6) Comparison of the attack of Cecropin A and LL-37 on a septating cell. (7) Table S1, describing timing and duration of permeabilization events for LL-37 attacking *E. coli*. (8) A movie showing the attack of Cecropin A on one septating cell and one non-septating cell. This material is available free of charge via the Internet at http://pubs.acs.org.

References

1. Wang, Z., and Wang, G. (2004) APD: the Antimicrobial Peptide Database, *Nucleic Acids Res 32*, D590-592.
2. Wimley, W. C., and Hristova, K. (2011) Antimicrobial peptides: successes, challenges and unanswered questions, *The Journal of membrane biology 239*, 27-34.
3. Brogden, K. A. (2005) Antimicrobial peptides: pore formers or metabolic inhibitors in bacteria?, *Nature reviews. Microbiology 3*, 238-250.
4. Mowery, B. P., Lindner, A. H., Weisblum, B., Stahl, S. S., and Gellman, S. H. (2009) Structure-activity relationships among random nylon-3 copolymers that mimic antibacterial host-defense peptides, *Journal of the American Chemical Society 131*, 9735-9745.
5. Clark, K. S., Svetlovics, J., McKeown, A. N., Huskins, L., and Almeida, P. F. (2011) What determines the activity of antimicrobial and cytolytic peptides in model membranes, *Biochemistry 50*, 7919-7932.
6. Almeida, P. F., and Pokorny, A. (2009) Mechanisms of antimicrobial, cytolytic, and cell-penetrating peptides: from kinetics to thermodynamics, *Biochemistry 48*, 8083-8093.
7. Hung, W. C., Chen, F. Y., Lee, C. C., Sun, Y., Lee, M. T., and Huang, H. W. (2008) Membrane-thinning effect of curcumin, *Biophys J 94*, 4331-4338.
8. Huang, H. W. (2006) Molecular mechanism of antimicrobial peptides: the origin of cooperativity, *Biochim Biophys Acta 1758*, 1292-1302.
9. Huang, H. W., Chen, F. Y., and Lee, M. T. (2004) Molecular mechanism of Peptide-induced pores in membranes, *Physical review letters 92*, 198304.

10. Tamba, Y., Ohba, S., Kubota, M., Yoshioka, H., Yoshioka, H., and Yamazaki, M. (2007) Single GUV method reveals interaction of tea catechin (-)-epigallocatechin gallate with lipid membranes, *Biophys J 92*, 3178-3194.

11. Tamba, Y., and Yamazaki, M. (2005) Single giant unilamellar vesicle method reveals effect of antimicrobial peptide magainin 2 on membrane permeability, *Biochemistry 44*, 15823-15833.

12. Wimley, W. C. (2010) Describing the mechanism of antimicrobial peptide action with the interfacial activity model, *ACS chemical biology 5*, 905-917.

13. Qian, S., Wang, W., Yang, L., and Huang, H. W. (2008) Structure of the alamethicin pore reconstructed by x-ray diffraction analysis, *Biophys J 94*, 3512-3522.

14. Lee, C. C., Sun, Y., Qian, S., and Huang, H. W. (2011) Transmembrane pores formed by human antimicrobial peptide LL-37, *Biophys J 100*, 1688-1696.

15. Lee, E., Jeong, K. W., Lee, J., Shin, A., Kim, J. K., Lee, J., Lee, D. G., and Kim, Y. (2013) Structure-activity relationships of cecropin-like peptides and their interactions with phospholipid membrane, *BMB reports 46*, 282-287.

16. Lee, M. T., Hung, W. C., Chen, F. Y., and Huang, H. W. (2008) Mechanism and kinetics of pore formation in membranes by water-soluble amphipathic peptides, *Proc Natl Acad Sci U S A 105*, 5087-5092.

17. Schlamadinger, D. E., Wang, Y., McCammon, J. A., and Kim, J. E. (2012) Spectroscopic and computational study of melittin, cecropin A, and the hybrid peptide CM15, *The journal of physical chemistry. B 116*, 10600-10608.

18. Leontiadou, H., Mark, A. E., and Marrink, S. J. (2006) Antimicrobial peptides in action, *Journal of the American Chemical Society 128*, 12156-12161.

19. Axelsen, P. H. (2008) A chaotic pore model of polypeptide antibiotic action, *Biophys J 94*, 1549-1550.

20. Shai, Y. (2002) Mode of action of membrane active antimicrobial peptides, *Biopolymers 66*, 236-248.

21. Shai, Y. (1999) Mechanism of the binding, insertion and destabilization of phospholipid bilayer membranes by alpha-helical antimicrobial and cell non-selective membrane-lytic peptides, *Biochim Biophys Acta 1462*, 55-70.

22. Schmidt, N. W., Tai, K. P., Kamdar, K., Mishra, A., Lai, G. H., Zhao, K., Ouellette, A. J., and Wong, G. C. (2012) Arginine in alpha-defensins: differential effects on bactericidal activity correspond to geometry of membrane curvature generation and peptide-lipid phase behavior, *The Journal of biological chemistry 287*, 21866-21872.

23. Yang, L., Gordon, V. D., Mishra, A., Som, A., Purdy, K. R., Davis, M. A., Tew, G. N., and Wong, G. C. (2007) Synthetic antimicrobial oligomers induce a composition-dependent topological transition in membranes, *Journal of the American Chemical Society 129*, 12141-12147.

24. Steiner, H., Hultmark, D., Engstrom, A., Bennich, H., and Boman, H. G. (1981) Sequence and specificity of two antibacterial proteins involved in insect immunity, *Nature 292*, 246-248.

25. Marassi, F. M., Opella, S. J., Juvvadi, P., and Merrifield, R. B. (1999) Orientation of cecropin A helices in phospholipid bilayers determined by solid-state NMR spectroscopy, *Biophys J 77*, 3152-3155.

26. Silvestro, L., and Axelsen, P. H. (2000) Membrane-induced folding of cecropin A, *Biophys J 79*, 1465-1477.

27. Gregory, S. M., Cavenaugh, A., Journigan, V., Pokorny, A., and Almeida, P. F. (2008) A quantitative model for the all-or-none permeabilization of phospholipid vesicles by the antimicrobial peptide cecropin A, *Biophys J 94*, 1667-1680.

28. Wade, D., Boman, A., Wahlin, B., Drain, C. M., Andreu, D., Boman, H. G., and Merrifield, R. B. (1990) All-D amino acid-containing channel-forming antibiotic peptides, *Proc Natl Acad Sci U S A 87*, 4761-4765.

29. Steiner, H., Andreu, D., and Merrifield, R. B. (1988) Binding and action of cecropin and cecropin analogues: antibacterial peptides from insects, *Biochim Biophys Acta 939*, 260-266.

30. Christensen, B., Fink, J., Merrifield, R. B., and Mauzerall, D. (1988) Channel-forming properties of cecropins and related model compounds incorporated into planar lipid membranes, *Proc Natl Acad Sci U S A 85*, 5072-5076.

31. Silvestro, L., Gupta, K., Weiser, J. N., and Axelsen, P. H. (1997) The concentration-dependent membrane activity of cecropin A, *Biochemistry 36*, 11452-11460.

32. Silvestro, L., Weiser, J. N., and Axelsen, P. H. (2000) Antibacterial and antimembrane activities of cecropin A in Escherichia coli, *Antimicrob Agents Chemother 44*, 602-607.

33. Sochacki, K. A., Barns, K. J., Bucki, R., and Weisshaar, J. C. (2011) Real-time attack on single Escherichia coli cells by the human antimicrobial peptide LL-37, *Proc Natl Acad Sci U S A 108*, E77-81.

34. Barns, K. J., and Weisshaar, J. C. (2013) Real-time attack of LL-37 on single Bacillus subtilis cells, *Biochim Biophys Acta 1828*, 1511-1520.

35. Neidhardt, F. C., Bloch, P. L., and Smith, D. F. (1974) Culture medium for enterobacteria, *J Bacteriol 119*, 736-747.

36. Sochacki, K. A., Shkel, I. A., Record, M. T., and Weisshaar, J. C. (2011) Protein diffusion in the periplasm of E. coli under osmotic stress, *Biophys J 100*, 22-31.

37. Sargent, F. (2007) The twin-arginine transport system: moving folded proteins across membranes, *Biochemical Society transactions 35*, 835-847.

38. Hong, R. W., Shchepetov, M., Weiser, J. N., and Axelsen, P. H. (2003) Transcriptional profile of the Escherichia coli response to the antimicrobial insect peptide cecropin A, *Antimicrob Agents Chemother 47*, 1-6.

39. Berg, H. C. (1993) *Random Walks in Biology*, Princeton University Books.

40. Porcelli, F., Verardi, R., Shi, L., Henzler-Wildman, K. A., Ramamoorthy, A., and Veglia, G. (2008) NMR structure of the cathelicidin-derived human antimicrobial peptide LL-37 in dodecylphosphocholine micelles, *Biochemistry 47*, 5565-5572.

41. Oren, Z., Lerman, J. C., Gudmundsson, G. H., Agerberth, B., and Shai, Y. (1999) Structure and organization of the human antimicrobial peptide LL-37 in phospholipid membranes: relevance to the molecular basis for its non-cell-selective activity, *Biochem J 341 (Pt 3)*, 501-513.

42. Bakshi, S., Siryaporn, A., Goulian, M., and Weisshaar, J. C. (2012) Superresolution imaging of ribosomes and RNA polymerase in live Escherichia coli cells, *Mol Microbiol 85*, 21-38.

43. Rakowska, P. D., Jiang, H., Ray, S., Pyne, A., Lamarre, B., Carr, M., Judge, P. J., Ravi, J., UI, M. G., Koksch, B., Martyna, G. J., Hoogenboom, B. W., Watts, A., Crain, J., Grovenor, C. R., and Ryadnov, M. G. (2013) Nanoscale imaging reveals laterally expanding antimicrobial pores in lipid bilayers, *Proc Natl Acad Sci U S A 110*, 8918-8923.

44. Mileykovskaya, E., and Dowhan, W. (2009) Cardiolipin membrane domains in prokaryotes and eukaryotes, *Biochim Biophys Acta 1788*, 2084-2091.

45. Pogliano, K., Pogliano, J., and Becker, E. (2003) Chromosome segregation in Eubacteria, *Curr Opin Microbiol 6*, 586-593.

46. Lutkenhaus, J., Pichoff, S., and Du, S. (2012) Bacterial cytokinesis: From Z ring to divisome, *Cytoskeleton 69*, 778-790.

47. Lee, M. T., Hung, W. C., Chen, F. Y., and Huang, H. W. (2005) Many-body effect of antimicrobial peptides: on the correlation between lipid's spontaneous curvature and pore formation, *Biophys J 89*, 4006-4016.

48. Powers, E. T., and Powers, D. L. (2006) The kinetics of nucleated polymerizations at high concentrations: amyloid fibril formation near and above the "supercritical concentration", *Biophys J 91*, 122-132.

49. Kushnareva, Y., Andreyev, A. Y., Kuwana, T., and Newmeyer, D. D. (2012) Bax activation initiates the assembly of a multimeric catalyst that facilitates Bax pore formation in mitochondrial outer membranes, *PLoS Biol 10*, e1001394.

50. Fuertes, G., Gimenez, D., Esteban-Martin, S., Sanchez-Munoz, O. L., and Salgado, J. (2011) A lipocentric view of peptide-induced pores, *Eur Biophys J 40*, 399-415.

Table 1. Summary of mean timing data for OM and CM permeabilization of *E. coli* by Cecropin A.[a]

	Nominal Bulk Cecropin A Concentration		
	1 μM	**2 μM**	**4 μM**
N_{tot} **(All cells)**	**43**	**54**	**7**
$\langle t_{OM} \rangle$	540 ± 300	183 ± 99	108 ± 51
$\langle t_{CM} \rangle$	601 ± 310	222 ± 97	129 ± 49
$\langle t_{CM} - t_{OM} \rangle$	64 ± 53	39 ± 17	21 ± 9
$\langle \Delta t_{GFP} \rangle$	22 ± 21 (N = 36)	15 ± 10 (N = 52)	15 ± 6
$\langle \Delta t_{Sytox} \rangle$	98 ± 47	92 ± 44	117 ± 47
N_{sept} **(septating)**	**13**	**18**	**3**
$\langle t_{OM} \rangle$	350 ± 120	100 ± 39	62 ± 9
$\langle t_{CM} \rangle$	410 ± 140	147 ± 45	84 ± 6
$\langle t_{CM} - t_{OM} \rangle$	63 ± 39	47 ± 14	22 ± 9
$\langle \Delta t_{GFP} \rangle$	23 ± 12 (N = 12)	17 ± 8	18 ± 6
$\langle \Delta t_{Sytox} \rangle$	85 ± 31	71 ± 23	78 ± 12
$N_{non\text{-}sept}$ **(non-septating)**	**30**	**36**	**4**
$\langle t_{OM} \rangle$	620 ± 320	225 ± 94	143 ± 38
$\langle t_{CM} \rangle$	680 ± 330	259 ± 95	164 ± 34
$\langle t_{CM} - t_{OM} \rangle$	65 ± 59	34 ± 17	21 ± 9
$\langle \Delta t_{GFP} \rangle$	22 ± 25 (N = 24)	14 ± 11 (N = 34)	15 ± 6
$\langle \Delta t_{Sytox} \rangle$	104 ± 52 (N = 29)	103 ± 49	117 ± 47

[a] All times in seconds. The ± values are one standard deviation of single measurements. *N* values give the number of cells in calculation of each mean.

Figures

Figure 1. Sequence of events for a septating cell at 2 μM nominal Cecropin A concentration. The overall sequence over 10 min is shown in the top row, while expanded views of GFP loss and Sytox Green entry are shown in the bottom row. Note left-right asymmetry in loss of GFP from septal region in first three frames after t = 1.00 min. Also note punctal entry of Sytox Green into the cytoplasm at t = 1.68 min.

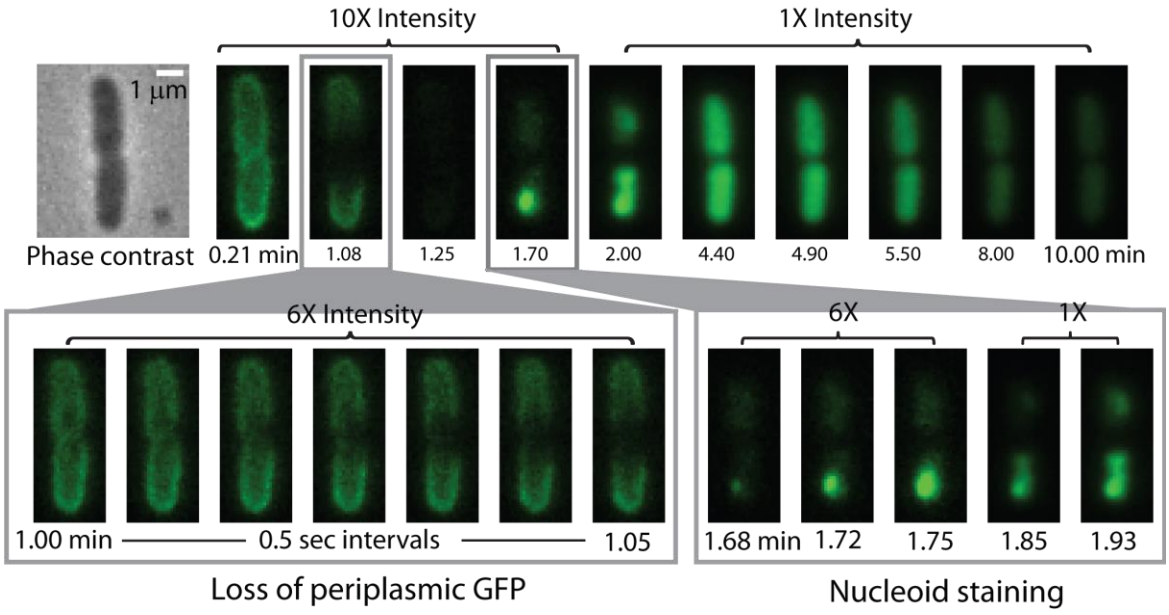

Figure 2. Sequence of events for a non-septating cell at 2 μM nominal Cecropin A concentration. The overall sequence over 5 min is shown in the top row, while expanded views of GFP loss and Sytox Green entry are shown in the bottom row. Note loss of GFP from one endcap (2–4 frames after t = 3.26 min) and predominantly punctal initial staining by Sytox Green.

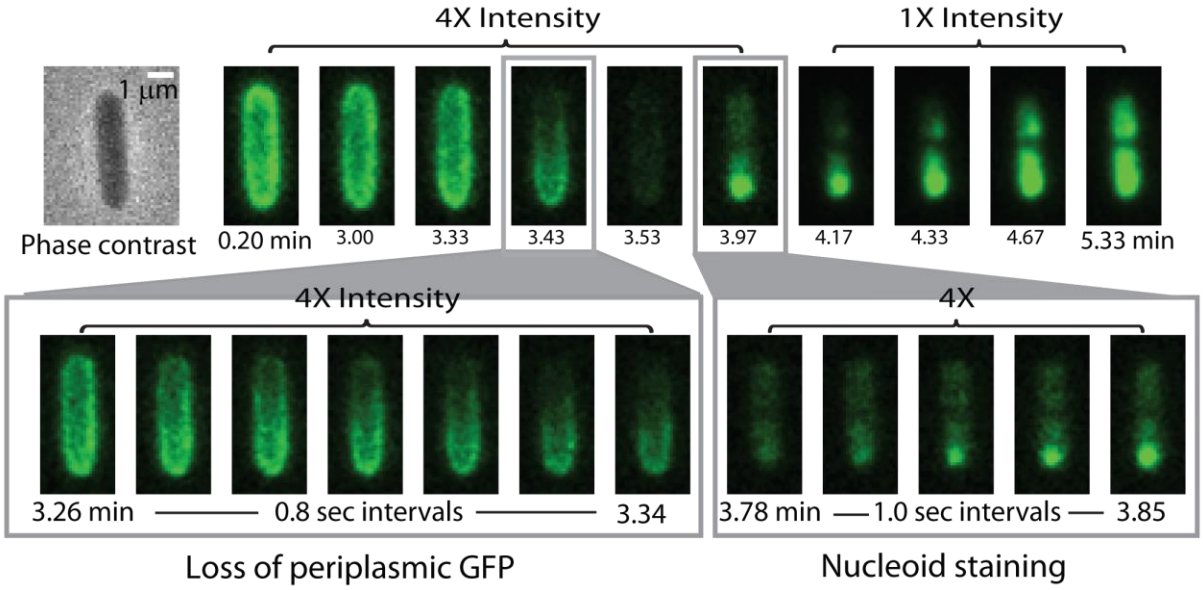

Figure 3. Correlation of axial locations of GFP loss vs Sytox Green entry, with axial location defined on a relative scale from 0 to 1 (tip-to-tip). For non-septating cells (circles), 0 is chosen at the end of the cell from which GFP leaves. Sytox Green tends to enter the cytoplasm at locations distant from the GFP exit point. For septating cells (triangles), choice of 0 is arbitrary. GFP leaves near the septum, while Sytox Green enters near one pole. See Supporting Information for details of measurements.

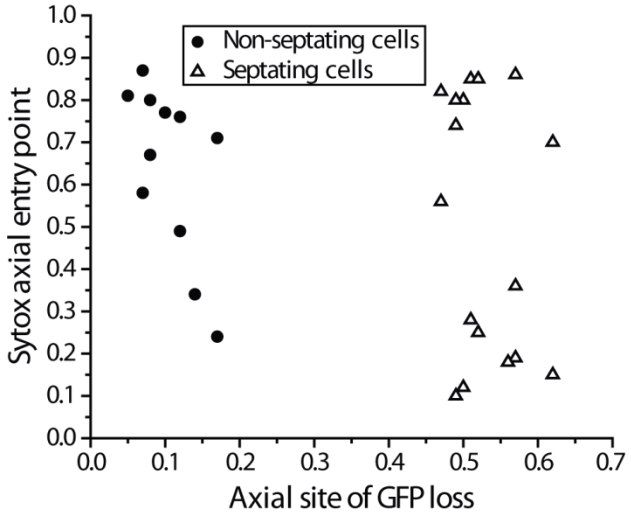

Figure 4. Plot of green fluorescence intensity (green) and cell length (black) vs time for one non-septating cell at nominal Cecropin A concentration of 2 μM. Laser is turned on just prior to Cecropin A injection at $t = 0$. Lag times to onset of GFP loss from periplasm (t_{OM}) and to Sytox Green entry into cytoplasm (t_{CM}) are shown. Time intervals required for loss of GFP from periplasm (Δt_{GFP}) and entry of Sytox Green into cytoplasm (Δt_{Sytox}) are also indicated.

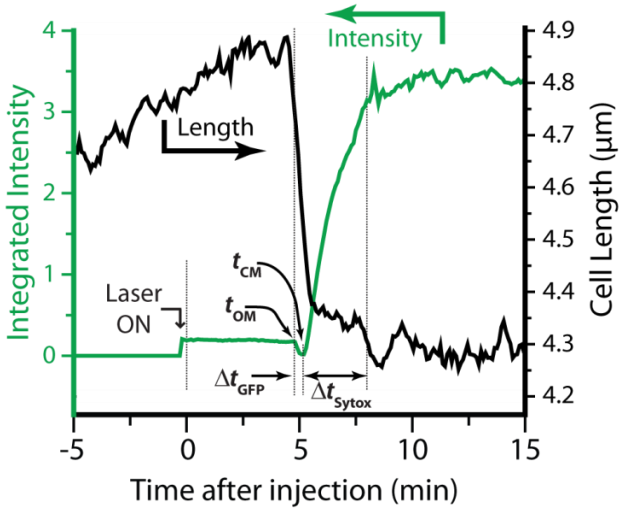

Figure 5. Histograms of timing events for onset of permeabilization of outer and cytoplasmic membranes. **A**: Comparison of distribution of t_{OM} for septating vs non-septating cells at nominal 2 μM Cecropin A. **B**: Comparison of distribution of t_{OM} for all cells at nominal 1 μM vs 2 μM Cecropin A. **C**: Comparison of distribution of ($t_{CM} - t_{OM}$) for all cells at nominal 1 μM vs 2 μM Cecropin A. Bin width is 25 s in Panel A, 50 s in Panel B, and 10 s in Panel C.

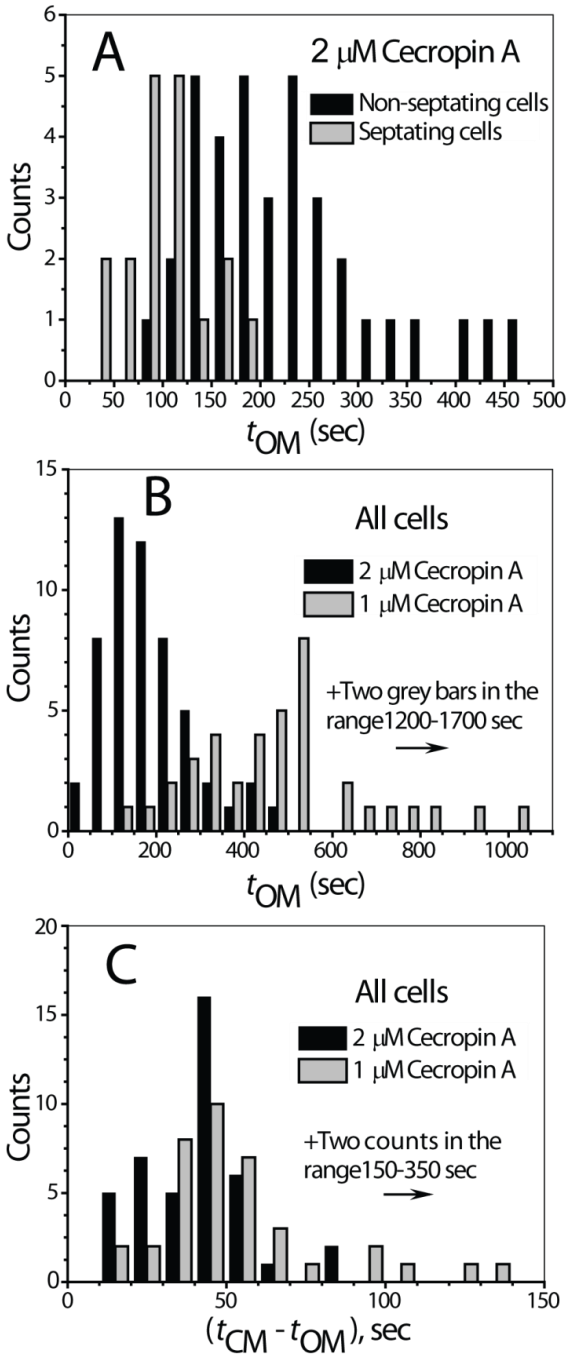

Figure 6. Expanded view of loss of periplasmic GFP for two cells, both septating, at nominal Cecropin A concentration of 2 μM. Most cells exhibit the abrupt loss behavior; see text.

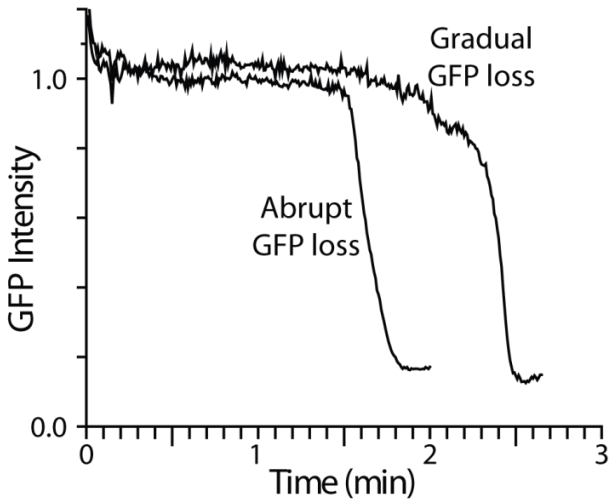

Figure 7. Monte Carlo simulations of GFP loss from periplasm. **A**: Model geometry for circular pore (both septal and endcap) and for annular ribbon. **B**: Comparison of GFP loss from one septating cell (Expt data) with different models as shown. **C**: Two-dimensional experimental images and axial profiles from the same cell as in **B** (center) compared with models. At left is 100 nm pore with D_{peri} = 0.5 μm^2-s^{-1}; at right is 3 nm annular ribbon with the same D_{peri} = 0.5 μm^2-s^{-1}. The model at left fits the data reasonably well at short times, but does not decay sufficiently over 10 s. The model at right decays too fast at short times but fits the data reasonably well at longer times.

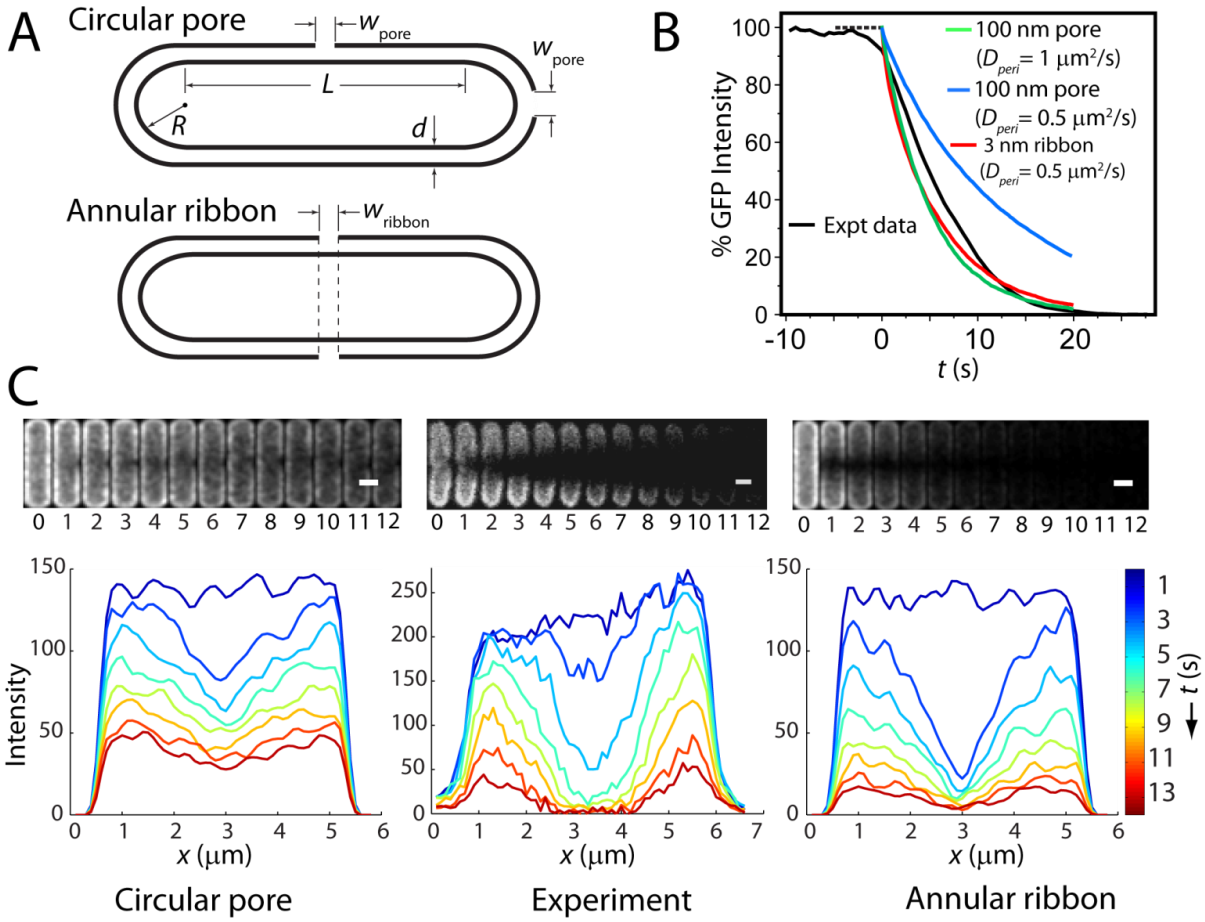

Figure 8. Comparison of the typical attack mode of (**A**) LL-37 and (**B**) Cecropin A on non-septating cells. Both attack the OM at one endcap; LL-37 attacks the CM at the *same* endcap but Cecropin A attacks the CM at the *opposite* endcap. For (**A**) and (**B**), the two images and axial linescans at left were obtained just before and just after OM permeabilization to GFP. Subtraction of the two linescans makes the grey difference plot, whose maximum determines x_{rel} for the OM permeabilization event. The image and linescan at right shows the initial localized Sytox Green signal. We determine x_{rel} for CM permeabilization from the peak position of the axial linescan. See also Supporting Information (Fig. S2).

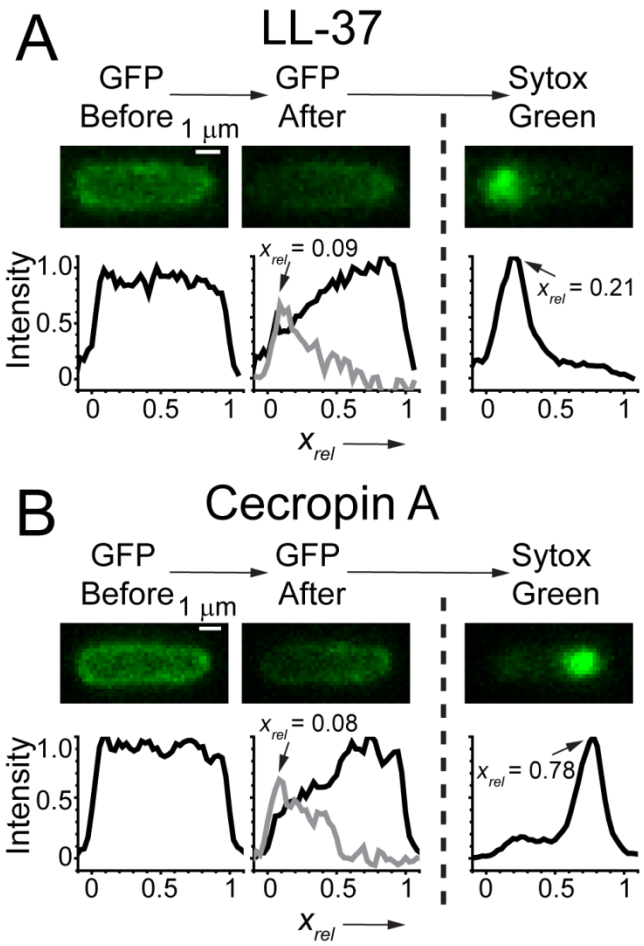

Supporting Information

Axial and transverse intensity profiles

To generate an axial intensity profile (or axial linescan) in ImageJ, fluorescence intensity was integrated for all the pixels along the short cell axis *y* at each *x* and plotted against *x*. See Fig. 7.

To generate a transverse intensity profile (Fig. S1), a line segment of variable width was drawn along the short, *y* axis of the cell. For each *y* value, fluorescence intensity was integrated for all *x* values within the width of the segment drawn. The transverse profile of the initial periplasmic GFP distribution has two peaks corresponding to the projection onto the *xy* plane of the shell of fluorescence from the periplasmic GFP (Fig. S1). The dip between the peaks is primarily due to periplasmic GFP at the top and bottom of the cell, plus fluorescence from GFP molecules that remain in the cytoplasm and some cell autofluorescence.

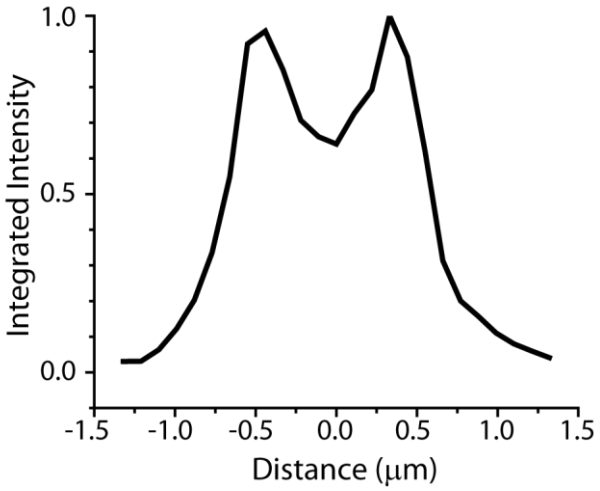

Figure S1. Transverse intensity linescan of the periplasmic GFP fluorescence prior to membrane permeabilization.

Relative axial coordinate of permeabilization events

To place locations of OM and CM permeabilization events for different cells on a common relative axial scale, we form an axial linescan (along the long axis *x*) for an image just prior to OM permeabilization. The two pixels closest to the full width at half-maximum height (FWHM) points were defined as the locations of x_{rel} = 0 and 1. In non-septating cells, x_{rel} = 0 was assigned

to the cell tip near which GFP loss began. In septating cells, the assignment of x_{rel} = 0 was arbitrary.

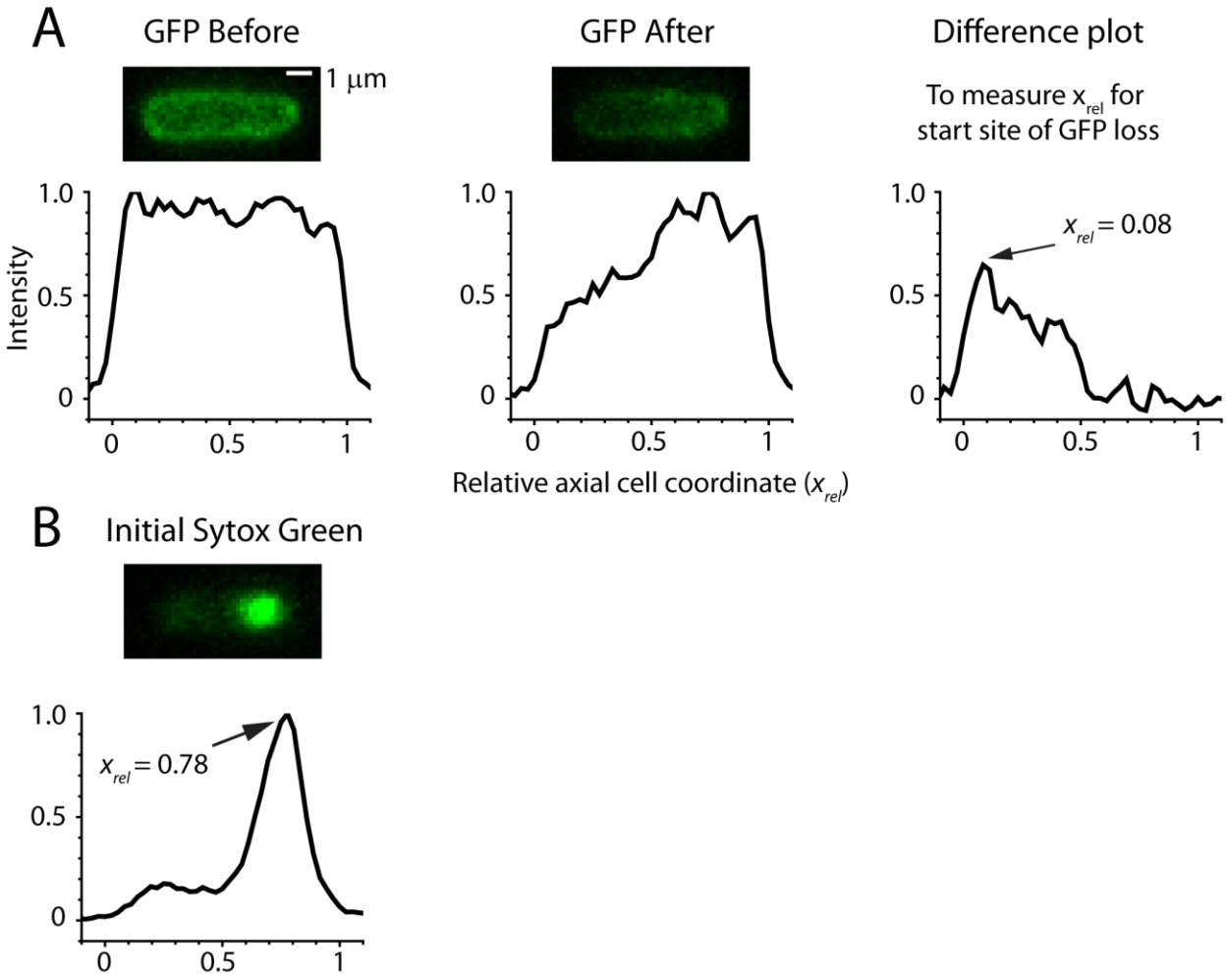

Figure S2. (A) Examples of axial linescans immediately before and after permeabilization of the OM and the difference plot. The axial location of the event is chosen at the intensity peak of the difference plot. (B) Axial linescan immediately after permeabilization of the CM. The axial location of the event is chosen at the peak in intensity.

To estimate the axial location of the onset of GFP loss, we form the axial linescan for the cell image taken immediately after GFP loss begins (Fig. S2) and subtract the axial linescan of the "after" image from that of the "before" image. The difference linescan exhibits a local maximum corresponding to the distribution of the lost GFP (Fig. S2). The location of the onset of OM permeabilization was taken as the value of x_{rel} at the local maximum of the difference plot. Similarly, for the CM a cell image was chosen immediately after the appearance of the initial bright dot of Sytox Green fluorescence. The axial linescan for this image featured a peak, and the location of the onset of CM permeabilization was taken as the value of x_{rel} at the peak. See Figs. 8 and S11 for other examples.

Scatter plots for septating and non-septating cells (Fig. 3) were generated by plotting the location of OM permeabilization against the location of CM permeabilization for each cell that exhibited both behaviors clearly.

Additional histograms of timing and duration of permeabilization events

Figures S3, S4, and S5 present additional histograms of $t_{OM,}$ t_{CM}, ($t_{CM} - t_{OM}$), Δt_{GFP}, and Δt_{Sytox} for the data at nominal 1 μM and 2 μM bulk Cecropin A concentration, obtained as described in the main text. Figure S3 combines both septating and non-septating cells, while Figs. S4 and S5 show data for septating cells alone and for non-septating cells alone. The lag time t_{OM} shows a substantial concentration dependence (see also 4 μM data in Table 1). The lag time ($t_{CM} - t_{OM}$) between OM and CM permeabilization is much less sensitive to concentration, as is also true for the GFP release time Δt_{GFP} and the Sytox Green entry time Δt_{Sytox}.

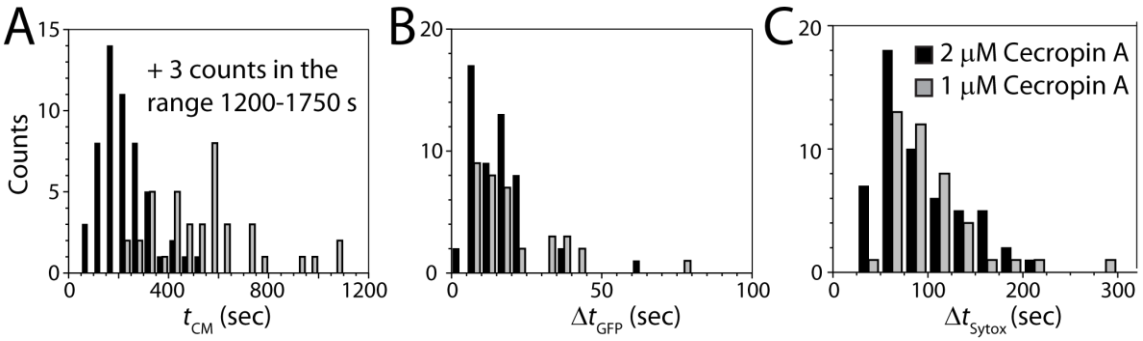

Figure S3. Histograms combining all cells, septating and non-septating, at 1 μM (grey bars) and 2 μM Cecropin A (black bars). See Fig. 5 of main text for t_{OM} and ($t_{CM} - t_{OM}$). **A.** Lag time to permeabilization of CM, t_{CM}. **B.** GFP release time, Δt_{GFP}. **C.** Sytox Green entry time, Δt_{Sytox}.

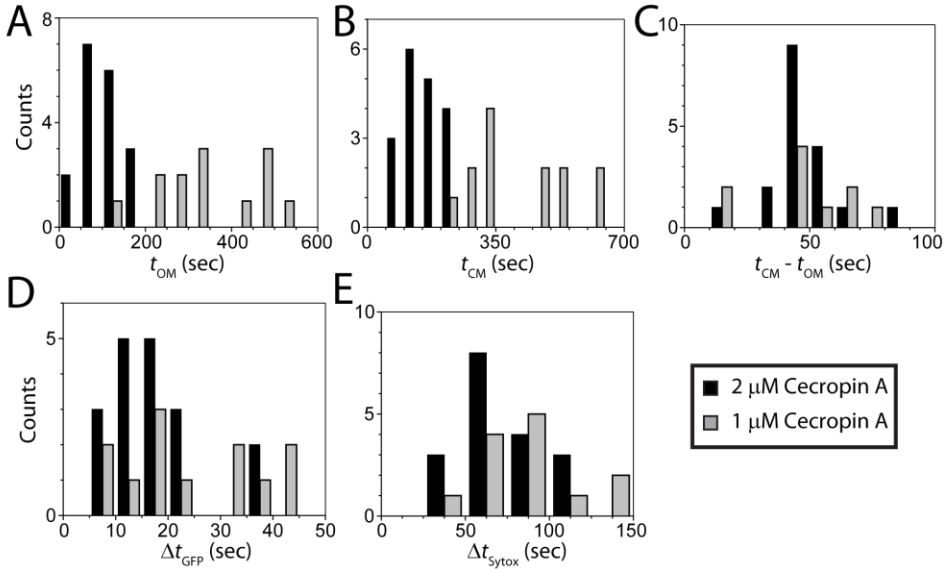

Figure S4. Histograms for septating cells only, at 1 μM (grey bars) and 2 μM Cecropin A (black bars). **A:** Lag time to permeabilization of OM, t_{OM}. **B:** Lag time to permeabilization of CM, t_{CM}. **C:** ($t_{CM} - t_{OM}$). **D:** GFP release time, Δt_{GFP}. **E:** Sytox Green entry time, Δt_{Sytox}.

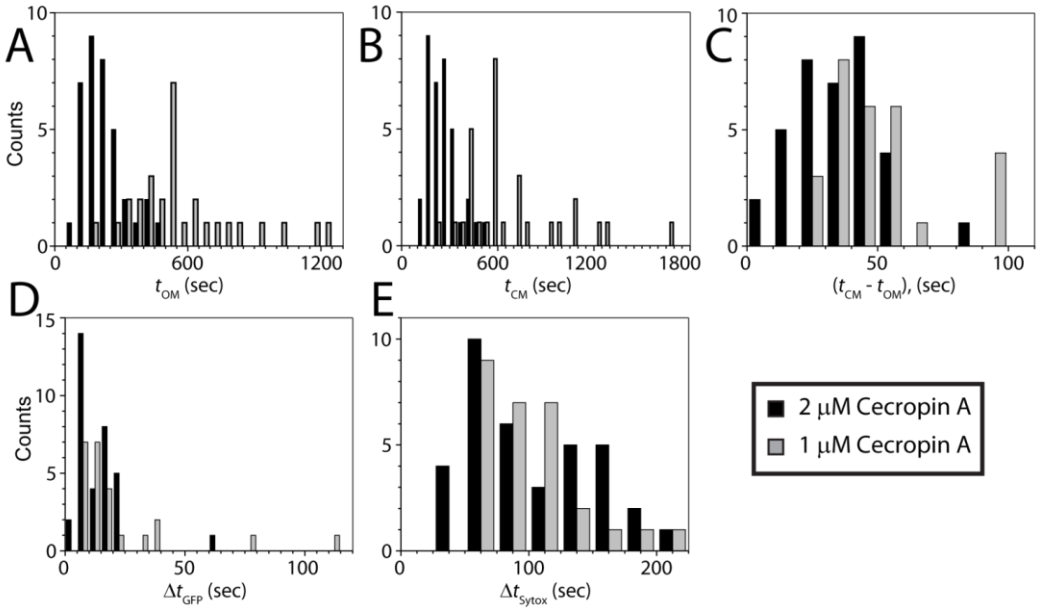

Figure S5. Histograms for non-septating cells only, at 1 μM (grey bars) and 2 μM Cecropin A (black bars). **A:** Lag time to permeabilization of OM, t_{OM}. **B:** Lag time to permeabilization of CM, t_{CM}. **C:** ($t_{CM} - t_{OM}$). **D:** GFP release time, Δt_{GFP}. **E:** Sytox Green entry time, Δt_{Sytox}.

Slowing of growth rate shortly after injection of Cecropin A

It is a subtle effect, but we sometimes observe a change in curvature of cell length vs time shortly after addition of Cecropin A and well before GFP exits and the cell shrinks. In exponential growth, $L(t)$ curves upward. In the plot in Fig. S6, $L(t)$ begins to curve downward for $t > 0$, the point of Cecropin A injection.

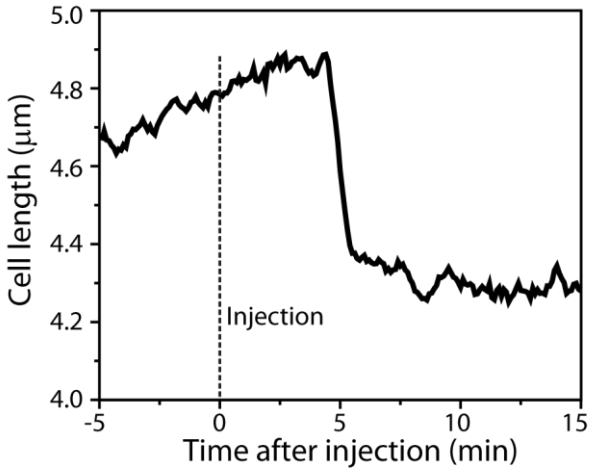

Figure S6. Decrease in growth rate shortly after injection of Cecropin A.

Monte Carlo simulations of GFP efflux from the periplasmic space

The periplasm is modeled as a thin, three-dimensional space sandwiched by two nested spherocylinders (Fig. 7A). The inner spherocylinder has a straight, cylindrical length L and endcap radius of R. The outer spherocylinder has the same cylindrical length of L, but the endcap radius is (R + d), where d is the thickness of the model periplasmic space. The average tip-to-tip length of an *E. coli* cell in our growth conditions is ~5 μm. In earlier work under the same growth conditions, we measured the radius of *E. coli* cytoplasm to be 400 ± 25 nm.[1] Therefore, we fixed the values L = 4.1 μm and R = 400 nm. Cryo-transmission electron microscopy on frozen-hydrated sections of *E. coli* estimated the thickness of the periplasm to be ~ 20 nm.[2] The Monte Carlo step size must be small compared to the smallest dimensions, and simulations with such a small value of d were time consuming. We found that the value d = 50 nm shortens the computational time by 9X without significant effect on the timescale of the GFP release.

Initial positions for 20,000 particles were chosen randomly within the thin space. The diffusion coefficient D_{peri} was varied in the range 0.1-5.0 μm^2-s^{-1} to reach semi-quantitative agreement with the observed values of Δt_{GFP} (Table 1). Each particle step along the *x*, *y*, and *z* coordinates is chosen from a Gaussian distribution whose width is determined by D_{peri}. A particle is removed from the simulation whenever it crosses the absorbing surface patch. No "re-crossings" of the surface patch are permitted, meaning that the model yields the fastest possible drainage of GFP through a hole in the OM. In comparison, both a pore of finite thickness and a carpet patch would transmit GFP less efficiently. An example of a simulation trajectory

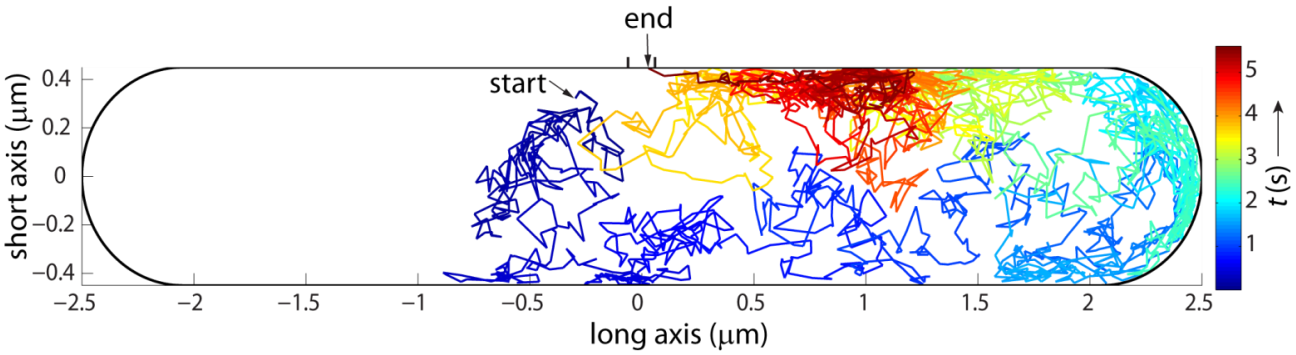

Figure S7. Diffusion to capture by a circular pore at the septum. Advancing time coded by color.

eventually captured by a circular patch at the septum is shown in Fig. S7.

Figures S8 and S9 show the dependence of GFP loss curves on model geometry and on GFP diffusion coefficient for the absorbing annular ribbon at the septum and for a circular absorbing patch placed at one endcap. In Fig. S10, we compare experimental GFP loss from one non-septating cell with the model of a static, circular, absorbing endcap patch with parameter tuned to closely match Δt_{GFP}. The model decays more rapidly than experiment initially, and less rapidly than experiment later. From this we infer that the permeability of the cell is increasing in time.

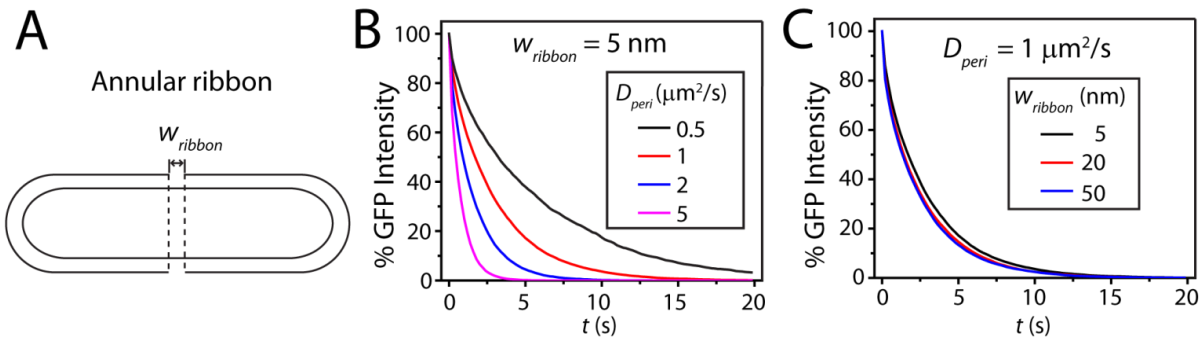

Figure S8. Monte Carlo simulations of GFP loss through an annular ribbon in the OM at the septum. **A**: Model geometry for the ribbon. **B**: Comparison of GFP intensity loss vs time with w_{ribbon} = 5 nm for different values of GFP diffusion constant D_{peri} as shown. **C**: Comparison of GFP intensity loss vs time with D_{peri} = 1 μm^2-s^{-1} and different values of w_{ribbon} as shown. Narrow and wide ribbons capture molecules equally efficiently because whenever a molecule gets close to a ribbon, it has high probability of capture regardless of ribbon width.

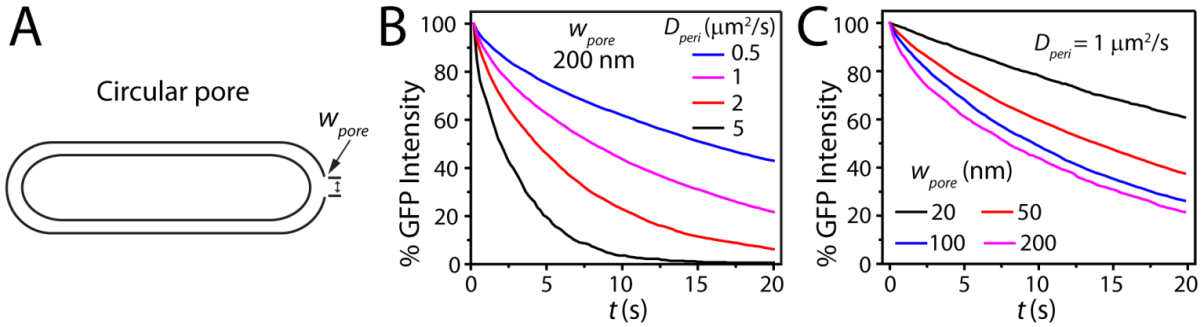

Figure S9. Monte Carlo simulations of GFP loss through a circular pore at the tip of the cell. **A**: Model geometry for a circular pore. **B**: Comparison of GFP intensity loss vs time with w_{pore} = 200 nm for different values of GFP diffusion constant D_{peri} as shown. **C**: Comparison of GFP intensity loss vs time with D_{peri} = 1 μm^2/s and different values of w_{pore} as shown.

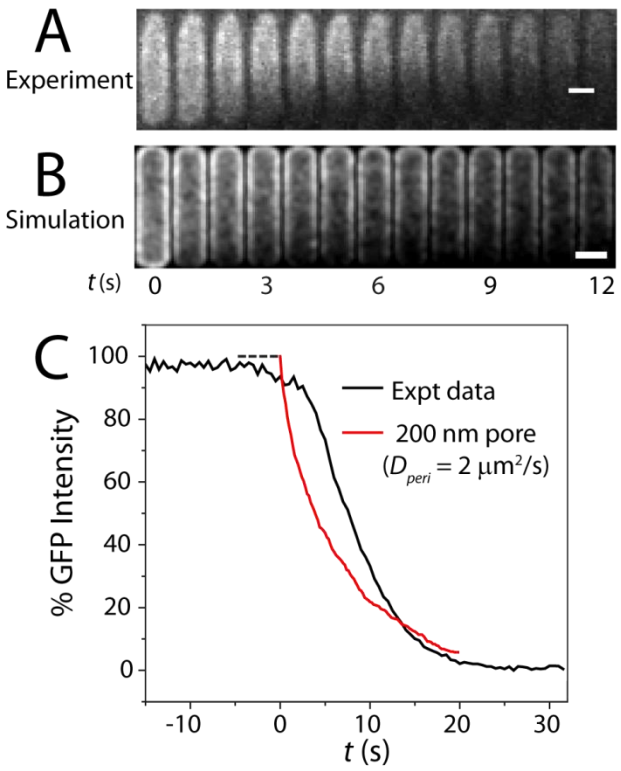

Figure S10. Two dimensional images of GFP loss from a non-septating cell. **A:** experimental example. **B:** Monte Carlo simulation using circular pore of 200 nm diameter and a diffusion constant D_{peri} = 2 µm^2/s. **C**: Comparison of GFP loss vs time for real cell and for the same model.

Comparison study of LL-37

Figure S11 illustrates the difference in the permeabilization behavior of LL-37 and Cecropin A in single septating cells. LL-37 permeabilizes both the OM and CM near the septum, at x_{rel} values of 0.52 and 0.58, respectively. Cecropin A permeabilizes the OM near the septum (x_{rel} = 0.56), but permeabilizes CM near an endcap (x_{rel} = 0.18). A summary of the timing of events related to OM and CM permeabilization, GFP loss and Sytox Green staining is presented in Table S1.

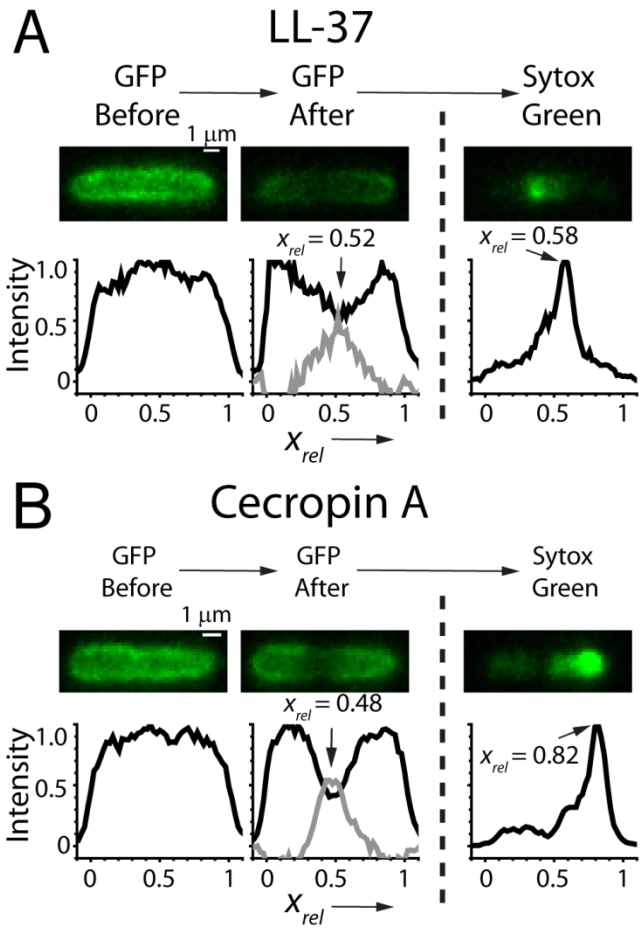

Figure S11: Axial intensity profiles of a single septating cell exposed to (**A**) LL-37 (4 μM) and (**B**) Cecropin A (2 μM). LL-37 permeabilizes both OM and CM near the septum. Cecropin A permeabilizes OM near septum and CM near an endcap. For (**A**) and (**B**), the two images and axial linescans at left were obtained just before and just after OM permeabilization to GFP. Subtraction of the two linescans makes the grey difference plot, from which we determine x_{rel} for the OM permeabilization event. The image and linescan at right shows the initial localized Sytox Green signal. We determine x_{rel} for CM permeabilization from the peak position of the axial linescan. See also Fig. S2.

Table S1. Summary of mean timing data for OM and CM permeabilization of *E. coli* by LL-37.

	Nominal Bulk Cecropin A Concentration	
	4 μM	**8 μM**
N_{tot} **(All cells)**	**9**	**19**
$\langle t_{OM} \rangle$	680 ± 540	220 ± 170
$\langle t_{CM} \rangle$	990 ± 330	350 ± 120
$\langle t_{CM} - t_{OM} \rangle$	320 ± 280	130 ± 150
$\langle \Delta t_{GFP} \rangle$	136 ± 89	60 ± 64
$\langle \Delta t_{Sytox} \rangle$	211 ± 93	89 ± 25
N_{sept} **(septating)**	**6**	**8**
$\langle t_{OM} \rangle$	262 ± 78	85 ± 43
$\langle t_{CM} \rangle$	916 ± 91	340 ± 120
$\langle t_{CM} - t_{OM} \rangle$	654 ± 78	250 ± 140
$\langle \Delta t_{GFP} \rangle$	130 ± 34	91 ± 54
$\langle \Delta t_{Sytox} \rangle$	220 ± 120	102 ± 25 (N = 8)
$N_{non\text{-}sept}$ **(non-septating)**	**3**	**11**
$\langle t_{OM} \rangle$	880 ± 560	310 ± 160
$\langle t_{CM} \rangle$	1030 ± 410	360 ± 130
$\langle t_{CM} - t_{OM} \rangle$	150 ± 160	50 ± 97
$\langle \Delta t_{GFP} \rangle$	140 ± 110	36 ± 63
$\langle \Delta t_{Sytox} \rangle$	205 ± 91 (N = 5)	76 ± 18

[a] All times in seconds. The ± values are one standard deviation of single measurements. *N* values give the number of cells in calculation of each mean.

References for Supporting Information

1. Bakshi, S., Bratton, B. P., and Weisshaar, J. C. (2011) Subdiffraction-limit study of Kaede diffusion and spatial distribution in live Escherichia coli, *Biophys J 101*, 2535-2544.

2. Matias, V. R., Al-Amoudi, A., Dubochet, J., and Beveridge, T. J. (2003) Cryo-transmission electron microscopy of frozen-hydrated sections of Escherichia coli and Pseudomonas aeruginosa, *J Bacteriol 185*, 6112-6118.

CHAPTER THREE

Live-cell imaging of the antimicrobial effects of synthetic, vesicle-permeabilizing peptides on *E. coli*

(To be submitted for publication)

ABBREVIATIONS

AMPs: Antimicrobial peptides, LUVs: Large Unilamellar Vesicles, CM: Cytoplasmic Membrane, OM: Outer Membrane, MRSA: Methicillin-Resistant *Staphylococcus auereus*, CDC: Centers for Disease Control and Prevention, TAT: Twin-Arginine Translocation pathway, MIC: Minimum Inhibitory Concentration, POPC: 1-Palmitoyl-2-oleoyl-sn-glycero-3-phosphocholine, POPG: 1-Palmitoyl-2-oleoyl-sn-glycero-3-phosphoglycerol, DPA: Dipicolinic acid, ANTS: 8-Aminonaphthalene-1,3,6-Trisulfonic acid, DPX: p-xylene-bis-pyridinium bromide, MLV: Multi-lamellar Vesicle, EZRDM: EZ-Rich Defined Medium, DMSO: Dimethyl sulfoxide, EMCCD: Electron Multiplying Charge Coupled Device.

ABSTRACT

In the previous chapter, we have shown that time-lapse microscopy can be used to study the action of natural antimicrobial peptides (Cecropin A and LL-37) on single *E. coli* cells at high spatiotemporal resolution. Here, we apply the same assays to investigate the effects of two synthetic antimicrobial peptides (AMPs), *ARVA and *VAYR*. Both peptides were previously discovered by our collaborators (Prof. Bill Wimley's group, Tulane University, New Orleans) in a stringent, high throughput *in-vitro* screen. Wimley and co-workers have demonstrated that *ARVA and *VAYR* permeabilize large unilamellar vesicles (LUVs) composed of anionic and zwitterionic phosololipids, similar to the bacterial cytoplasmic membrane (CM), within 30 min.

In our live-cell imaging assay, both peptides first permeabilize the CM and within 5 min. GFP that was previously restricted to the periplasm now gets redistributed over the entire cell volume. SYTOX signal also begins to rise at this time. For *ARVA, the early stages of DNA staining with SYTOX appear distributed along the length of the nucleoids, indicating global permeabilizaton of the CM to SYTOX. Less than 1 min after CM permeabilization, *ARVA causes fast loss of periplasmic GFP and rapid increase in SYTOX fluorescence, which saturates within 3-4 min. For *VAYR*, the early stages of DNA staining by SYTOX show bright puncta, indicating that CM disruption is localized to a small area of the perimeter. SYTOX staining and GFP loss are slow; requiring ~20-30 min for completion. The slow kinetics points to partial healing of the CM or limited permeation of the OM. Our studies provide a detailed comparison of the steps involved in the antimicrobial action of these peptides.

INTRODUCTION

Antibiotic resistance poses serious health concerns worldwide. Drug resistant bacteria (such as Methicillin-Resistant *Staphylococcus Aureus* or MRSA) cause more than 2 million infections and ~23,000 deaths in the United States each year[1]. Such 'superbugs' are able to survive long, continued treatments with the most potent antibiotic treatments. Antimicrobial peptides (AMPs), which are found in various eukaryotic organisms, are being studied as templates for the design of new, potent antibiotics to counter the spread of drug resistant bacteria. Natural AMPs are important components of the innate immune systems in humans (LL-37, Defensins), animals (Magainin, Protegrin), plants (Thionins) and insects (Cecropin A, Melittin). These peptides are known to counter microbial infections by direct microbial killing and by signaling the host immune response[2,3].

To better understand the mechanism of action of AMPs and to improve their potency and in-vivo applicability, research efforts have focused on the design and functional characterization of new, synthetic mimics of AMPs. These synthetic AMPs share compositional features of natural AMPs such as small size (10-50 residues), cationicity, a balance of hydrophobic and polar residues; and the adoption of ordered secondary structures (α-helices, β-sheets)[4].

In recent years, high throughput screens have been developed to test large libraries of synthetic AMPs for membrane permeabilizing activity on lipid vesicles. Some reports have suggested that membrane-permeabilizing activity on lipid vesicles does not necessarily correlate with antimicrobial potency against bacterial cells[5]. This could be attributed to the differences in lipid composition and organization in vesicles and cells. Vesicles are typically made by mixing purified lipids in varying ratios, freezing the mixture, evaporating the solvent, and then resuspending the frozen lipid mixture in a buffer. Therefore, the membrane composition in vesicles

is quite simplified. On the other hand, cell membranes consist of multiple types of lipids with substantial heterogeneity in the nature of head groups, chain lengths, degrees of unsaturation, etc. Furthermore, cell membranes also contain the cell wall material (lipopolysaccharide, peptidoglycan), membrane proteins and membrane surfaces of varying curvature[6]. In live cells, the membrane is being constantly synthesized, incorporated and modified. Therefore, a direct comparison of the action of membrane-active peptides such as AMPs on vesicle membranes and bacterial membranes is likely to yield different results. To better understand AMP activity, it is essential to complement *in vitro* LUV-based assays with mechanistic studies of antimicrobial action on bacterial cells.

We observe the sequence of events involved in the action of AMPs on single, live *E. coli* cells using time-lapse fluorescence microscopy. To observe AMP effects on membrane integrity in single cells, we use an *E. coli* strain containing GFP in the periplasm[7]. GFP is expressed in the cytoplasm tagged with a short peptide sequence that signals the twin-arginine translocase (TAT) pathway and exports it to the periplasm. As a secondary labeling strategy, we also observe the fluorescence dynamics of SYTOX Green or Orange – DNA stains that are non-fluorescent by themselves, but fluoresce brightly when bound to DNA[8]. Using this approach, we have previously shown that natural AMPs such as Cecropin A and LL-37 (both 37 AAs, +7 charge) cause localized permeabilization in the outer and cytoplasmic membranes of *E. coli* and, simultaneously, halt cell growth[9,10]. Additionally, using complementary approaches, our group has shown that some AMPs cause formation of reactive oxygen species on similar timescales as membrane permeabilization[11]. In our experience, each AMP produces a unique set of responses in single cells, which further provide clues to the mechanism of antimicrobial action. Our assays afford good spatiotemporal resolution for observing these events in single cells.

Here, we study the effects of synthetic peptides that were previously identified to permeabilize large unilamellar vesicles (LUVs) composed of anionic and zwitterionic phospholipids, similar to the bacterial cytoplasmic membrane. The peptides studied in this work (Table 3.1) are part of a ~16,000-member conformational peptide library designed to probe the compositional requirements for membrane permeabilizing activity[12,13]. Peptide sequences, lengths, net charge and minimum inhibitory concentrations (MICs) are given in Table 3.1. The sequences consist of a core segment of nine residues with four variable residues (charged (D, R), polar (N, T) or hydrophobic (V, A, G, Y)) and five fixed hydrophobic residues (W, three L's, Y). Terminal basic cassettes (RRG- and -GRR at the N- and C-termini, respectively; both represented as asterisks in the peptide names) were included to aid in peptide solubility. The C-terminal was amidated for all peptides. Members of the library contain 9, 12 or 15 amino acids depending on the presence of none, one or two terminal basic cassettes. The net charge ranges from +1 to +6. This library of peptides was screened for soluble members that permeabilize LUVs whose composition is similar to the bacterial cytoplasmic membrane[12]. Only ten unique peptide sequences with potent membrane permeabilizing activity were identified.

We selected two representative peptides – one 12-mer (*ARVA) and one 15-mer (*VAYR*) for the current study. We were interested in comparing the antimicrobial effects of two highly potent pore forming peptides identified in the same high throughput screen. We also studied two synthetic peptides (TP2 and LRL)[14] that were previously found to translocate across the membranes of LUVs composed of zwitterionic, eukaryotic phospholipds without permeabilizing them to small molecules and ions. We sought to determine whether these peptides could also translocate across *E. coli* membranes and inhibit cell growth.

RESULTS

The 9-hour MIC values of *ARVA and *VAYR* are 2 μM (Table 3.1 and Figure S3.1). We imaged single *E. coli* cells exposed to these peptides for at least 25 min. To ensure reproducibility of the results, we performed 2-3 replicate experiments and observed the dynamic responses of more than 600 cells in total. Images were acquired every 3 s with alternate excitation using a 488 or 561 nm laser and a white light source, resulting in an overall cycle time of 6 s. The total observation time of 30 min is composed of 300 imaging cycles. Fresh growth medium containing 2 μM *ARVA was flowed through the chamber starting at t = 0 min. This helps to maintain a constant bulk peptide concentration in the solution during the experiment. Details of the setup are provided in the Methods section and Supporting Information.

Action of 2 μM *ARVA. *ARVA causes dramatic membrane permeabilization and halting of cell growth in single *E. coli* cells. Here, we present a detailed analysis of the sequence of events in two representative cells, one each for the periplasmic GFP and SYTOX Orange assays. There is considerable heterogeneity in the kinetics and sequence of the antimicrobial symptoms. The sequence of events described for these cells were observed in a large majority of the observed cells. We discuss the number of cells that exhibit a particular phenotype, and quantify the mean timepoints at which these effects are first observed.

Cell images - effect on periplasmic GFP. *ARVA causes dramatic effects on the spatial distribution of periplasmic GFP. Figure 3.1A shows snapshots of GFP fluorescence within a representative cell shown at 30 s time intervals. The first two snapshots (4 and 4.5 min) show the cell with most of its GFP content in the periplasm, as evidenced by the thin shell of fluorescence. At 5 min, the spatial pattern of the fluorescence has changed dramatically. GFP is now

redistributed over the entire volume of the cell, i.e. the cytoplasm and periplasm, indicating that *ARVA has permeabilized the cytoplasmic membrane (CM). The 'whole-cell' distribution of GFP continues until 5.5 min. In the subsequent snapshots, at 6 min and 6.5 min, intracellular fluorescence is no longer observed. Evidently, the OM is also permeabilized between 5.5 and 6 min, allowing GFP to leave the cell. The extracellular volume is much larger than the volume of the cell and contains growth medium under constant flow. As GFP leaves the cell, it is diluted in the growth medium and flows out of the chamber.

We analyzed 70 single cells exposed to 2 μM *ARVA in two separate experiments. Similar to the representative cell discussed above, *ARVA causes near-complete loss of GFP in all cells within ~5 min. The sequence of events is also similar – redistribution of periplasmic GFP to the whole cell volume followed by GFP loss to the surrounding medium.

Transverse line profiles of periplasmic GFP fluorescence. Transverse line profiles of the GFP fluorescence signal were monitored to further demonstrate changes in the spatial distribution of GFP. Line profiles were constructed by integrating the fluorescence intensity along a swath drawn perpendicular to the long axis of the cell, and centered roughly at the mid-point of the cell. The initial fluorescence signal within the cell is mainly due to periplasmic GFP with minor contributions from cytoplasmic autofluorescence and GFP that is not exported to the periplasm. The transverse profile corresponding to the shell of fluorescence from periplasmic GFP features two peaks (Figure 3.1B, 4.5 min). Following permeabilization of the CM and redistribution of GFP within the entire cell volume, the two peaks merge into a single peak (Figure 3.1B, 5 min). Subsequently, after OM permeabilization and loss of GFP, the cell has negligible fluorescence and the transverse profile is a flat line close to zero intensity (not shown). Similar changes to the

transverse line profiles were observed in all the cells when GFP redistributes to the whole cell volume, and again when GFP leaves the cell.

GFP Intensity vs time plot. In addition to observing cell images, we monitor the total GFP fluorescence intensity within this cell over time. Figure 3.1C shows a plot of the background corrected intensity vs time for the same cell as in Figure 3.1A. By combining the quantitative information in this plot with the observed changes in the cell images, we determine the timepoints of the membrane permeabilization events. We define t_{CM} as the timepoint at which the CM is permeabilized to GFP. At t_{CM}, GFP redistributes over the entire cell volume. Similarly, t_{OM} is the time required to permeabilize the OM, which corresponds to loss of GFP to the surrounding medium. The delay between CM and OM permeabilization is $\Delta t_{GFP} = t_{CM} - t_{OM}$.

In the cell shown in Figure 3.1A, GFP remains in the periplasm for the initial 4.9 min after start of flow of *ARVA, and the total signal remains constant. At t_{CM} = 4.9 min, the GFP signal drops by ~17% over the next 12 s before the signal plateaus again. Loss in fluorescence signal corresponds in time with redistribution of GFP over the entire cell volume. Evidently, *ARVA has permeabilized the CM to GFP. The cause for signal loss upon migration of periplasmic GFP to the cytoplasm is currently unclear. Changes in the ionic strength or oxidation state of the cytoplasm upon AMP treatment might cause a reduction in the quantum yield of GFP fluorescence. We have observed similar reduction of GFP signal upon treatment of single cells with several short, cationic AMPs (CM-15, Indolicidin, cWFW, Melittin) and antimicrobial polymers that cause periplasmic GFP to move inwards into the cytoplasm (Weisshaar group, unpublished results). Following spatial redistribution, GFP intensity remains constant for the next 0.6 min (Δt_{GFP}). At t_{OM} = 5.5 min, this cell rapidly loses all fluorescence intensity over the next ~18 s. We attribute this to the permeabilization of the OM and loss of GFP from the cell.

We measured t_{CM}, t_{OM} and Δt_{GFP} values for 70 single cells exposed to 2 μM *ARVA in two separate experiments. The mean time required to permeabilize the CM in all the cells is 3.1 ± 1.7 min (t_{CM}, 70 cells). The mean time to permeabilize the OM is 3.8 ± 1.9 min (t_{OM}, 70 cells). *ARVA causes rapid, extensive disruption of both membranes to GFP in all cells within the field of view. The mean delay time between the CM and OM permeabilization in each cell is 0.6 ± 0.3 min (70 cells). All timing values and standard deviations are summarized in Table 3.2.

DNA staining by SYTOX Orange. The periplasmic GFP assay allows us to estimate the timescale at which *ARVA permeabilizes both cell membranes to GFP. We monitored membrane disruption to the DNA stain SYTOX Orange. Free SYTOX in solution has negligible fluorescence. Upon binding to DNA, the quantum yield of SYTOX increases ~500-fold and a bright signal is observed with 561 nm excitation. We observed DNA staining by SYTOX in single cells using our time-lapse microscopy setup. The image acquisition parameters were similar to the periplasmic GFP experiment.

At 2 μM, *ARVA permeabilized the CM of *E. coli* cells to SYTOX within ~5 min, similar to the timescale of CM and OM disruption to GFP. We quantified the dynamic staining of the nucleoid by SYTOX in over 100 single cells. Within cell-to-cell variation, the kinetics and spatial pattern of DNA staining are similar in all the cells. Here, we illustrate the progression of DNA staining by SYTOX in a single representative cell (Figure 3.1D). Growth medium containing dissolved *ARVA and SYTOX is flowed into the chamber at 0 min. Figure 3.1D shows cell snapshots between 2 and 7 min, at 1 min intervals. Negligible fluorescence signal is observed in the 2 min snapshot. At this stage, SYTOX molecules are present mainly in the surrounding growth medium. The OM is equipped with the porin channels (upper size limit 600-800 Da) and allows transport of ions and small molecules. SYTOX has a low molecular weight of 300-500 Da, and

may traverse across the OM into the periplasm. Since free SYTOX in the periplasm (and outside the cell) has negligible fluorescence, the cell does not exhibit a fluorescence signal. Therefore, the SYTOX Orange assay does not report OM permeabilization. The CM does not contain porins and, therefore, poses a size barrier to SYTOX.

SYTOX fluorescence is first observed in the 3 min snapshot. Evidently, *ARVA has permeabilized the cytoplasmic membrane to SYTOX. Shortly after entering the cytoplasm, SYTOX molecules bind to DNA and fluoresce. The cell exhibits two regions of fluorescence corresponding to the two DNA lobes stained with SYTOX. The fluorescence intensity increases in the subsequent snapshots (Figure 3.1D, 4-7 min), and is retained for the remainder of the image acquisition time period (30 min).

To quantify the dynamics of the SYTOX Orange fluorescence within this cell, we plot the total single cell fluorescence intensity vs time (Figure 3.1E). No signal is observed for the initial 2 min. At t_{SYTOX} = 2.1 min, the fluorescence intensity starts to rise. The cell image at 3 min shows the spatial pattern of SYTOX fluorescence soon after the staining begins. The signal reaches 90% of its max value at 4.9 min, resulting in a rise time for the SYTOX signal, $t_{SYTOX\ Rise}$ = 2.8 min. The signal plateaus at ~6 min, indicating saturation of the DNA binding sites. Subsequently, photobleaching of the dye results in decay of the total signal.

We measured t_{SYTOX} and $t_{SYTOX\ Rise}$ in 114 cells from two replicate experiments (both 2 μM *ARVA) and determined the average behavior. The mean lag time to permeabilize the CM to SYTOX was $\langle t_{SYTOX} \rangle = 2.4 \pm 1.0$ min. This $\langle t_{SYTOX} \rangle$ value agrees closely with the mean time to permeabilize the CM to GFP ($\langle t_{CM} \rangle = 3.1 \pm 1.7$ min), within variation across multiple experiments. We note that SYTOX signal and the first partial loss of periplasmic GFP signal, both, report the

same process, i.e. CM permeabilization. GFP also reports OM permeabilization when the signal subsequently drops to zero. The SYTOX signal saturated over 3.7 ± 1.7 min (<$t_{SYTOX\ Rise}$>, 114 cells).

*Effect of bulk *ARVA concentration on kinetics of CM and OM permeabilization.* We have previously observed that the bulk concentration of AMPs significantly affects the kinetics of membrane permeabilization[10]. In this work, we varied the bulk *ARVA concentration and monitored periplasmic GFP and SYTOX Orange fluorescence in single cells exposed to 0.5 μM (0.25 X MIC) and 1 μM (0.5 X MIC) *ARVA. We measured the timing values of membrane permeabilization events (t_{CM}, t_{OM}, Δt_{GFP}, t_{SYTOX} and $t_{SYTOX\ Rise}$) for more than 50 cells at both concentrations.

In the periplasmic GFP experiments, 0.5 μM *ARVA did not permeabilize membranes in any of 57 cells analyzed. Evidently, this concentration is insufficient to cause observable damage to cell membranes within 25 min. At 1 μM (half the 9-hour MIC value), *ARVA permeabilized the cytoplasmic membranes in ~50% of the cells in the field of view. The sequence of events is the same as described for the cell in Figure 3.1A. In 27 of 58 cells analyzed, *ARVA permeabilized the CM to periplasmic GFP within a mean lag time, t_{CM} = 15.4 ± 7.3 min. Subsequently, *ARVA permeabilized the OM within t_{OM} = 16.9 ± 7.4 min (27 cells), resulting in a mean delay time of Δt_{GFP} = 1.7 ± 0.8 min (27 cells). In 20 of the remaining 31 cells, periplasmic GFP was lost to the surrounding medium prior to being redistributed over the entire cell, *i.e.*, the OM was permeabilized to GFP before the CM. This presents as a secondary effect of *ARVA at 1 μM. Since this effect was not observed at 2 μM, we did not analyze this behavior in detail. However, we note that there is a high degree of variation in the single cell responses observed in our experiments at this concentration. Finally, the remaining 11 cells retained the periplasmic GFP

distribution throughout the observation time and continue to grow. It is possible that some or all of these cells would eventually lose their GFP content over longer timescales.

We studied the timescale of SYTOX staining as a function of bulk *ARVA concentration, similar to the periplasmic GFP study described in the preceding section (Table 3.2). At 0.5 μM, *ARVA does not induce SYTOX staining in any of 108 cells within the field of view. At 1 μM *ARVA, permeabilized 50 of 94 cells to SYTOX within 14.8 ± 4.3 min. The remaining 44 cells were not permeabilized to SYTOX. The $<t_{SYTOX\ Rise}>$ value at 1 μM *ARVA is 5.6 ± 2.0 min (42 cells). The $<t_{SYTOX}>$ values at 1 and 2 μM *ARVA agree closely with the mean t_{CM} values for periplasmic GFP at the same concentrations (Table 3.2). As explained in the previous section, the onset of SYTOX signal and partial loss of GFP signal reflect CM permeabilization.

Halting of cell growth. Simultaneous with CM permeabilization, *ARVA halts growth and causes shrinkage of cell length. As a proxy measure of cell growth, we monitored the tip-to-tip length (L_t) of phase contrast images of single cells. The single cells in our experiments are at various independent growth stages and, therefore, varying initial lengths. To facilitate comparison between the growth patterns of multiple cells, we calculate the relative cell length, L_{rel}, at each timepoint for each cell as follows:

$$L_{rel}(t) = L(t) / L(t=0)$$

At t = 0 min, all cells have an L_{rel} value of 1. L_{rel} values were measured for multiple cells chosen randomly from the periplasmic GFP and SYTOX Orange experiments at 0.5, 1 and 2 μM *ARVA. $<L_{rel}>$ vs t plots are shown in Figure 3.2 for (A) 9 cells at 0.5 μM, (B) 10 cells at 1 μM and (C) 13 cells at 2 μM. The solid black trace represents mean L_{rel} values; gray swath indicates standard deviations at each data point.

Cells exposed to 0.5 μM *ARVA continued to elongate throughout the observation time period (Figure 3.2A). At this concentration, the estimated doubling time (time over which cells double their length) is 74.5 ± 15.7 min (8 cells). This is slower than the doubling time for cells growing in fresh growth medium without any AMP treatment (~45 min[8]), indicating that 0.5 μM *ARVA slows down cell growth. As discussed in the preceding sections 0.5 μM *ARVA is insufficient to permeabilize membranes to GFP or SYTOX Orange.

At 1 μM, we observe halting of cell growth and shrinkage of length in a subset of the observed cells. A plot of $<L_{rel}>$ vs time for five representative cells (Figure 3.2B, solid line with light gray swath) shows that cell elongation occurs till ~10 min followed by gradual shrinkage over the next ~10 min. The final cell length is similar to the initial length at t = 0 min. Overall the cell length dropped by ~10% of the pre-shrinkage length. On a similar timescale, these same cells are permeabilized to periplasmic GFP and SYTOX Orange. Another subset of cells continues to elongate without exhibiting shrinkage. These cells are not permeabilized to GFP or SYTOX Orange over 25 min. The $<L_{rel}>$ vs time plot for five such cells (Figure 3.2B, solid line with dark gray swath) curves downward, indicating that growth rate slows down over 25 min. The mean doubling time for these five cells is 87.2 ± 7.8 min. This subset of cells grow slower than the cells exposed to 0.5 μM *ARVA.

At 2 μM, *ARVA halts growth and causes rapid shrinkage of all cells in the field of view. Based on the mean behavior of 13 representative cells, shrinkage occurs within ~2 min and is complete within the next ~3 min. Cell length decreases by ~10% (L_{rel} value drops from 1 to ~0.9) and remains fairly constant until 25 min.

Growth inhibition of a fraction of the total cells exposed to 1 μM *ARVA, rapid cell shrinkage at 2 μM *ARVA and the timescale of halting and shrinkage events are in close agreement with similar observations for membrane permeabilization to GFP and SYTOX. Taken together, these observations indicate the existence of a threshold bulk concentration between 0.5 and 1 μM. Below this threshold concentration (i.e. at 0.5 μM), no antimicrobial effects (membrane permeabilization or growth halting) were observed. While growth rate slows down, as indicated by the $<L_{rel}>$ vs time plot, cells continue to divide. Above the threshold (1 μM), we observed membrane permeabilization in a fraction of the total cells. On further increasing the bulk concentration to 2 μM, all cells were permeabilized within 5 min. The bulk AMP concentration is likely to limit the surface accumulation of AMP molecules on cell membranes, and slow down antimicrobial action.

Action of 2 μM *VAYR*. Here, we describe the sequence of events in the antimicrobial action of 2 μM *VAYR*. As in the case of *ARVA, we use the examples of single representative cells to describe membrane permeabilization to GFP and SYTOX, mean timing measurements of permeabilization and effect on cell growth. The image acquisition parameters are identical to the experiments with *ARVA.

Cell images - effect on periplasmic GFP. Figure 3.3A shows images of GFP fluorescence within a representative non-septating cell. In this cell, the periplasmic GFP distribution is maintained until 4 min. At 5 min, the spatial distribution has changed – now GFP is uniformly distributed over the entire cell volume. Evidently, *VAYR* has formed GFP-sized disruptions in the CM, similar to the action of *ARVA. Subsequently, *VAYR* causes GFP to leave the cell *gradually* over the following 20-25 min. This is different from the action of *ARVA, which disrupts the OM to GFP within ~5 min of CM permeabilization and releases GFP within 6-12 sec.

Transverse line profiles of the fluorescence images agree with the observed changes in the spatial distribution of GFP within the cell (not shown).

GFP fluorescence. GFP Intensity vs time plot. A plot of the GFP fluorescence intensity vs time for the same cell is shown in Figure 3.3B. The fluorescence signal remains constant for the first 4-5 min after start of flow of growth medium containing *VAYR*. At t_{CM} = 4.9 min, the GFP fluorescence signal drops abruptly by ~14% within 12 seconds. Simultaneously, GFP is distributed over the entire cell volume. As in the case of *ARVA, *VAYR* has permeabilized the CM to GFP. Subsequently, the cell loses GFP over the next 15-20 min.

At 2 μM *VAYR*, the mean time to permeabilize the CM averaged over 79 cells was $\langle t_{CM} \rangle$ = 4.6 ± 1.8 min. This value is similar to the $\langle t_{CM} \rangle$ for 2 μM *ARVA (3.1 ± 1.7 min). However, the kinetics of OM permeabilization of the two peptides is quite different. After permeabilizing the CM, there is a short delay time of 1-5 min, similar to the Δt_{GFP} value for 2 μM *ARVA (0.6 ± 0.3 min). Subsequently, *VAYR* causes the GFP signal to decay gradually over the next 15-20 min. In contrast, *ARVA causes GFP to leave the cell volume rapidly within 6-12 sec. The nature of OM permeabilization to GFP seems markedly different for the two peptides.

DNA staining by SYTOX Orange. We also tested the membrane permeabilizing activity of *VAYR* to SYTOX Orange. Figure 3.3C shows fluorescence snapshots of DNA staining with SYTOX in a representative cell. The fluorescence signal from DNA-bound SYTOX is first observed in the 3 min snapshot. It increases gradually over the remainder of the observation time. From the cell images over the entire 30 min movie (not shown), we observed that the cellular fluorescence continued to rise without plateauing. This behavior is different from that observed in the case of *ARVA (Figure 3.1A), where the signal plateaued within 5 min.

To quantify this behavior, we plotted the total fluorescence intensity vs time (Figure 3.3E). SYTOX fluorescence first appears at t_{SYTOX} = 1.7 min. The signal increases rapidly until t = 5 min and the Intensity-time plot during this time period exhibits a steep positive slope. Subsequently, further increase in SYTOX signal occurs at a slower rate, *i.e.*, the plot shows a smaller positive slope. Even at 30 min, the signal continues to rise and the Intensity-time plot has not yet plateaued. The $t_{SYTOX\ Rise}$ value (13.9 ± 6.5 min) for *VAYR* is much longer than for *ARVA (2.7 min, Figure 3.1E). However, we note that the rise of SYTOX signal in the case of *VAYR* exhibits two phases – an initial fast step followed by a slow step. Therefore, a single timing measurement does not accurately describe the timescale of events. Instead, we characterize the 2-step rise of SYTOX signal by measuring the timepoint and % signal at the inflection point of the Intensity-time plot. In Figure S3.2, we show similar plots for ten unique cells exposed to 2 μM *VAYR*. All cells exhibit the 2-step rise in SYTOX signal. For these ten cells, SYTOX signal starts to rise within $\langle t_{SYTOX} \rangle$ = 1.63 ± 0.14 min. On average, the fast step continues for the next 5.87 ± 0.54 min. By this time, the cell signal reaches ~65% of the maximum signal observed in the experiment. Subsequently, the cell fluorescence rises slowly over the remainder of the experiment. In our experience working with various AMPs, this is the first instance of partial arrest of nucleoid staining by SYTOX. Interpretations of this observation on the sequence of membrane permeabilization events are presented in the Discussion section.

Transient vs persistent nature of CM permeabilization. Wimley and co-workers have previously described the transient and partial nature of membrane permeabilization caused by *ARVA and *VAYR* in phospholipid LUVs[12]. The LUVs were composed of a mixture of anionic and zwitterionic phospholipids, similar to the CM of *E. coli*. Briefly, a single dose of peptide treatment caused partial release of encapsulated dye from vesicles. A second dose resulted in a

second burst of dye release, indicating that the initial membrane disruptions healed over time. Here, we tested whether these peptides cause similar transient permeabilization of the CM of single *E. coli* cells to SYTOX Orange. We treated cells with growth medium containing 4 μM *VAYR* or *ARVA (no SYTOX Orange) for 25 min. We used two-fold higher concentration of both AMPs to ensure that membrane disruption and growth inhibition is complete in all cells in the field of view within 25 min. Subsequently, we rinsed out the peptide solution and started flowing growth medium containing 5 nM SYTOX Orange at 26 min. We continued to image the cells until t = 50 min.

Figure 3.4 shows plots of the mean SYTOX signal in 10 cells for each experiment. The solid black traces represent the mean SYTOX fluorescence values, and corresponding gray swaths indicate the deviations of the fluorescence signal about the mean. In both cases, fluorescence signal is observed almost immediately upon start of flow of growth medium containing SYTOX. In *ARVA-treated cells, the fluorescence signal rises rapidly and saturates much faster, within 2.3 ± 0.6 min (10 cells). This is similar to the $<t_{\text{SYTOX Rise}}>$ value obtained at 2 μM *ARVA (3.7 ± 1.7 min, 114 cells). The slightly faster rise time observed in this experiment could be attributed to the higher bulk concentration of AMP, which may cause more extensive membrane permeabilization. In cells treated with *VAYR*, SYTOX fluorescence saturates within 18.9 ± 3.9 min (10 cells). This is longer than the $<t_{\text{SYTOX Rise}}>$ value obtained at 2 μM *VAYR* (13.9 ± 6.5 min, 95 cells). For both peptides, the SYTOX signal vs time traces exhibit a smooth rise. Interestingly, the plot for cells treated with *VAYR* did not exhibit the two-step increase in signal, as was previously observed when both *VAYR* and SYTOX were flowed together into the chamber (Figure 3.3C and Figure S3.2). We describe implications of this observation in the Discussion section.

Localized vs global permeabilization of the cytoplasmic membrane. We have previously shown that Cecropin A and LL-37, both natural antimicrobial peptides, cause localized permeabilization of the OM and CM to periplasmic GFP and SYTOX Green, respectively[10]. Here, we analyzed the spatial pattern of DNA staining by SYTOX Orange to test whether *ARVA and *VAYR* permeabilize the CM locally, or cause spatially distributed, 'global' disruption. We tracked the onset of SYTOX staining in single cells exposed to 4 μM *ARVA, 4 μM *VAYR* and, for comparison, 2 μM Cecropin A. At these concentrations, all peptides permeabilized cells to SYTOX Orange within ~5 min. To follow the dynamics of SYTOX staining, we acquired images at a rate of 5 frames/s, which is 30-fold faster than the previous experiments. We observed cell images and constructed axial line profiles of the SYTOX fluorescence for single cells treated with all three peptides.

Axial line profiles of the SYTOX Orange intensity provide further evidence for spatial pattern of SYTOX staining (Figure 3.5). For cells treated with *ARVA and Cecropin A, we obtained axial profiles at 2 s intervals between the first and second cell images (gray traces) to track the early onset of SYTOX Orange fluorescence (Figure S3.3), and at 20 s intervals for the subsequent cell images (black traces). Since *VAYR* causes slower SYTOX staining (explained in the text previously), gray traces were obtained at 4 s intervals to better represent the rise of SYTOX fluorescence. Black traces were made at 20 s intervals, similar to *ARVA and Cecropin A.

Fluorescence images and axial line profiles for a single representative cell exposed to *ARVA are shown in Figure 3.5A. In this cell, SYTOX Orange staining is clearly observed first at 3.6 min. The cell exhibits two regions of mild fluorescence corresponding to the two DNA lobes. The fluorescence signal on both lobes increases simultaneously with time. At 5.1 min, both DNA

lobes are brightly stained with SYTOX Orange. As is evident from the plot of total fluorescence intensity in the cell vs time (Figure S3.3), the SYTOX signal has saturated by ~5 min.

In this cell, axial profiles during the onset of SYTOX staining (gray traces, 3.3-3.6 min) exhibit two broad peaks centered at x_{rel} = 0.28 and 0.63. The locations of the peaks correspond to sites on the two DNA lobes. Both peaks rise in intensity with time; this indicates that both DNA lobes are stained by SYTOX Orange simultaneously. The lack of any obvious asymmetry in the axial profiles and the simultaneous, monotonic rise of the intensities of both peaks suggest that SYTOX molecules enter the cytoplasm from multiple entry points distributed along the cytoplasmic membrane. These entry points are sites of membrane permeabilization caused by *ARVA. Even at much longer time scales (black traces 3.80-5.13 min), the axial profiles exhibit two peaks at much higher fluorescence intensities. Overall, the cell images and axial profiles indicate that *ARVA permeabilizes the cytoplasmic membrane to SYTOX Orange globally.

In the cell treated with *VAYR* (Figure 3.5B), SYTOX fluorescence is first observed as a faint spot near the cell center at 4.1 min. The staining is more evident in the 4.8 min snapshot, consisting of a bright spot near the cell center and additional fluorescence distributed along the cell length. Axial line profiles corresponding to the early stages of SYTOX staining (gray traces) were obtained at 4 s intervals between the first two cell images, i.e. between 4.1 min and 4.8 min. SYTOX staining initially appears in a fairly localized manner, as evidenced by the peak in the gray traces near x_{rel} = 0.5. The peak broadens progressively and black traces (between 4.8 min and 6.7 min, 20 s intervals) exhibit two peaks corresponding to both DNA lobes.

In the cell exposed to Cecropin A (Figure 3.5C), SYTOX staining begins as a bright spot near one end cap at 2.4 min. Evidently, a small patch on the cytoplasmic membrane has been

permeabilized to SYTOX molecules. As more SYTOX molecules enter the cytoplasm and bind to the DNA, the fluorescence spreads along the length of the cell until it saturates all DNA binding sites at ~4.1 min (again, evident from the intensity vs time trace in Figure S3.3, signal plateaus at ~4.2 min).

At the early stages of SYTOX staining induced by Cecropin A (gray traces, 2.1-2.4 min), the axial profiles exhibit a single broad peak centered at x_{rel} = 0.19. This corresponds to SYTOX staining within one DNA lobe. All gray traces (covering 20 s in total) exhibit one peak, indicating that progressive staining of the DNA occurs on the same DNA lobe. We attribute this to localized permeabilization of the cytoplasmic membrane caused by Cecropin A. At 2.8 min (first black trace), the peak observed in the gray traces has broadened considerably, indicating that SYTOX staining has now progressed axially. This profile also features a slight shoulder at x_{rel} ~ 0.6, which marks the initial staining of the second DNA lobe. This shoulder grows into a second peak, as observed in the subsequent black traces (2.80-4.13 min).

The SYTOX Orange assay is blind to OM permeabilization, since the free dye does not fluoresce while in the periplasm. Therefore, it does not inform us about the spatial location of outer membrane permeabilization.

Action of membrane translocating peptides (LRL and TP2). LRL and TP2 belong to a family of membrane-translocating peptides that were selected in a high throughput screen for their ability to spontaneously translocate across membranes of artificial multilamellar vesicles (MLVs)[14]. These vesicles were composed of mixtures of zwitterionic phospholipids and carried a net neutral charge. The peptides also transported fluorescent dyes TAMRA and Alexa Fluor 546 across the membranes of Chinese Hamster Ovary (CHO) cells. At 1-2 μM, these peptides exhibited

translocation (across MLVs) or cargo transport (across eukaryotic cell membranes) within 15-30 mins.

MIC assay. The activity of these peptides against bacterial cells was not tested previously. We tested the growth inhibitory effects of LRL and TP2 on *E. coli* using the MIC assay. The assay for LRL and TP2 was carried out based on a protocol that was explained previously[10]. We mixed mid-log phase *E. coli* cell cultures with peptide solutions of varying concentrations (0.01-20 μM) in growth medium, and incubated at 30º C for 9 hours. The working concentration of LRL and TP2 used in the previous study with eukaryotic cells and MLVs (1-2 μM) falls within the concentration range tested in the MIC assay. Figure 3.6A shows a plot of Optical Density (OD at 600) nm vs peptide concentration. The black traces corresponding to LRL and TP2 indicate substantial cell growth (~ OD = 0.3), similar to the untreated sample ('No AMP' control). Evidently, LRL and TP2 did not inhibit cell growth, even at the highest concentration of 20 μM.

We also monitored the effects of these peptides on the periplasmic GFP distribution and cell length dynamics of single cells under the microscope. Here, we present results from the MIC assay on LRL and TP2; and microscopy experiments on LRL. Corresponding results from microscopy studies on TP2 peptide are presented in Supporting Information.

Effect of LRL on periplasmic GFP and cell length. We also checked if LRL and TP2 affect the spatial distribution of periplasmic GFP in *E. coli*, in a manner similar to *ARVA and *VAYR*. We flowed 10 μM of LRL (or TP2) into the microfluidic chamber containing single cells, and monitored the periplasmic GFP distribution for the next 25 min. Figures 3.6B-D show cell images and plots of GFP fluorescence intensity vs time and cell length vs time for one *E. coli* cell treated with 10 μM LRL. The fluorescence images (Figure 3.6B) show that GFP remains confined within

the periplasm over the 25 min observation time. Evidently, 10 μM LRL does not permeabilize the outer membrane or the cytoplasmic membrane to GFP. We also plotted the total GFP fluorescence intensity within the cell as a function of time (green trace, Figure 3.6D). The intensity trace is a flat line parallel to the time axis, indicating that the GFP content within the cell remains constant during the observation time. Over 25 min, there is some loss of the signal due to photobleaching.

The phase contrast images (Figure 3.6C) show that the cell elongates over time, without showing any halting of growth or shrinkage of cell length. This is supported by the plot of cell length vs time (black trace, Figure 3.6D), which shows that cell length increases exponentially. We did not find evidence for any adverse effects on the normal physiological state of the cells.

10 μM TP2 peptide also did not permeabilize the outer or cytoplasmic membranes to GFP; and did not cause halting of cell growth or shrinkage of cell length (Figure S3.4).

DISCUSSION

Summary of previous studies on *ARVA and *VAYR*. The membrane binding and permeabilizing effects of *VAYR* and *ARVA on LUVs composed of 9:1 POPC: POPG LUVs have been studied previously[12]. Peptide partitioning into the lipid membrane of the vesicles was monitored by measuring the enhancement of Tryptophan fluorescence upon addition of LUVs (Tryptophan emission maximum shifts from 352 nm in aqueous buffer to 332 nm in lipid). Both peptides bound to and saturated the lipid bilayer of the LUVs strongly within 5 minutes. Subsequently, membrane permeabilization was monitored the bulk fluorescence reported by various dyes: (a) Encapsulated Tb^{3+} and externally added DPA (chelator), (b) co-encapsulated ANTS (dye) and DPX (quencher), and (c) fluorescein-labeled Dextrans of either 3 or 40 kDa molecular weight. *ARVA caused a small increase in the bulk fluorescence signal, as observed in the Tb^{3+}-DPA assay. The signal rose immediately on mixing LUVs with the peptide, and saturated over 10-15 min. *VAYR* caused more than five times higher fluorescence, although the signal rose gradually over 25 min. Other members of this peptide library permeabilized LUVs within 10 min. The ANTS-DPX assay revealed that the mechanism of permeabilization was all-or-none, and not graded release.

All peptides released 5-50% of the encapsulated reporter molecules, indicating that the 'pore' state was a transient, short-lived event that caused partial release of encapsulated reporter molecules. A second addition of peptide caused a second burst of fluorescence signal, although no data supporting this observation was provided. This was not an equilibrium pore structure, as proposed for some other AMPs, which would release all contents within a few seconds. Instead, these peptides induce leakage over a much longer timescale of 5-30 min. These observations indicate that the permeabilized state of the LUV membrane heals over time.

Antimicrobial action of *ARVA. At the MIC value (2 μM), *ARVA permeabilizes *E. coli* cell membranes and halts growth within 5 min. In cells with periplasmic GFP, *ARVA first permeabilizes the CM, and within a few minutes, permeabilizes the OM, to GFP. The single cell fluorescence intensity decays in two steps. The first step coincides with CM permeabilization and redistribution of periplasmic GFP to the whole cell volume. We attribute this to a physiological effect of a change in the environment of GFP (periplasm to cytoplasm), although we don't have a quantitative explanation for reduction of GFP fluorescence yet. The second step is a rapid loss of GFP from cell, due to permeabilization of the OM. The CM and OM permeabilization events occur in close succession ($<\Delta t_{GFP}>$ = 0.6 min, Figure 3.1C and Table 3.1).

*ARVA also causes bright SYTOX staining – the signal rises rapidly and plateaus within a few minutes. The outer membrane of *E. coli* is permeable to small molecules of size 500-700 Da via the porin channels. We expect SYTOX Orange to equilibrate across intact outer membranes of cells soon after start of flow of growth medium containing peptide and SYTOX Orange. However, the cytoplasmic membrane prevents SYTOX molecules from entering the cytoplasm. If *ARVA sequentially permeabilized the CM and OM to SYTOX, similar to its effect on periplasmic GFP, we would expect a two-step increase in SYTOX signal. The first step would occur when the CM is permeabilized and SYTOX molecules already present in the periplasm would enter the cytoplasm and bind to DNA. This would result in a burst of SYTOX signal within the cell. Subsequently, on permeabilization of the OM, there would be a second stage of rise in SYTOX signal, presumably at a much faster rate. In the periplasmic GFP study, the delay between CM and OM permeabilization was 0.6 min. Assuming a similar delay in permeabilization to SYTOX, a change in slope of the SYTOX intensity vs time plot would be expected 0.6 min after the signal starts to rise.

As observed in the *I vs t* plot for *ARVA (Figure 3.1C), SYTOX signal increases smoothly in a single step. Once the cellular fluorescence begins to rise, there is no obvious break in the slope of the trace. However, the S-shaped early onset of SYTOX staining might be indicative of a slow rise of SYTOX signal (intact OM) followed soon after by a much faster rise (permeabilized OM). We note that this effect is rather subtle. Alternatively, it is possible that the CM and OM are permeabilized to SYTOX essentially simultaneously. Another explanation for the lack of a definite break in slope could be that while OM permeabilization increases rate of SYTOX entry into the periplasm, it may not significantly increase the rate at which SYTOX molecules access binding sites on the nucleoid.

Halting of cell growth and rapid cell shrinkage accompanies the CM permeabilization, possibly preceding it by a few minutes. Previously, we reported membrane permeabilization caused by natural AMPs Cecropin A and LL-37 using similar assays[9,10]. These peptides first permeabilized the OM, causing GFP to directly leave the cell without moving into the cytoplasm. Growth halting coincided with OM permeabilization. Subsequently, Cecropin A and LL-37 permeabilized the CM to GFP and SYTOX Green. Here, we observe cell shrinkage occurs at the same time as CM permeabilization. Evidently, damage to either membrane affects cell growth. The inhibitory effects of *ARVA and VAYR are persistent. We do not observe growth recovery after cell shrinkage in any cell.

Antimicrobial action of *VAYR*. *VAYR* first permeabilizes the CM to GFP. GFP signal decreases by ~10%, similar to the cell exposed to *ARVA (Figures 3.1A and 3.1C, see preceding discussion). In the second step, *VAYR* causes gradual loss of GFP signal from the cell, indicating slow leakage of GFP molecules to the surrounding medium. Complete loss of GFP occurs over ~15 min for *VAYR*. The same process occurred within 12-18 sec for *ARVA. The

slower decay of GFP signal in the case of *VAYR* indicates that the OM is permeabilized to a smaller degree. Alternatively, it is possible that CM or OM permeabilization occurs transiently and the membrane partially heals from the disruption.

SYTOX signal increases in two steps – an initial fast step in which ~65% of the total signal is attained within ~5 min, and a second slow step, which results in a further increase in signal by 35% over 10-20 min. As discussed for *ARVA, upon start of flow of growth medium containing *VAYR* and SYTOX, SYTOX molecules can traverse the intact OM but not the CM. Therefore, the early increase in SYTOX signal (Figure 3.3C) would correspond to SYTOX molecules already present in the periplasm. The rapid rise in signal indicates that the OM is also permeabilized to SYTOX, allowing large number of SYTOX molecules to bind to the DNA and fluoresce. A break from the fast increase in signal may occur when the CM has partially healed, reducing the rate of entry of SYTOX molecules into the cytoplasm. Alternatively, the same effect would occur if the OM recovers from the permeabilization event, resulting in slow entry of SYTOX molecules into the periplasm.

When we delayed flow of SYTOX until 25 min after treatment with 4 μM *VAYR*, we observed that SYTOX signal increased gradually over ~19 min (Figure 3.4). The kinetics of signal rise is similar to the second, slow step of the two-step rise previously observed for the cell in Figure 3.3. We did not observe the two-step rise of signal. This observation further substantiates the argument for membrane healing (either CM or OM) after the initial permeabilization event. In this experiment, recovery from permeabilization must have occurred before start of SYTOX flow, i.e. within 25 min.

Spatial pattern of CM permeabilization. The spatially distributed onset of SYTOX staining caused by *ARVA (line profiles in Figure 3.5A) points to the formation of multiple disruption sites along the perimeter of the CM. In contrast, *VAYR* causes mostly localized onset of SYTOX fluorescence, as evidenced by the peak near the cell center (x_{rel} ~0.5) in line profiles in Figure 3.4B (gray traces). This could be attribute to the permeabilization of a single, localized membrane region. Our assays do not have the resolution to distinguish whether this occurs via 'pores' or 'non-pore structures'. In our previous study of Cecropin A[10], we demonstrated that the timescale of GFP loss can be explained with membrane permeability equivalent to a 100 nm-diameter pore, or multiple smaller pores covering a similar area. A similar argument can be applied to the present observations as well.

A new model for sequential, transient permeabilization of *E. coli* membranes. Both *ARVA and *VAYR* cause periplasmic GFP to redistribute inwards into the cytoplasm. Evidently, these AMPs have translocated across the OM into the periplasm without causing GFP-sized disruptions on the OM. Direct observation of AMP translocation into the periplasm prior to CM permeabilization to GFP is a topic of future work. This would involve fluorescent labeling of AMP molecules with a red-emitting fluorescent dye (complementary to GFP emission); and monitoring fluorescence in both red and green channels in real time. After translocation into the periplasm, the AMPs permeabilize the CM to GFP. Translocation across the OM and subsequent permeabilization of the CM appears to be a common feature of the antimicrobial action of several short, cationic AMPs such as CM-15[11], Indolicidin, cWFW, Melittin (Weisshaar group, unpublished results). We note that this sequence of membrane permeabilization is different from the action of natural AMPs Cecropin A and LL-37, which permeabilize the OM first and cause periplasmic GFP to directly leave the cell[10]. There may be a threshold peptide length above which

AMPs cannot translocate across the OM and are required to cause OM disruption to access the periplasm.

For both *ARVA and *VAYR*, the lag times to permeabilize the CM to periplasmic GFP and SYTOX are 3-5 min. *ARVA permeabilizes the CM and OM in two fast steps, spaced <1 min apart. The extent of membrane disruption allows complete equilibration of both reporter molecules (GFP and SYTOX) across both membranes. The sequence of membrane permeabilization caused by *VAYR* involves rapid, sequential permeabilization of the CM and OM followed by partial recovery of the either the CM or OM, or both membranes. This is evidenced by the following two observations: (a) After the initial redistribution of GFP into the whole cell volume, subsequent loss of GFP slows down substantially before signal decay is complete. (b) The rise of SYTOX fluorescence slows down long before the total cell signal reaches its maximum value. These results are not consistent with an equilibrium pore structure, which would allow GFP and SYTOX to traverse across the CM within a few seconds. Instead, the slow kinetics of the GFP signal decay and SYTOX signal rise indicate partial recovery of the CM from the permeabilization. Similar 'membrane healing' has been invoked previously for LUV membranes with the aid of an amended 'sinking-raft' model of permeation[12].

In this model, initial binding and self-assembly of AMPs on the bilayer surface of an LUV membrane creates an imbalance of mass, charge and surface tension across the bilayer[12,15]. To relieve this imbalance, non-bilayer structures are formed simultaneous with trans-bilayer equilibration of peptides, lipids, entrapped contents and other solutes. Eventually, an equilibrium stage is reached when bilayer stress is completely dissipated. As a result, trans-bilayer movement of peptides or leakage of entrapped dyes stops.

Based on the sequence of events reported by periplasmic GFP and SYTOX in this study, we propose the following model of permeabilization of *E. coli* membranes:

(1) *Binding to OM*. *ARVA and *VAYR* bind to the lipopolysaccharide (LPS) layer, diffuse to the OM and accumulate on the outer leaflet of the OM. Diffusion through the LPS and surface accumulation explains the initial lag time before permeabilization observed in our study (Figure 3.1C and Table 3.2). Increasing the bulk AMP concentration enables faster accumulation of AMP molecules on the LPS and OM. This explains the observed dependence of $<t_{CM}>$, $<t_{OM}>$ and $<t_{SYTOX}>$ on the bulk concentration of *ARVA (Table 3.2). Similar lag times to permeabilization and dependence on bulk concentration have been previously observed for natural AMPs Cecropin A and LL-37[10].

(2) *Translocation across OM*. To relieve the bilayer stress created across the OM, *ARVA and *VAYR* molecules translocate into the periplasm. We do not observe loss of periplasmic GFP to the surrounding medium. This indicates that AMP translocation does not cause GFP-sized 'pores' to form on the OM. We believe translocation is a transient event without major perturbations to membrane integrity. Due to constant flow of the bulk solution, AMP molecules continue to accumulate on the OM, reinforce the bilayer stress, and translocate into the periplasm. This would result in accumulation of AMPs molecules in the periplasm.

(3) *Permeabilization of CM*. *ARVA and *VAYR* molecules in the periplasm can bind to several periplasmic targets, for e.g. the inner leaflet of the OM, peptidoglycan (PG) layer and the outer leaflet of the CM. All these processes would occur simultaneously. Our assay allows us to observe CM permeabilization, which would require AMPs to accumulate on the outer leaflet of the CM. This would cause bilayer stress and subsequent

permeabilization to reporter molecules GFP and SYTOX. The observed mean lag time required to permeabilize the CM, i.e. $<t_{CM}>$, would span steps 1-3 in this model.

(4) *Permeabilization of OM*. Bilayer stress on the OM can be relieved with or without the concomitant release of reporter molecules. We believe OM permeabilization to GFP involves the occurrence of GFP-sized disruption(s), in response to bilayer stress, as explained above.

(5) *Partial healing of CM or OM*. This step is invoked to account for the slow kinetics of GFP loss and SYTOX staining (step 2, Figure 3.3C). This may involve partial recovery of the planar bilayer arrangement of lipids. Alternatively, continuous influx of AMPs molecules may favor formation of AMP-lipid macromolecular aggregates that may result in partial blocking of membrane 'pores'. The detailed mechanisms of membrane healing need to be investigated.

This model needs to align with the observed spatial pattern of CM permeabilization to SYTOX. *ARVA permeabilizes the CM globally and completely. Cells do not exhibit recovery from the permeabilization event. Evidently, the presence of several membrane disruption sites distributed along the perimeter of the cytoplasm poses a significant challenge, and the cell is unable to recover from this stress. In contrast, *VAYR* permeabilizes the CM locally (e.g. near the cell center in Figure 3.4B). There is some evidence for a 'membrane healing' phenomenon, as discussed in the preceding section. The cell may be able to overcome (partially or completely) from a single, spatially confined site of membrane disruption. This 'healing' phenomenon may involve either partial shrinkage of a large 'pore' or disrupted membrane patch, or complete recovery of a fraction of the total, small-size 'pores'.

Further experimental validation of this model is required. For example, accurate estimate of the surface bound AMP concentration, possibly by monitoring fluorescence signal of a fluorophore-tagged AMP, would enable a more quantitative description of the initial steps proposed in this model. In preliminary work with a Rhodamine labeled Cecropin A, we have faced technical challenges involving high background signal from AMP molecules adhered to the coverslip and free molecules diffusing in solution. These result in poor signal-to-noise values during the initial binding event. Labeling AMPs with lipophilic membrane dyes that exhibit bright fluorescence in lipid environments might help to overcome this problem. These and other approaches to quantify the partition of AMPs from growth medium onto cell membranes will will be considered in future extensions of this work.

The underlying cause for differences between *ARVA and *VAYR* in the kinetics of membrane permeabilization events are currently under investigation. Both peptides were discovered in a stringent, high-throughput screen for potent membrane permeabilizing activity in LUVs. They bound to LUV membranes rapidly within a few minutes and permeabilized LUVs to small reporter molecules as well as 40 kDa Dextrans. While detailed mechanistic insights have been developed from such *in-vitro* studies, the biological relevance of the findings are unclear. Cell membranes are more complex in structure and composition than LUV membranes, which are composed of reconstituted, purified lipids. Also, in bacteria, the outer membrane is surrounded by the cell wall material (lipopolysaccharide in Gram-negative bacteria and peptidoglycan in Gram-positive bacteria)[6]. These are likely to influence the initial binding and interaction with AMPs. Additionally, it has been recently shown that the membrane permeabilizing activity on LUVs and antimicrobial activity on bacteria are weakly correlated[5]. Finally, the peptide-lipid ratios employed in LUV studies are widely different from those used in experiment antimicrobial assays with

bacterial cells[16]. These factors necessitate direct experimental studies of the antimicrobial effects of AMPs on live bacteria.

We also studied LRL and TP-2, both short, cationic peptides screened for membrane-translocating activity on multi-lamellar vesicles (MLVs) composed solely of zwitterionic phospholipids (as in eukaryotic membranes). We did not observe membrane permeabilization or halting of cell growth when these peptides were used at five times their working concentrations on MLVs. Our assay does not directly report peptide entry into the cell volume unless membrane integrity or growth rate are affected. It is possible that LRL and TP-2 translocate across the OM and CM while maintaining cellular homeostasis. This will have to be tested by imaging the interaction of fluorophore labeled peptides with *E. coli* cells.

CONCLUSION

Using live-cell imaging, we obtained a detailed view of the effects of two synthetic antimicrobial peptides, *ARVA and *VAYR*, on the CM, OM and growth rate of single *E. coli* cells. Both peptides exert rapid growth inhibitory effects involving permeabilization of the CM and OM to reporter molecules GFP and SYTOX Orange. *ARVA causes more rapid, persistent membrane defects. *VAYR* permeabilizes the CM transiently, and the membrane integrity recovers partially. It is intriguing that a single high throughput peptide screen selects for rare, membrane permeabilizing peptides that exhibit different action on live bacteria. Observing dynamic responses of single cells to antibiotic treatment enables detailed mechanistic understanding of antibiotic action.

METHODS

Peptides and stock solutions. All peptides (*ARVA, *VAYR*, TP2, LRL) were obtained as lyophilized powders from the Wimley Group. A second batch of *VAYR* was synthesized in the Peptide synthesis facility at the Biotechnology Center, University of Wisconsin-Madison. Details of peptide sequence design and solid phase peptide synthesis have been described earlier[12]. All peptide stock solutions were made in sterile, ultrapure (18.2 MΩ.cm) water containing 0.025% Acetic acid to aid in peptide solubility. A 5 mM solution (in DMSO) of SYTOX Orange was purchased from Molecular Probes (S11368). Cell cultures were grown in EZ Rich Defined Medium (EZRDM), which consists of MOPS buffer (M2130, Teknova), nucleic acids (M2103, Teknova), amino acids (M2104, Teknova), glucose (2 mg/mL), K_2HPO_4 (1.32 mM) and NaCl (76 mM). A 0.01% w/v solution of poly-L-lysine hydrobromide (MW>300,000 g-mol^{-1}, Sigma Aldrich, P1524) was made in sterile, ultrapure water.

Bacterial strains and growth conditions. The K-12 *E. coli* strain MG1655 is the parent strain used in all our experiments. To monitor periplasmic GFP, we expressed the TorA-GFP sequence from the plasmid pJW1 as described previously. TorA includes a short signal sequence (43 AAs) from trimethylamine N-oxide reductase that signals the twin-arginine translocation (TAT) pathway. The TorA sequence is cleaved upon transport to the periplasm. Cells were grown overnight to stationary phase at 30°C, diluted in fresh EZRDM and grown to exponential phase (optical density 0.3-0.5 at 600 nm) before injecting into the microfluidic flow chamber.

Minimum Inhibitory Concentration (MIC) assay. We have previously determined the MICs of LL-37 and Cecropin A to be 1 μM and 0.5 μM, respectively. Using a similar protocol, we determined the MICs of *VAYR* (2 μM), *ARVA (2 μM) and VVRG (8 μM) (Table 3.1 and

Figure S3.1). We also tested the potency of the membrane-translocating peptides TP2 and LRL to inhibit growth of *E. coli* cells using the MIC assay. We did not observe any visible growth inhibition up to a bulk concentration of 20 μM. This is discussed in detail in the Results section.

Peptide flow conditions. A detailed description of the microfluidic chamber is given in supporting information. Typically, ~500 μL of cell culture was injected in short pulses into the chamber. A field of view with at least 10 cells lying flat on the coverslip was selected prior to start of image acquisition and peptide flow. Excess cells suspended in bulk medium were rinsed out with fresh medium that did not contain any cells. To maintain a constant bulk peptide concentration throughout the observation time, the peptide solutions were continuously flowed through the chamber using a syringe pump (New Era Pump Systems, NE-300). At t = 0 min, peptide dissolved in growth medium was injected using the syringe pump at a flow rate of 0.2 ml/min. After 2 mins, the flow rate was reduced to 1 mL/hour (this enables the total chamber volume to be replenished every 5 mins).

Fluorescence and phase contrast microscopy. Details about the image acquisition setup have been described in detail earlier. We acquire cell images on a Nikon Eclipse Ti inverted microscope with an oil immersion objective (Nikon CFI Plan Apo Lambda DM; 100X magnification, 1.45 numerical aperture [NA]). Cell images were recorded on a back-illuminated EMCCD camera with 512 by 512 pixels of size 16 μm X 16 μm. Each pixel corresponds to 105 nm X 105 nm in real space, an overall magnification of 150X. Cell images with periplasmic GFP and DNA stained with SYTOX Orange were obtained by exciting cells at 488 nm (Ar^+ ion laser, Melles Griot) and 561 nm (CrystaLaser), respectively. Both lasers were used at an average laser intensity of 5-10 W/cm^2 at the sample. Appropriate bandpass filters (HQ510/20 for 488 nm

excitation and HQ600/50M for 561 nm excitation) were used to collect the fluorescence signal. To measure cell length vs time (as a proxy for cell growth), cells were illuminated with white light.

To obtain simultaneous fluorescence and white light images, cells were alternately illuminated with laser excitation and white light. Camera frames were acquired at a rate of 1 frame every 3 s with an exposure time of 50 ms/frame, resulting in a total cycle time of 6 s. Cells were imaged for 25 min after start of flow of antimicrobial peptides (250 imaging cycles).

Imaging onset of SYTOX Orange staining. To determine the spatial confinement of membrane permeabilization caused by *ARVA, we monitored the dynamics of DNA staining by SYTOX Orange at an image acquisition rate of 5 frames/s, which provides sufficient time resolution to continuously track the spatial pattern of SYTOX fluorescence within the cell (images were acquired at a rate of 2 frames/s in the Cecropin A study). The mean laser power at objective is 200 µW and the total imaging duration is 10 min. Peptide flow was started at 0 min at a rate of 0.2 mL/min for 5 min, the solution was static for the remaining 5 min of image acquisition. We used 4 µM *ARVA and 2 µM Cecropin A (both twice the MIC). At these concentrations, DNA staining by SYTOX Orange occurs within 5 min for most cells in the field of view.

Data Analysis. Fluorescence images of single *E. coli* cells were acquired using Andor Solis (version 4.23). Data analyses were performed using Fiji (ImageJ version 1.49 m), Microcal Origin 8.1 and MATLAB R2014a. The total single-cell fluorescence intensity and axial line profiles were computed as explained in previous works.

REFERENCES

(1) Antimicrobial resistance threats in the United States, 2013. Centers for Disease Control and Prevention.

(2) Jenssen, H., Hamill, P., and Hancock, R. E. W. (2006) Peptide antimicrobial agents. *Clin. Microbiol. Rev. 19*, 491–511.

(3) Hilchie, A. L., Wuerth, K., and Hancock, R. E. W. (2013) Immune modulation by multifaceted cationic host defense (antimicrobial) peptides. *Nat. Chem. Biol. 9*, 761–768.

(4) Brogden, K. A. (2005) Antimicrobial peptides: pore formers or metabolic inhibitors in bacteria? *Nat. Rev. Microbiol. 3*, 238–250.

(5) He, J., Krauson, A. J., and Wimley, W. C. (2014) Toward the de novo design of antimicrobial peptides: Lack of correlation between peptide permeabilization of lipid vesicles and antimicrobial, cytolytic, or cytotoxic activity in living cells: Toward the de novo design of antimicrobial peptides. *Biopolymers 102*, 1–6.

(6) Silhavy, T. J., Kahne, D., and Walker, S. (2010) The bacterial cell envelope. *Cold Spring Harb. Perspect. Biol. 2*.

(7) Sochacki, K. A., Shkel, I. A., Record, M. T., and Weisshaar, J. C. (2011) Protein diffusion in the periplasm of *E. coli* under osmotic stress. *Biophys. J. 100*, 22–31.

(8) Bakshi, S., Choi, H., Rangarajan, N., Barns, K. J., Bratton, B. P., and Weisshaar, J. C. (2014) Nonperturbative imaging of nucleoid morphology in live bacterial cells during an antimicrobial peptide attack. *Appl. Environ. Microbiol. 80*, 4977–4986.

(9) Sochacki, K. A., Barns, K. J., Bucki, R., and Weisshaar, J. C. (2011) Real-time attack on single *Escherichia coli* cells by the human antimicrobial peptide LL-37. *Proc. Natl. Acad. Sci. 108*, E77–E81.

(10) Rangarajan, N., Bakshi, S., and Weisshaar, J. C. (2013) Localized permeabilization of *E. coli* membranes by the antimicrobial peptide Cecropin A. *Biochemistry (Mosc.) 52*, 6584–6594.

(11) Choi, H., Yang, Z., and Weisshaar, J. C. (2015) Single-cell, real-time detection of oxidative stress induced in *Escherichia coli* by the antimicrobial peptide CM15. *Proc. Natl. Acad. Sci. 112*, E303–E310.

(12) Rathinakumar, R., and Wimley, W. C. (2008) Biomolecular engineering by combinatorial design and high-throughput screening: small, soluble peptides that permeabilize membranes. *J. Am. Chem. Soc. 130*, 9849–9858.

(13) Rathinakumar, R., Walkenhorst, W. F., and Wimley, W. C. (2009) Broad-spectrum antimicrobial peptides by rational combinatorial design and high-throughput screening: The importance of interfacial activity. *J. Am. Chem. Soc. 131*, 7609–7617.

(14) Marks, J. R., Placone, J., Hristova, K., and Wimley, W. C. (2011) Spontaneous membrane-translocating peptides by orthogonal high-throughput screening. *J. Am. Chem. Soc. 133*, 8995–9004.

(15) Wimley, W. C. Describing the mechanism of antimicrobial peptide action with the interfacial activity model. *ACS Chem. Biol.*

(16) Wimley, W. C. (2010) Describing the mechanism of antimicrobial peptide action with the interfacial activity model. *ACS Chem. Biol. 5*, 905–917.

Table 3.1: Sequences, lengths, charges and MIC values of the peptides studied in this work. The C-terminii of all peptides was amidated.

Peptide	Sequence	Length	Charge	MIC (μM)
***ARVA**	RRGWVLALYLRYGRR	15	+6	2
VAYR	RRGWALRLVLAY	12	+4	2
TP2	PLIYLRLLRGQWC	12	+2	--
LRL	LRLLRWC	7	+2	--
Cecropin A	KWKLFKKIEKVGQNIRDG--RIVQRIKDFLRNLVPRTES	37	+7	0.5

Table 3.2: Summary of mean timing data for membrane permeabilization to GFP and SYTOX Orange caused by *ARVA and *VAYR*.

Peptide	Bulk conc. (μM)	Total # of cells	$\langle t_{CM} \rangle$	$\langle t_{OM} \rangle$	$\langle \Delta t_{GFP} \rangle$
*ARVA	0.5	57	No effect on periplasmic GFP		
	1	58	15.4 ± 7.3 (27 cells)	16.9 ± 7.4 (27 cells)	1.7 ± 0.8 (27 cells)
	2	70	3.1 ± 1.7	3.8 ± 1.9 (67)	0.6 ± 0.3 (67)
VAYR	2	79	4.6 ± 1.8	--	--
			$\langle t_{SYTOX} \rangle$		$\langle t_{SYTOX\ Rise} \rangle$
*ARVA	0.5	108	No SYTOX staining		
	1	94	14.8 ± 4.3 (50 cells)		5.6 ± 2.0 (42 cells)
	2	114	2.4 ± 1.0		3.7 ± 1.7
VAYR	2	95	1.0 ± 0.5		13.9 ± 6.5

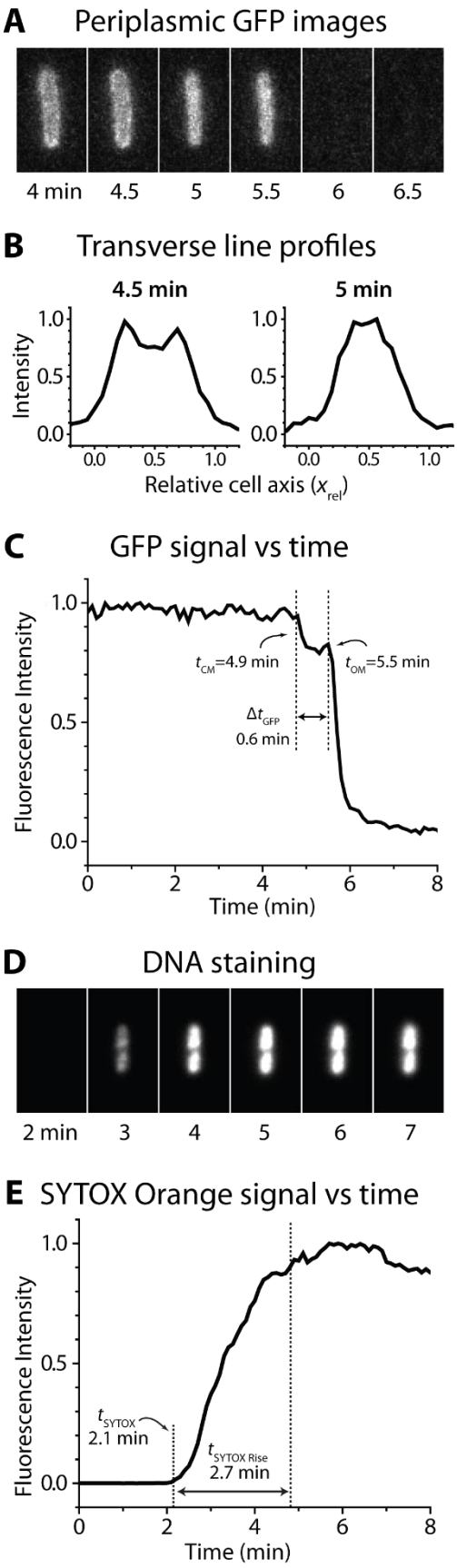

Figure 3.1: Cell images and quantitative data illustrating the changes in fluorescence due to periplasmic GFP and the DNA stain SYTOX Orange in a representative *E. coli* cell exposed to 2 µM *ARVA. The dynamics of the spatial distribution of periplasmic GFP are shown within this cell between 4 and 6.5 min at 30 s intervals. (B) Transverse line profiles of the fluorescence images of the cell at 4.5 and 5 min illustrate changes in the spatial distribution of GFP within the cell. (C) Plot of the single cell fluorescence versus time quantifies the dynamics of intracellular GFP. (D) DNA staining by SYTOX Orange caused by 2 µM *ARVA is shown in another representative cell. (F) The corresponding intensity vs time plot illustrates the timescale of the onset of SYTOX fluorescence.

Figure 3.2: Plots of mean relative cell length vs time for 0.5, 1 and 2 µM *ARVA. Gray swaths represent standard deviations about the mean.

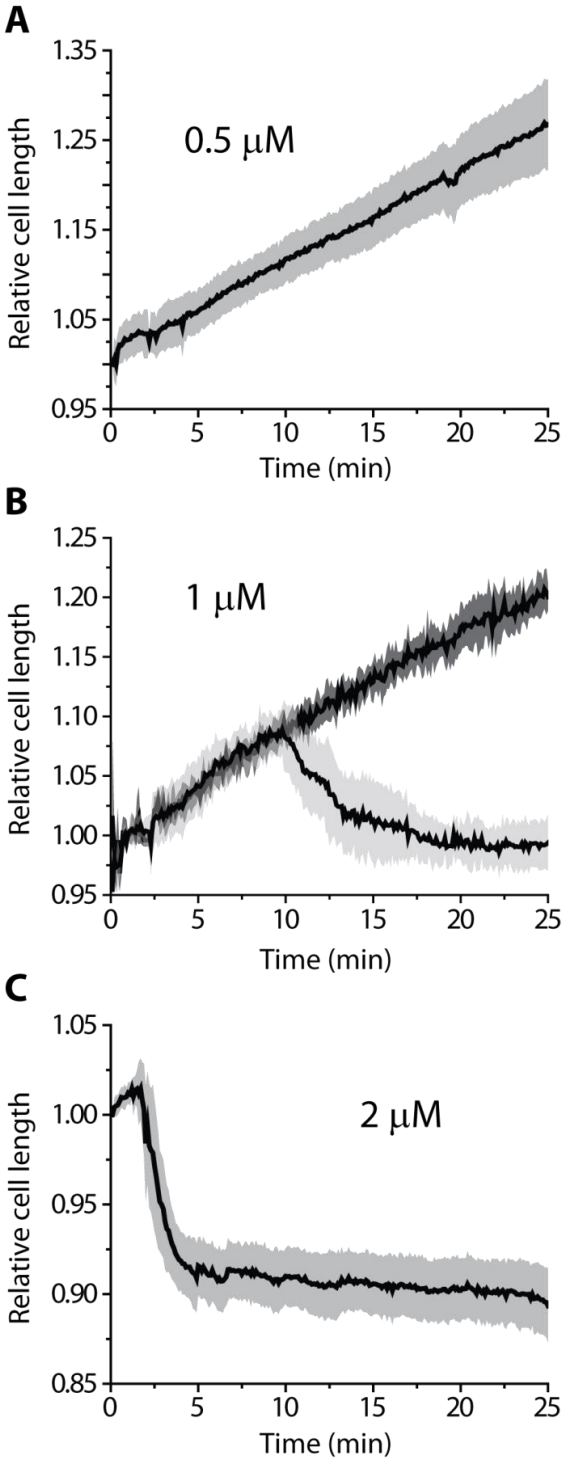

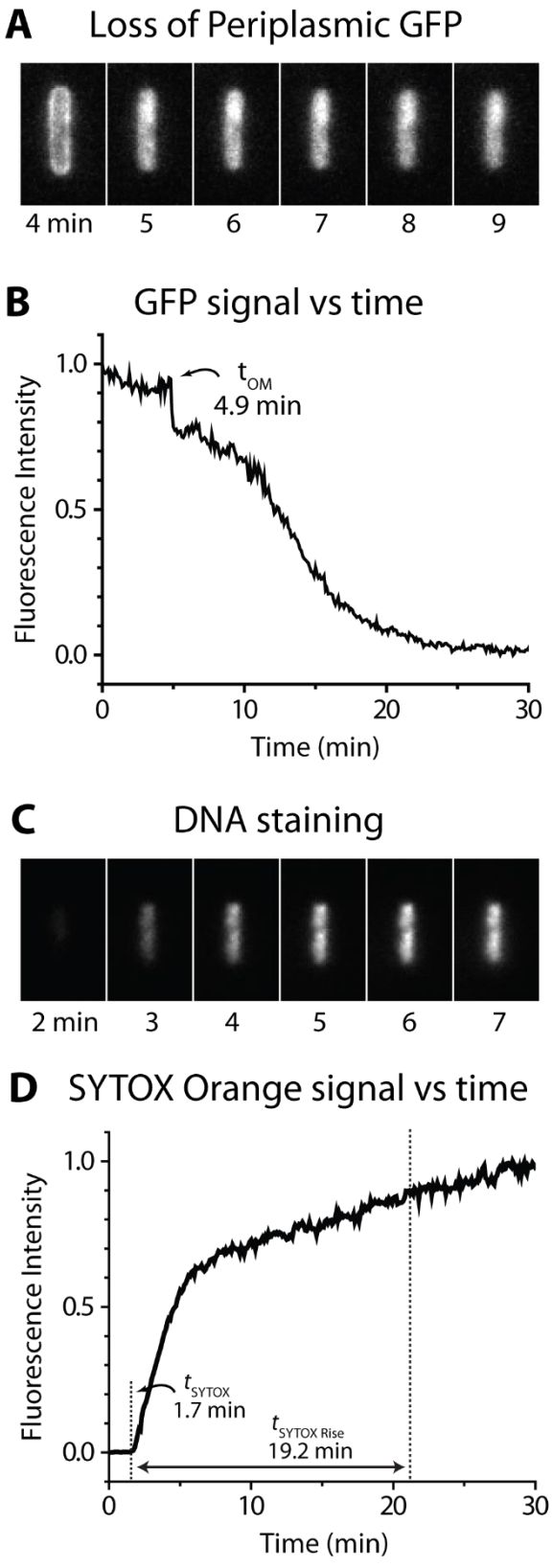

Figure 3.3: Cell images and quantitative data illustrating the changes in fluorescence due to periplasmic GFP and the DNA stain SYTOX Orange in a representative *E. coli* cell upon treatment with 2 µM *VAYR*. The dynamics of the spatial distribution of periplasmic GFP within this cell is shown between 4 and 9 min, at 1 min intervals (A). The total GFP fluorescence intensity in the cell is plotted as a function of time in (B). DNA staining by SYTOX Orange caused by 2 µM *VAYR* is shown in another representative cell (C). The corresponding intensity vs time plot (D) illustrates the timescale of DNA staining with SYTOX.

Figure 3.4: Plots of SYTOX Orange fluorescence vs time for cells exposed to 4 µM *ARVA and 4 µM *VAYR*. Peptide treatment was started at 0 min, until 25 min. Growth medium containing SYTOX Orange was flowed at 26 min. For both peptides, solid black lines represent mean fluorescence signal from 10 cells. Gray swaths represent standard deviations from the mean.

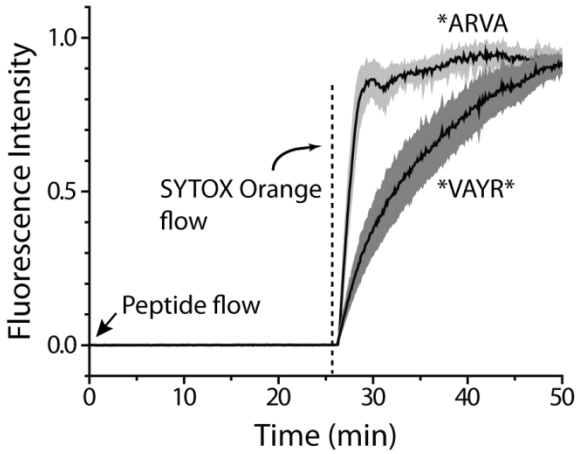

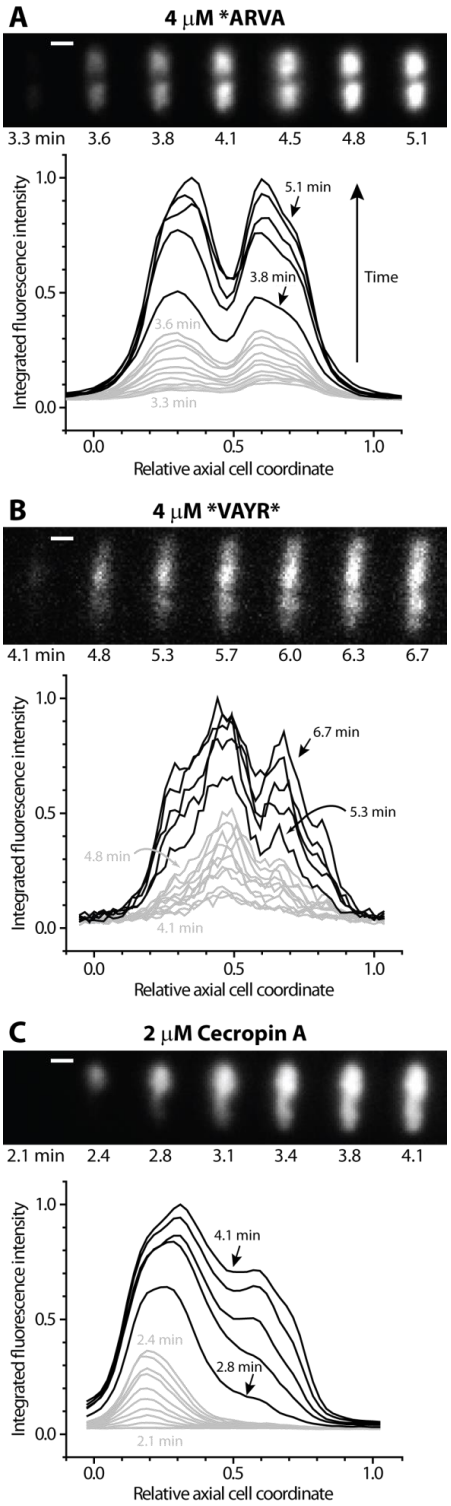

Figure 3.5: Comparison of spatial patterns of DNA staining by SYTOX Orange induced by (A) 4 µM *ARVA, (B) 4 µM *VAYR* and (C) 2 µM Cecropin A in representative cells. Cell images illustrate the overall dynamics of SYTOX staining. For *ARVA and Cecropin A, gray traces represent axial line profiles of SYTOX Orange fluorescence obtained at 2 s intervals. Black traces were obtained, subsequently, at 20 s. For *VAYR*, gray traces were obtained at 4 s intervals and black traces, again at 20 s intervals.

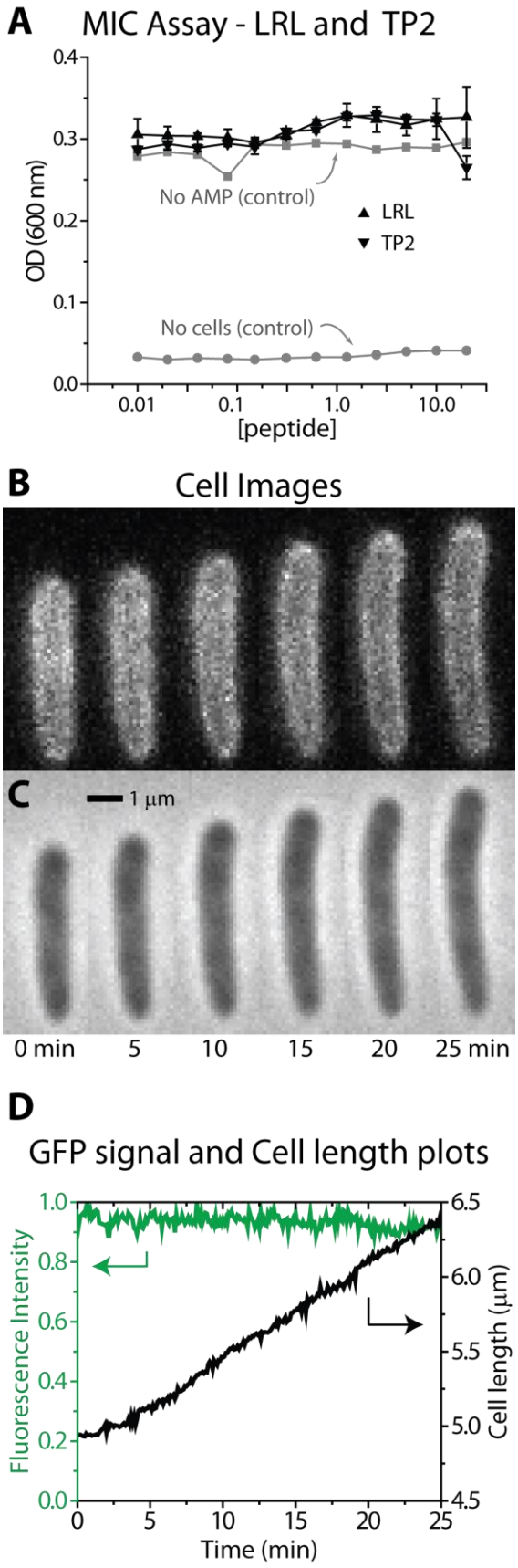

Figure 3.6: Effects of 10 μM LRL peptide on *E. coli* (A) Results from MIC assay of LRL and TP2 peptides on *E. coli*. (B) Fluorescence and (C) Phase contrast images of a single *E. coli* cell treated with 10 μM LRL peptide. (D) Plots of fluorescence intensity and cell length vs time for the same cell as in (B) and (C). GFP intensity stays fairly constant while cell length increases exponentially during the observation time

SUPPORTING INFORMATION

Figure S3.1: MIC assay plot for *ARVA and *VAYR*: A plot of the optical density (OD) at 600 nm vs peptide concentration for *E. coli* cell cultures mixed with the antimicrobial peptides *VAYR*, *ARVA and VVRG. The gray traces represent the cell culture lacking antimicrobial peptide (No AMP) and growth medium (No cells).

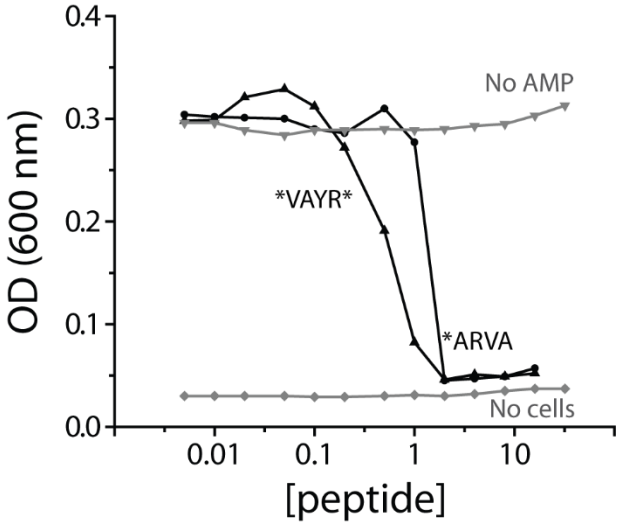

Figure S3.2: Plots of SYTOX Orange fluorescence vs time for ten representative cells exposed to 2 µM *VAYR*. All cells exhibit the two-step rise of signal composed of an initial fast step and a subsequent slower step.

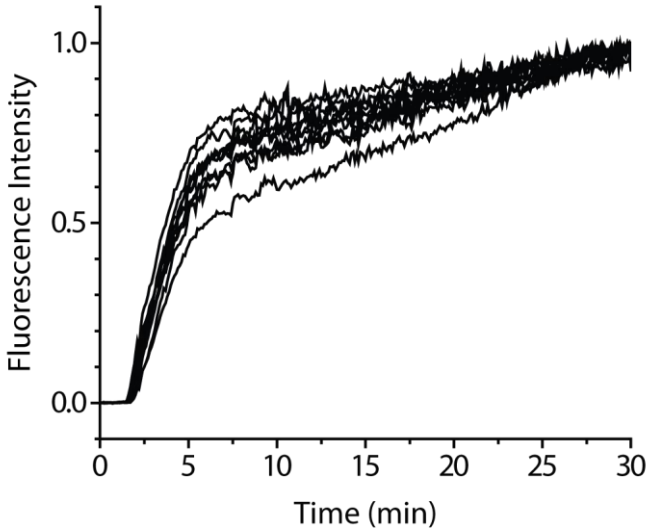

Figure S3.3: SYTOX Orange fluorescence intensity vs time plots for single cells exposed to 4 µM *ARVA, 4 µM *VAYR* and 2 µM Cecropin A. Gray traces were constructed at 2 s intervals (*ARVA and Cecropin A) or 4 s (*VAYR*) during the early onset of SYTOX staining, between the time points indicated by the dotted lines. Black traces were obtained at 20 s intervals for subsequent time points.

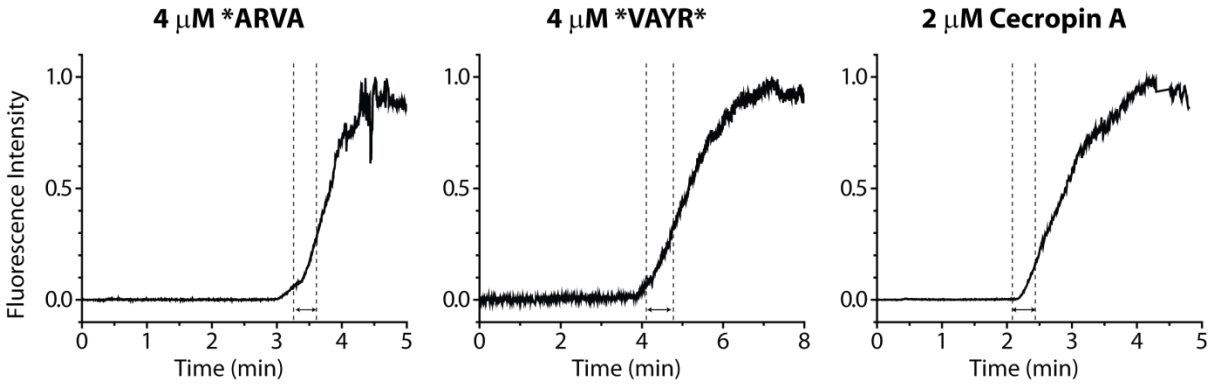

Action of 10 µM TP2 on periplasmic GFP and cell length

In the main text, we described the action of 10 µM LRL peptide on the periplasmic GFP distribution in *E. coli*. LRL had no adverse effects on cell growth and did not disturb the periplasmic GFP distribution up to 25 min after start of peptide flow. In an analogous experiment, we tested the effect of another peptide, TP2, known to translocate across the membranes of multilamellar vesicles and eukaryotic cells. We flowed 10 µM TP2 peptide into the microfluidic chamber and watched single cells with periplasmic GFP for 25 min after start of peptide flow.

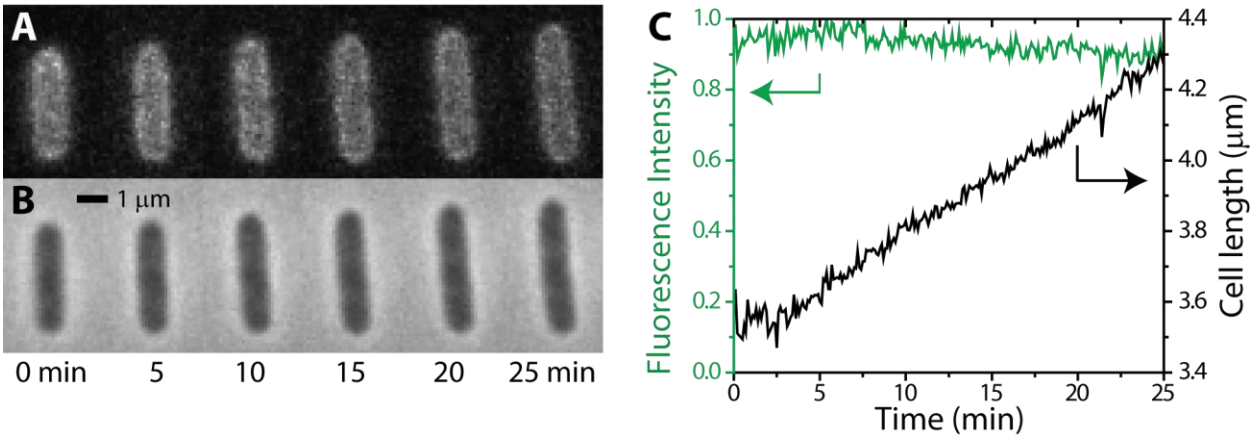

Figure S3.4: Effects of 10 µM LRL peptide on *E. coli* (A) Fluorescence and (B) Phase contrast images of one *E. coli* cell exposed to flow of 10 µM TP2 peptide. (C) Plots of GFP fluorescence intensity (green trace) and cell length (black trace) vs time for the same cell as in A and B.

Design, construction and use of the microfluidic chamber

The microfluidic chamber used in this work consisted of a polydimethylsiloxane (PDMS) mold adhered to a glass coverslip.

A master with the necessary micrometric features was designed and fabricated with the assistance of the research group of Prof. Doug Weibel (Department of Biochemistry, University of Wisconsin Madison). The master was rinsed with Ethanol and dried under a stream of Nitrogen. A piece of Aluminum foil of size ~10 inches X 10 inches was pressed around a flat bottom dish; and then removed from the dish. The clean master was placed inside the Al-foil dish and the foil was wrapped around the master to cover the base, but the chamber masks were left exposed.

Silicon Elastomer base was mixed with Silicon Elastomer curing agent (both Sylgard 184, Dow Corning) in a 1:10 ratio (base : curing agent) in a weighing boat, poured on top of the master to a height of ~2-3 mm, vaccum dessicated for 1 hour and cured at 110°C for 30 mins. The cured PDMS mold was peeled off the master, rinsed with Ethanol, dried under Nitrogen and trimmed with a razor. Inlet and exit ports of diameter 1 mm were punched on the junctions using tissue culture bores (Harris Unicore 1.00 Ted Pella Inc.). The chamber face of the PDMS mold was cleaned thrice with scotch tape, the opposite face was cleaned once.

Glass coverslips of size 40 mm X 20 mm (Fisher Scientific, catalog no. 12-548-5C) were rinsed with sterile, ultrapure water; sonicated with Acetone for 30 mins; rinsed again with water and dried under Nitrogen.

The Acetone-cleaned coverslips and cured PDMS mold were oxidized in an Oxygen plasma cleaner (Harrick Plasma). The oxidation process produces reactive silanol (-SiOH) groups at the glass and PDMS surfaces. A freshly oxidized coverslip and PDMS mold were brought in

contact with each other to form an irreversible covalent seal. This assembly provides a simple rectilinear observation volume with dimensions 11 mm by 6 mm by 50 μm (length by width by height). 10 μL of 0.01% w/v poly-L-lysine was injected into the chamber and allowed to bind to the coverslip surface at room temperature for at least 2 hours prior to imaging.

On the day of experiment, two stainless steel hypodermic needles (Component supply, part no. HTX-23R-30, previously cut into 1-inch bits) were rinsed with Ethanol, dried under Nitrogen, bent into an L-shape and inserted into inlet and exit ports on the PDMS mold. Polyethylene tubing (Warner Instruments, catalog no. 64-0752, PE-50) was connected to the free ends of the hypodermic needles. Unbound Poly-l-Lysine was rinsed out of the chamber with water. The chamber was attached to a metal plate with high vaccum grease (Dow Corning). For all our experiments, the plate was brought into contact with the microscope objective and warmed to 30°C by a TC-344B dual channel temperature controller and CC-28 heating cables attached to RH-2 heater blocks (all from Warner Instruments). Solutions were flowed through the chamber via a 1 mL NORM-JECT syringe equipped with an 18G-blunt tip needle. The exit tubing was connected to a waste reservoir.

The chamber elements that contribute to the total chamber volume include the inlet tubing, the hypodermic needle at the inlet port and the rectilinear observation volume. A conservative estimate of the total chamber volume is ~10 μL.

CHAPTER FOUR

Future Directions

INTRODUCTION

The time-lapse microscopy work described in this thesis provides detailed, quantitative insights into the action of antimicrobial peptides (AMPs) on live *E. coli* cells. At low micromolar concentrations, antimicrobial symptoms were observed within a few minutes of start of AMP treatment. Growth inhibition was simultaneous with membrane permeabilization. There was considerable cell-to-cell variation in the kinetics and spatial attributes of membrane permeabilization events. The Weisshaar group has extensively studied the antimicrobial action of several other AMPs in *E. coli*[1–4] and *B. subtilis*[5]. In our experience, every AMP-bacterium combination has displayed a unique sequence of events. Extensions of the current body of work will involve studying new AMPs and characterizing their mode of action. Development of novel biochemical assays to assess the effect on intracellular targets such as DNA, ribosomes, proteins, transmembrane potential and proton-motive force will further substantiate our understanding of antimicrobial events.

This concluding section discusses several areas in which the scope of this thesis can be extended. Section 1 describes ongoing efforts to adapt our microscopy-based assays to observe AMP effects in single cells from stationary phase cultures. To our knowledge, single cell analysis of the action of AMPs on stationary phase bacteria is an unexplored research area. This work carries significant medical relevance and will be of special interest to the research community. Section 2 focusses on investigating the molecular basis for localized permeabilization caused by Cecropin A and LL-37, as discussed in Chapters 2 and 3. For both projects, we describe proposed experiments and future directions. In Section 3, I have proposed several other extensions of this work that could serve as aims for future theses and research grants.

SECTION 1

Single-cell imaging of AMP effects on stationary phase *E. coli*

Bacterial growth has been quantitatively characterized under optimal laboratory conditions. The changes to cell density and volume after inoculation are graphically described as growth curves (measured as Optical Density at 600 nm vs time). There are four major phases of growth in bacteria:

(1) *Lag phase*: An initial period of negligible growth, when cells adapt to the changed growth conditions. This is observed when the culture is inoculated from a freezer stock or single colony. Depending on the nature of growth medium, temperature and aeration, this phase could last several hours.

(2) *Log phase*: This phase involves active cell metabolism, rapid growth and an exponential rise in the growth curve. Again, depending on growth conditions, the log phase can extend for several hours.

(3) *Stationary phase*: In this phase, nutrient depletion and accumulation of metabolic waste in the medium limits cell growth. Cell density is highest in stationary phase. The growth curve levels off and stays constant for several days. Although the total number of cells is constant, there is a dynamic cycling of cell division and death.

(4) *Death phase*: In this phase, the rate of cell death exceeds that of cell division. Cell density decreases and the growth curve has a negative slope.

The live-cell imaging studies described in Chapter 2, Chapter 3 and Appendix 1 were performed on single cells plated from bulk cultures in log phase. Similarly, most bulk assays of

antibiotic action have been performed on actively growing planktonic cultures in rich growth media. However, conditions that sustain exponentially growing bacteria are rarely found in the wild. In nature, bacteria spend most of their lifetimes in stationary phase[6]. Also, several chronic bacterial infections are likely to consist of non-growing or stationary phase bacteria, or biofilms. Therefore, it is important to develop antibiotics that are active against non-growing bacteria. The growth inhibitory or killing effects of several antibiotics depends on active cellular metabolism or division. It is well established that stationary phase bacteria resist antibiotic treatments. Also, antibiotics may adopt different modes of killing in actively dividing cells and non-growing cells, as demonstrated for Daptomycin, a lipopeptide antibiotic[7].

There are only a few reports of AMP studies on stationary phase cells. For example, the effects of Human neutrophil peptide Defensins on stationary phase cultures have been compared with activity on mid-logarithmic phase cultures. Stationary phase bacteria resisted cytoplasmic membrane permeabilization to small fluorophores (mol. Wt. 300 Da) and exhibited membrane blebs as observed in electron microscopy after long exposure to AMPs[8]. Similar blebbing in stationary phase *E. coli* was recently shown to be a major effect of Human α-Defensin 5 (oxidized form, with all three intact disulfide bonds)[9]. Other reports provide further evidence for increased resistance to AMPs in stationary phase bacteria[10–12].

Our single cell assays can be easily adapted to observe the effects of AMPs on live cells from stationary phase cultures at high spatiotemporal resolution. We have already developed a detailed understanding of the effects of several natural and synthetic AMPs on exponentially growing cells from mid-logarithmic cultures. By applying the same assays to stationary phase cells, we would be able to observe the growth phase dependence of the kinetics and sequence of

events of antimicrobial action. To perform time-lapse imaging on stationary phase cells, it is necessary to maintain individual cells in a state of negligible growth.

We achieved this by flowing growth medium depleted of nutrients by overnight bacterial growth. Briefly, we grew a separate batch of bacterial culture to stationary phase overnight. The culture was at 10,000g for 5 min and the supernatant was used as the flow solution in our experiment. We did not observe any visible growth in single stationary phase *E. coli* cells for 30 min under constant flow of spent medium. The cell length vs time plot shows no visible increase in length of 5 cells over 30 min (Figure 4.1). This is the timescale over which we observe AMP effects on cells from mid-logarithmic cultures. For the same batch of cells, subsequent rinsing of spent medium with fresh, rich growth medium results in recovery of exponential growth in all cells. This is illustrated by the rise in cell length vs time plot between 30 and 60 min in Figure 4.1. Evidently, lack of growth during the initial 30 min is due to lack of essential nutrients, and not due to any adverse killing effects of the spent medium.

In other experiments (data not shown), we have extended the duration of flow of spent medium for up to four hours, and still recovered cell growth by rinsing with rich medium. This could prove useful for our studies on stationary phase bacteria, as it has been shown that AMPs induce membrane permeabilization in stationary phase cultures on a much longer timescale than in mid-logarithmic cultures[8]. We note that stationary phase cultures have been previously used to maintain single stationary phase cells in a state of negligible growth[13]. However, in that work, the bulk culture was flowed as is into a microfluidic chamber, without removal of cells. The flowing medium was separated from the plated cells by a semi-permeable membrane, which prevent excess cells from interfering with plated cells. This method cannot be directly applied to

our setup as there is no separation between the flow medium and plated cells in our microfluidic chamber. This necessitates cell removal before flow of the spent medium.

In the future, we will perform time-lapse imaging on cells under flow of spent medium containing AMPs and SYTOX Orange. Similar to the work described in Chapters 2 and 3, we will monitor DNA staining by SYTOX as a proxy for cytoplasmic membrane (CM) permeabilization. We will also adapt the periplasmic GFP assay by first inducing GFP expression and export to the periplasm, and then allowing cell growth to process till stationary phase. The single cell GFP content will get diluted over several doubling cycles. We will optimize the protocol for inducing GFP expression to ensure sufficient GFP fluorescence signal in single stationary phase cells.

SECTION 2

Investigating a possible role of anionic phospholipids in localized membrane permeabilization caused by AMPs

In Chapter 2, we have provided a detailed discussion of localized permeabilization of the OM and CM caused by Cecropin A and LL-37. Membrane regions of high curvature, such as the septum and endcaps, are permeabilized more often than cylindrical membrane regions. In Chapter 3, we provide evidence that indicates *VAYR* permeabilizes the CM in a similar localized mode. The molecular cause for localization of membrane disruption is currently unknown. One hypothesis is that anionic phospholipids Phosphatidylglycerol (PG) and Cardiolipin (CL), which constitute more than 70% of the membrane material at the endcaps[14], may enhance AMP binding at these regions. A larger pool of active AMP molecules on the

bilayer surface near the septum and endcaps would, in turn, favor localized disruption of the membrane. Another hypothesis is that the membrane strain and lipid packing defects in highly curved membrane regions cause them to be more susceptible to permeabilization. It is possible both factors, the anionic lipid composition and strained geometry, cause these membrane regions to be favorable sites for AMP binding and permeabilization. In future work, we will test these hypotheses using methods described in Chapters 2 and 3.

We will observe onset of SYTOX staining and periplasmic GFP loss caused by AMPs in two *E. coli* strains lacking in PG and CL, as well as a double deletion mutant lacking both anionic phospholipids. As a control, we will include the parent 'wild-type' strain of these mutants. These strains have been generously gifted to us by the Weibel group. Quantitative comparisons of the polar localization of PG and CL in these strains have been performed and reported recently[14]. Septating cells were excluded from that study to facilitate analysis, so the septal localization of PG and CL has not been quantified. Based on methods described in Chapter 2, we will quantitatively determine the site of OM permeabilization to GFP and CM permeabilization to SYTOX. Using quantitative analysis and statistics, we will determine whether there is a significant difference in the average spatial pattern of OM and CM disruption between the four strains (three mutants and one wild-type strain). We will first test this hypothesis with Cecropin A, since its localized membrane permeabilization is well characterized (Chapter 2). We will also study LL-37 and *VAYR* and compare the observed trends of all three peptides.

If anionic lipid headgroups are involved in the localized membrane permeabilization caused by AMPs, we should observe that the same AMPs cause spatially distributed 'global' onset of membrane permeabilization in the absence of CL and PG. We also note such localized

disruption is, by no means, a universal feature of AMP action. In our research group, we have observed that several AMPs (CL-15, Indolicidin and Melittin) cause spatially distributed permeabilization of the CM and OM. We will include these peptides as controls in this proposed work.

SECTION 3

Other extensions of this work

Improving throughput. Although our time-lapse imaging assays enable detailed observations in single cells, our results are limited by low throughput. At the start of our experiments, all cells plated within our chamber (>1000) are simultaneously exposed to the AMP solution. Antimicrobial events occur within ten minutes. However, we observe only a small 50 µm X 50 µm field of view that contains, on an average 30-50 cells. Also, this experimental design does not allow us to switch to a different field of view to observe antimicrobial events in a second set of cells. The throughput of our method is at least two orders of magnitude lower than that of other single cell imaging works involving static snapshots of living/fixed/dead cells. This is an area that needs to be addressed in the future.

One route to improving throughput would be to design and construct a microfluidic device with multiplexed inlet channels and cell chambers. This is not possible in the current device, which consists of a single inlet channel and single cell chamber. The improved device would be allow us to plate cells separately in each chamber, and separately flow AMP solutions into each subset of cells. Flowing AMPs into one chamber should not interfere with regular growth of cells in other chambers. After acquiring images in the first chamber (over ~10 min),

the stage can be moved manually to bring the second chamber within the field of view. This way, several time-lapse movies can be acquired on the same microfluidic device.

Another way to improve throughput would be to use a lower magnification objective lens. Essentially, this would result in 'zooming out' of the focal plane and observing a larger field of view. For e.g. replacing a 100X objective lens with a 10X lens would result in a ten-fold increase in the area of the field of view and in the number of cells per experiment. It is important to note that loss of magnification will be accompanied by loss of spatial resolution and possibly, lower numerical aperture. This affects the ability of the objective to collect photons, and may limit the applicability of low magnification lenses under low signal conditions. It may be advisable to first perform experiments at high magnification to understand details of the spatial patterns in antimicrobial events. This could be substantiated by further experiments at lower magnification to obtain the broad dynamics of intracellular fluorophores at high throughput.

Studying AMP action within phagocytes. The work described in this thesis involves studying live bacterial cells in-vitro, on a glass coverslip. Inside host organisms, bacteria are exposed to a wide variety of immune cells, such as phagocytes and neutrophils. Both these cells engulf and ingest invading bacterial cells, and then release AMPs, enzymes and other co-factors that cause bacterial cell lysis. Developing time-lapse imaging assays to observe *E. coli* cell engulfment and ingestion by phagocytes would enable us to understand the early processes in immune response. Monitoring the lysis of the 'phagocytosed' bacteria within single phagocytes would provide a detailed view of the killing process. The experimental workflow would involve first plating single phagocytes on the glass coverslip. Phagocytes are 15-16 μm in diameter. Our microscope's field of view is sufficient to observe at least 2-3 phagocytes. A diluted bacterial culture can be flowed through the chamber. There will be a wait time before a bacterial cell

comes in the proximity of the phagocytes in our field of view. This could be adjusted by the OD of the bulk culture.

Sequences and timescales of bacterial killing events can be quantified using methods similar to those used in this work. It will also be interesting to compare these parameters for wild-type macrophages and mutant macrophages deficient in AMP expression. It is expected that AMP-deficient macrophages would cause slower or reduced extent of bacterial killing. Also, mutant macrophage strains deficient in one of several important phagocytosis factors such as lysozymes, peroxidases, lactoferrin, etc can be studied. This would enable us to quantify the relative contributions of these factors towards each individual step in phagocytosis – engulfment, ingestion and, eventually, cell lysis and degradation.

CONCLUSIONS

Single cell investigations of AMP action on live bacteria report on the detailed sequence of events in bacterial killing. Our imaging studies provide a direct view of individual bacterial cell during antimicrobial action at high spatiotemporal resolution. Using an ensemble of labeling approaches, it is possible to study the effects of AMPs on the cell envelope, DNA, ribosomes, electron transport chain as well as specific intracellular proteins. Based on our studies and works by other groups, we know that several essential processes are targeted by AMPs over similar timescales.

To observe antimicrobial symptoms on a convenient timescale, we used AMPs at 1X or 2X the bulk MICs. We note that the agreement of in-vitro concentrations (in bulk and on cell surfaces) with actual AMP levels within infected host organisms is not unclear. Concentration

dependence of AMP effects needs to be investigated in greater detail. Several growth inhibitory effects have been reported at sub-MIC levels of AMPs. Essential process such as transcription, translation and cell division may be targeted prior to membrane permeabilization. Studies monitoring gene expression in cells treated with AMPs at sub-MIC concentrations have revealed that a wide variety of cellular processes are affected during antimicrobial action. The time resolution of these studies do not afford a direct comparison with the timescales of antimicrobial attack observed in our experiments. Also, most of the transcription profiling work has been performed on bulk cultures. Therefore, the data reports on the gene expression changes averaged over the entire cell population. We expect a wide degree of cell-to-cell variation in transcriptional response. To enable a detailed view of the early stages of antimicrobial action at high resolution, it would be interesting to apply single-cell transcriptomics assays to AMP studies. Quantifying transcript-level changes in AMP-treated single cells would provide a further level of detail into the underlying cellular effects. Comparisons with the phenotypes observed in live-cell imaging assays would allow enable a comprehensive understanding of AMP action.

REFERENCES

(1) Sochacki, K. A., Barns, K. J., Bucki, R., and Weisshaar, J. C. (2011) Real-time attack on single Escherichia coli cells by the human antimicrobial peptide LL-37. *Proc. Natl. Acad. Sci. 108*, E77–E81.

(2) Rangarajan, N., Bakshi, S., and Weisshaar, J. C. (2013) Localized Permeabilization of E. coli Membranes by the Antimicrobial Peptide Cecropin A. *Biochemistry (Mosc.) 52*, 6584–6594.

(3) Bakshi, S., Choi, H., Rangarajan, N., Barns, K. J., Bratton, B. P., and Weisshaar, J. C. (2014) Nonperturbative Imaging of Nucleoid Morphology in Live Bacterial Cells during an Antimicrobial Peptide Attack. *Appl. Environ. Microbiol. 80*, 4977–4986.

(4) Choi, H., Yang, Z., and Weisshaar, J. C. (2015) Single-cell, real-time detection of oxidative stress induced in *Escherichia coli* by the antimicrobial peptide CM15. *Proc. Natl. Acad. Sci. 112*, E303–E310.

(5) Barns, K. J., and Weisshaar, J. C. (2013) Real-time attack of LL-37 on single Bacillus subtilis cells. *Biochim. Biophys. Acta BBA - Biomembr. 1828*, 1511–1520.

(6) Kolter, R., Siegele, D. A., and Tormo, A. (1993) The stationary phase of the bacterial life cycle. *Annu. Rev. Microbiol. 47*, 855–874.

(7) Mascio, C. T. M., Alder, J. D., and Silverman, J. A. (2007) Bactericidal Action of Daptomycin against Stationary-Phase and Nondividing Staphylococcus aureus Cells. *Antimicrob. Agents Chemother. 51*, 4255–4260.

(8) Lehrer, R. I., Barton, A., Daher, K. A., Harwig, S. S., Ganz, T., and Selsted, M. E. (1989) Interaction of human defensins with Escherichia coli. Mechanism of bactericidal activity. *J. Clin. Invest. 84*, 553–561.

(9) Chileveru, H. R., Lim, S. A., Chairatana, P., Wommack, A. J., Chiang, I.-L., and Nolan, E. M. (2015) Visualizing Attack of *Escherichia coli* by the Antimicrobial Peptide Human Defensin 5. *Biochemistry 54*, 1767–1777.

(10) McLeod, G. I., and Spector, M. P. (1996) Starvation- and Stationary-phase-induced resistance to the antimicrobial peptide polymyxin B in Salmonella typhimurium is RpoS (sigma(S)) independent and occurs through both phoP-dependent and -independent pathways. *J. Bacteriol. 178*, 3683–3688.

(11) Matsuo, M., Oogai, Y., Kato, F., Sugai, M., and Komatsuzawa, H. (2011) Growth-phase dependence of susceptibility to antimicrobial peptides in Staphylococcus aureus. *Microbiol. Read. Engl. 157*, 1786–1797.

(12) Kozlowska, J., Vermeer, L. S., Rogers, G. B., Rehnnuma, N., Amos, S.-B. T. A., Koller, G., McArthur, M., Bruce, K. D., and Mason, A. J. (2014) Combined Systems Approaches Reveal Highly Plastic Responses to Antimicrobial Peptide Challenge in Escherichia coli. *PLoS Pathog 10*, e1004104.

(13) Gefen, O., Fridman, O., Ronin, I., and Balaban, N. Q. (2014) Direct observation of single stationary-phase bacteria reveals a surprisingly long period of constant protein production activity. *Proc. Natl. Acad. Sci. 111*, 556–561.

(14) Oliver, P. M., Crooks, J. A., Leidl, M., Yoon, E. J., Saghatelian, A., and Weibel, D. B. (2014) Localization of Anionic Phospholipids in Escherichia coli Cells. *J. Bacteriol. 196*, 3386–3398.

FIGURE 4.1

Relative cell length vs time plots for five single cells sequentially exposed to spent medium and rich growth medium. Cells were exposed to spent medium from 0 min to 30 min; and fresh, rich growth medium from 30 to 60 min.

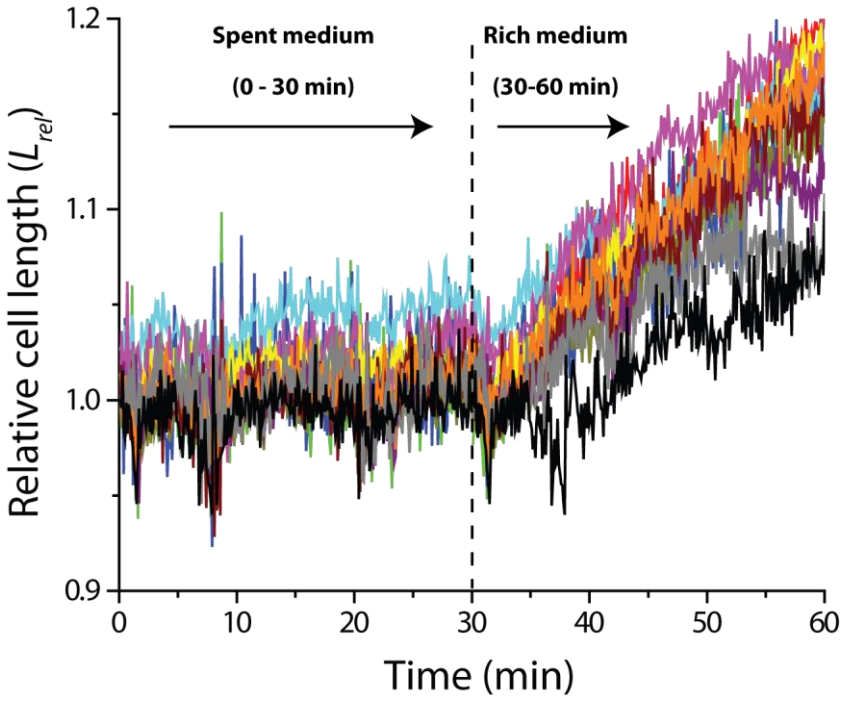

APPENDIX 1

Effects of Cecropin A and LL-37 on the segregation of DNA and ribosomes in *E. coli*

*(**Adapted from**: Bakshi, S., Choi, H., Rangarajan, N., Barns, K. J., Bratton, B. P., and Weisshaar, J. C. (2014) Nonperturbative Imaging of Nucleoid Morphology in Live Bacterial Cells during an Antimicrobial Peptide Attack. Appl. Environ. Microbiol. 80, 4977–4986.)*

Introduction

We have previously studied the applicability of two different classes of DNA-binding fluorescent stains for imaging live *E. coli* cells[1]. 'Dead-cell stains' SYTOX Orange and SYTOX Green were found to be more suitable than 'live-cell stains' DRAQ5 and SYTO 61, and also DAPI. SYTOX Orange was used to monitor DNA replication and segregation in dividing cells using time-lapse fluorescence microscopy. Cell growth, as measured by the tip-to-tip cell length of the phase contrast images, was not affected much due to the SYTOX staining. In contrast, the other dyes either caused perturbation of the DNA spatial distribution (DRAQ5, DAPI), halting of cell growth (DRAQ5), or provided a less detailed view of the nucleoid (SYTO 61). SYTOX Orange also stained the nucleoids of single *B. subtilis* cells to provide similarly bright, detailed fluorescent patterns.

In unperturbed cells, superresolution fluorescence imaging of RNA polymerase and 30S ribosomal subunits has previously revealed that chromosomal DNA and ribosomes exhibit strong spatial segregation[2]. Due to separation of nascent chromosomes, cells of medium length exhibit two nucleoid lobes. The ribosomes occupy three 'ribosome-rich regions' where the DNA density is low: two at the end caps and one at the cell center. A simple model of excluded volume and polymer entropy helps explain this segregation[3]. Here, we co-imaged the *E. coli* nucleoids (stained by SYTOX Orange) and ribosomes (labeled with an S2-YFP construct expressed from the chromosome) and tested for effects of antimicrobial peptides (AMPs) Cecropin A and LL-37 on DNA-ribosome segregation.

Using two-color fluorescence imaging, we show that Cecropin A destroyed nucleoid-ribosome segregation within 20 min of permeabilization of the *E. coli* cytoplasmic membrane,

reminiscent of the long term effects of the drug Rifampin. In contrast, LL-37, while similar to Cecropin A in length, charge and the ability to permeabilize bacterial membranes, had no observable effect on the nucleoid-ribosome segregation.

Results

Cecropin A and LL-37 are similar in length (37 amino acids), charge (+7) and exist as amphipathic α-helices on binding to lipid bilayers[4,5]. We previously reported the sequence of events involved in the membrane permeabilization and growth inhibition caused by these peptides[6] (Chapter 2). In earlier work[7], we carried out time-lapse imaging on single *E. coli* cells that transport green fluorescent protein (GFP) to the periplasm via the twin arginine translocation pathway. Both peptides first permeabilize the outer membrane (OM) to periplasmic GFP and subsequently permeabilize the cytoplasmic membrane (CM) to SYTOX Green[6,7]. Cell growth halts and cells shrink at the same time as the OM permeabilization event. Although membrane permeabilization is a major step in the mechanism of action of these AMPs, the post-permeabilization effects on the DNA, ribosome and other cytosolic components have not been studied.

In each cell, SYTOX Orange stained the nucleoids and S2-YFP expressed from the chromosome labeled all copies of the 30S ribosomal subunit. The long maturation time of YFP ensures that all S2-YFP copies are incorporated into 30S subunits[2]. The 30S subunits may occur as free 30S or as complete 70S ribosomes, most often members of a "polysome," a chain of 70S ribosomes translating the same message. The two-color fluorescence plus phase-contrast imaging scheme provided interleaved images of DNA, ribosomes, and cell dimensions over some 40 min with a 9-s cycle time.

The time-lapse series in Figures 1A and 1B shows images of a single representative cell following injection of 400 μl of 2 μM Cecropin A into the observation chamber (four times the MIC) at t = 0 min. Prior to Cecropin A injection (t = −4.5 min), the cell images and line scans

show normal DNA-ribosome segregation. At t = ∼4 min after injection, growth halts and the cell length (L_{cell}) shrinks abruptly by ∼10%. This is shown quantitatively in the $L_{cell}(t)$ curve in Figure 2A. Shortly after the shrinkage event, the nucleoid lobes and ribosome-rich regions begin to merge, as seen most clearly in the false-color images at t = 13.5 and 31.5 min. Eventually, the DNA and ribosomes mix almost completely; see the images and line scans at t = 38.5 min. Similar behavior was observed for all 22 cells in the field of view.

Treatment of cells with 8 μM LL-37 (eight times the MIC) causes cell shrinkage within 2.0 min after injection (Figures 1C and 1D; also Figure 2B). In contrast to Cecropin A, LL-37 treatment does not subsequently affect the spatial segregation of the nucleoid lobes and ribosome-rich regions, even 35 min after cells have stopped growing. Axial line scans (Figure 1D) of the fluorescence images at 13.5 min and 38.5 min continue to exhibit well-separated peaks corresponding to the DNA-rich and ribosome-rich regions. Normal segregation persists.

Discussion

Our initial application demonstrated that the antimicrobial peptide Cecropin A gradually causes mixing of DNA and ribosomes over tens of minutes after the abrupt cell shrinkage event and the halting of growth. In sharp contrast, LL-37 causes no such mixing. The underlying cause of these intriguingly different behaviors deserves further investigation. On similar timescales, certain antibacterial drugs are also known to alter nucleoid morphology, either expanding the nucleoid (e.g., rifampin) or contracting it (e.g., chloramphenicol)[8,9]. The underlying mechanisms are again not well understood. It is possible that certain drugs and AMPs may displace nucleoid-associated proteins whose binding to DNA contributes to DNA compactness in normal conditions. We also wonder if 30S and 50S monomeric ribosomal subunits may mix freely with the nucleoids, while 70S polysomes cannot mix due to excluded volume/entropy effects[3]. That idea is consistent with the contrasting effects of chloramphenicol (which freezes ribosomes on the mRNA) and rifampin (which prevents transcription initiation, eventually causing 70S to dissociate). In the future, single-molecule studies of the diffusive properties of ribosomes and DNA binding proteins before and after treatment with drugs and AMPs will shed additional light on these phenomena.

Methods

To enable simultaneous imaging of DNA and ribosomes, we used strain AFS55, which expresses the ribosomal protein S2-YFP from the chromosome. Cell cultures were grown overnight in EZ rich defined medium (EZRDM; Teknova)[10] with shaking in a 30°C water bath. We subsequently made subcultures by diluting the stationary-phase culture at least 1:100 into 2 ml of fresh EZRDM. When cells had grown to mid-log phase (optical density at 600 nm [OD_{600}] = 0.2 to 0.4 with 1-cm path length), SYTOX orange solution (50 μM stock concentration) was added to a final concentration of 500 nM. After 10 min of incubation, the cells were centrifuged twice at 8,000 × *g* for 2 min and resuspended in fresh EZRDM, after which 500 μl of cell culture was injected into the microfluidics chamber. The microfluidics chamber is made of polydimethylsiloxane (PDMS) adhered to a glass coverslip. It provides a simple rectilinear observation volume of the dimensions 11 mm by 6 mm by 50 μm (length by width by height), with inlet and outlet ports to enable flow. The preassembled microfluidics chamber was brought into contact with the microscope objective and warmed to 30°C before injection of the cells for imaging.

Once sufficient cell density was observed in a field of view, the remaining culture was rinsed with 1 ml of fresh, warmed, aerated growth medium. The rinsing steps eliminate background fluorescence from dye molecules that adhere to the coverslip without removing SYTOX Orange from the cytoplasm. This SYTOX Orange concentration and incubation time provide bright staining of the nucleoids, enabling at least 500 high-quality DNA snapshots without extensive photobleaching.

The 30S subunits were imaged using 488-nm excitation and a 525/50 emission filter. The spatial distribution of SYTOX Orange was monitored using 561-nm laser excitation (CrystaLaser, Reno, NV) of an intensity of 5 to 10 W/cm^2 at the sample. The SYTOX Orange fluorescence was collected through a bandpass filter (bright line 617/73-25; Semrock). Phase-contrast images were used to monitor cell length versus time. The imaging sequence consisted of interleaved pulses of 488 nm (30S ribosomal subunits), 561 nm (DNA stained by SYTOX Orange), and phase contrast (to obtain the cell outline). The exposure time for each light pulse was 50 ms and consecutive pulses were spaced by 3 s, resulting in a total cycle time of 9 s. Cells were treated with antimicrobial peptides at t = 4.5 min after the start of image acquisition. The total observation time was 45 min (300 imaging cycles). Additional details are provided elsewhere[6,7]. Post-acquisition, the interleaved snapshots were separated into the three respective channels for image analysis.

References

(1) Bakshi, S., Choi, H., Rangarajan, N., Barns, K. J., Bratton, B. P., and Weisshaar, J. C. (2014) Nonperturbative Imaging of Nucleoid Morphology in Live Bacterial Cells during an Antimicrobial Peptide Attack. *Appl. Environ. Microbiol. 80*, 4977–4986.

(2) Bakshi, S., Siryaporn, A., Goulian, M., and Weisshaar, J. C. (2012) Superresolution imaging of ribosomes and RNA polymerase in live Escherichia coli cells. *Mol. Microbiol. 85*, 21–38.

(3) Mondal, J., Bratton, B. P., Li, Y., Yethiraj, A., and Weisshaar, J. C. (2011) Entropy-Based Mechanism of Ribosome-Nucleoid Segregation in E. coli Cells. *Biophys. J. 100*, 2605–2613.

(4) Oren, Z., Lerman, J. C., Gudmundsson, G. H., Agerberth, B., and Shai, Y. (1999) Structure and organization of the human antimicrobial peptide LL-37 in phospholipid membranes: relevance to the molecular basis for its non-cell-selective activity. *Biochem. J. 341*, 501–513.

(5) Silvestro, L., and Axelsen, P. H. (2000) Membrane-Induced Folding of Cecropin A. *Biophys. J. 79*, 1465–1477.

(6) Rangarajan, N., Bakshi, S., and Weisshaar, J. C. (2013) Localized Permeabilization of E. coli Membranes by the Antimicrobial Peptide Cecropin A. *Biochemistry (Mosc.) 52*, 6584–6594.

(7) Sochacki, K. A., Barns, K. J., Bucki, R., and Weisshaar, J. C. (2011) Real-time attack on single Escherichia coli cells by the human antimicrobial peptide LL-37. *Proc. Natl. Acad. Sci. 108*, E77–E81.

(8) Cabrera, J. E., Cagliero, C., Quan, S., Squires, C. L., and Jin, D. J. (2009) Active Transcription of rRNA Operons Condenses the Nucleoid in Escherichia coli: Examining the Effect of Transcription on Nucleoid Structure in the Absence of Transertion. *J. Bacteriol. 191*, 4180–4185.

(9) van Helvoort, J. M. L. M., and Woldringh, C. L. (1994) Nucleoid partitioning in Escherichia coli during steady-state growth and upon recovery from chloramphenicol treatment. *Mol. Microbiol. 13*, 577–583.

(10) Neidhardt, F. C., Bloch, P. L., and Smith, D. F. (1974) Culture Medium for Enterobacteria. *J. Bacteriol. 119*, 736–747.

Figure 1: Phase-contrast and two-color fluorescence images of a representative *E. coli* cell before and after treatment with antimicrobial peptides. DNA is stained with SYTOX Orange, and 30S ribosomal subunits are labeled with an S2-YFP construct. (A and B) At t = 0 min, Cecropin A is injected at 2 μM, four times the MIC. Nucleoid expansion and DNA-ribosome mixing occur over tens of minutes after cell shrinkage, as shown by false-color images (left) and axial intensity line scans (right). (C and D) At t = 0 min, LL-37 is injected at 8 μM, eight times the MIC. DNA-ribosome segregation is maintained over the following 35 min. See the text for further details.

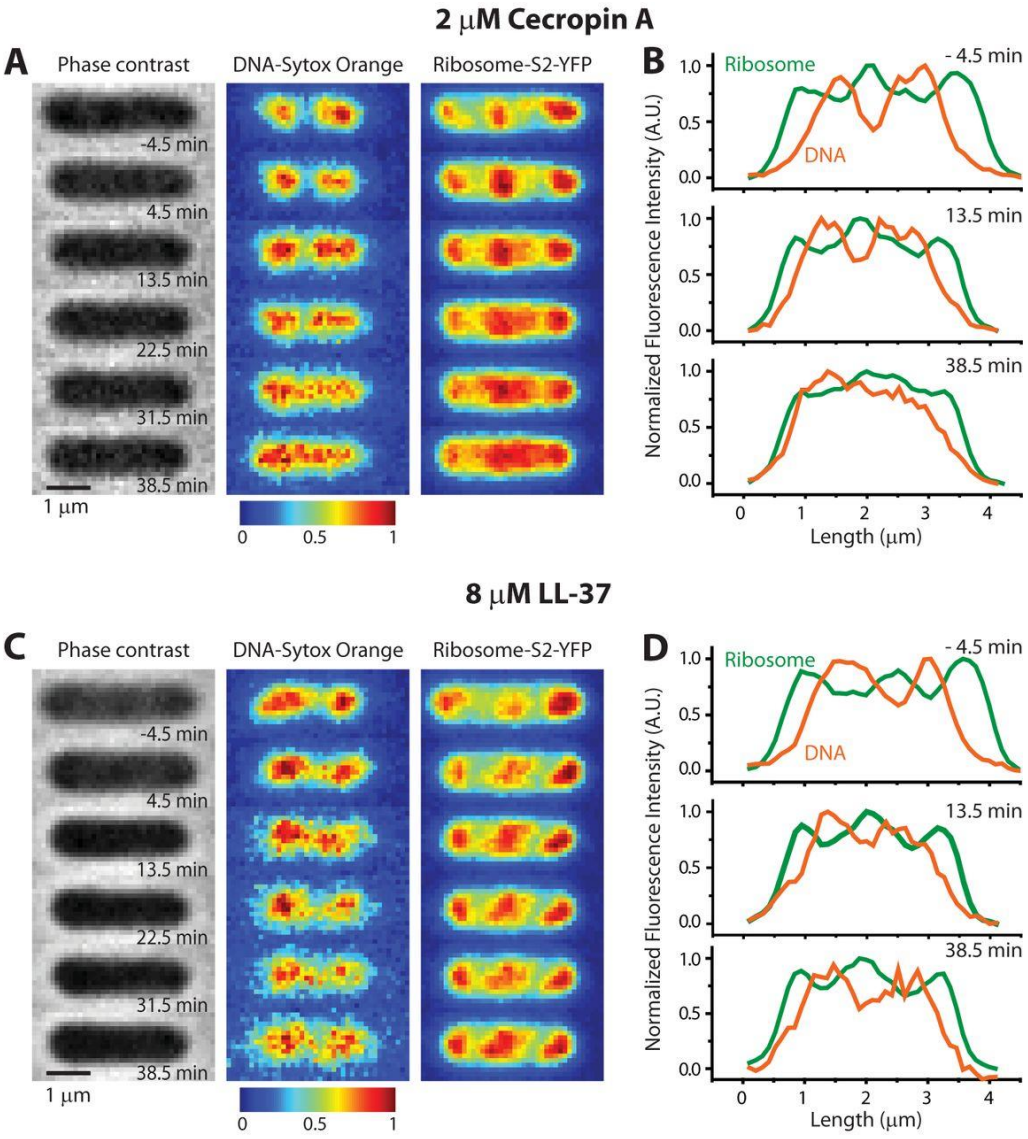

Figure 2: Plots of cell length vs time (derived from phase contrast images) for the single E. coli cells whose images are shown in Fig. 7 of the main text. (A) Injection of 2 μM of Cecropin A at t = 0 leads to abrupt cell shrinkage and halting of growth at t= 4 min. (B) Injection of 8 μM of LL-37 causes more gradual shrinkage beginning at t = 2 min.

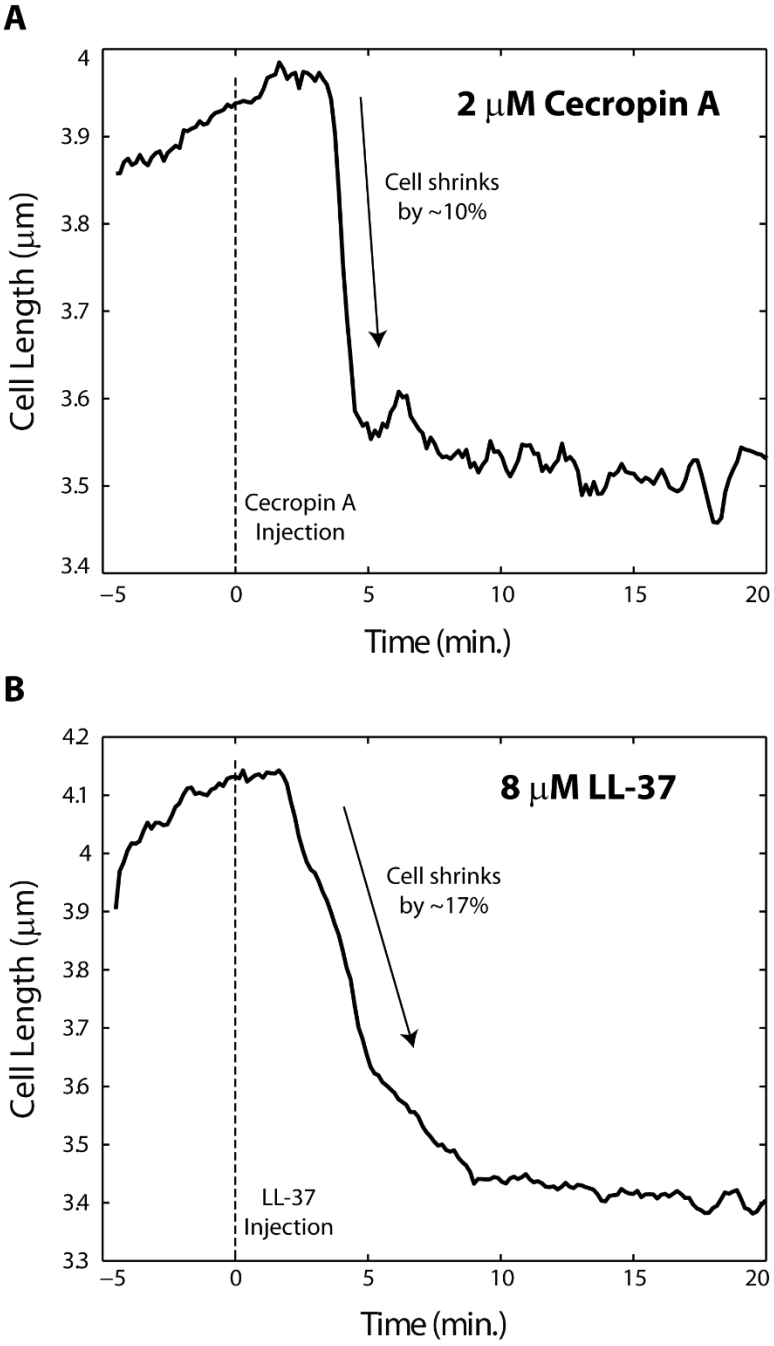

APPENDIX 2

Watching antimicrobial action in live bacteria

(Prepared for the WISL Award for Communicating Graduate Chemistry Research to the Public)

There's no better learning than that acquired via questions and answers. Through a Q&A format, this chapter aims to provide a brief overview of my graduate work to the general public. I am grateful to the Wisconsin Initiative for Science Literacy for giving me this opportunity to connect with a broader audience.

Q1. Can you describe the aim of your thesis in one sentence?

In my graduate work, I have developed a detailed understanding of how a particular class of antibiotics (Antimicrobial Peptides or AMPs) kills live bacterial cells.

Q2. What are antibiotics and why do we need to study them?

Think of the last time you were running a temperature and visited a clinic. Part of the diagnosis would have been to figure out whether you had a bacterial infection. If so, the doctor would have prescribed an antibiotic dose for 3-7 days.

Antibiotics are "wonder drugs" that have been used to treat bacterial infections since the 1940s. Penicillin, arguably the most popular antibiotic, was serendipitously discovered in 1928 by Alexander Fleming, a Professor of Bacteriology at St. Mary's Hospital in London. On returning from a vacation, Fleming was sorting bacterial samples, which were streaked out on petridishes containing bacterial food. He noticed that one of the petridishes had a mold growing on it, and the zone immediately surrounding the mold was cleared of all bacterial growth. Apparently, some substance secreted by the mold had inhibited bacterial growth in its vicinity.

Subsequent research performed by Howard Florey, Ernst Chain and their colleagues at Oxford University converted this research curiosity into a life-saving drug!

Over the past seventy years, several new antibiotics have been introduced in clinical use. These have undoubtedly contributed to global health and well-being. However, prolonged and excessive use of antibiotics has allowed disease-causing bacteria to adapt in several ways. These 'improved' bacterial strains are now able to resist the same antibiotic treatments. Infections caused by 'antibiotic resistant' bacteria are one of the leading causes of sickness and death today. The CDC (Centers for Disease Control and Prevention) estimated that more than 2 million infections were caused in 2013 in the U.S.A., out of which 20,000 cases were fatal. Some prominent pathogenic bacteria are MRSA (Methicillin Resistant *Staphylococcus Aureus*), C. Diff. (*Clostridium Difficile*) and *Acinetobacter*. Particularly alarming are bacteria that resist all known antibiotic treatments – these 'superbugs' are virtually impossible to kill.

There is a constant tug-of-war between bacteria and antibiotics being played out in our hospitals and health-care facilities. Quite frankly, the bacteria are winning this hands down! Within only a few years of a drug being introduced in the market, bacteria are able to adapt and render it ineffective. To add to the problem, no new families of antibiotics have been approved by the FDA over the last two decades.

Q3. Why are Antimicrobial Peptides (AMPs) important?

As is clear from the answer to Q2, there is a pressing need for novel, potent antibiotics that work against all kinds of bacteria. This is where Antimicrobial peptides (AMPs) are hypothesized to play a crucial role. AMPs are part of our immune systems – they are present on

our skin, in our saliva, tears and in white blood cells. AMPs help us fight infections by directly killing invading bacteria, and my signaling our immune systems to start working! They were first discovered in the 1970s. Today, more than 2500 natural AMPs are known, with varying structures, lengths and sequences. Some AMPs are shown in Figure 1. Almost every organism has one of these 'natural' antibiotics.

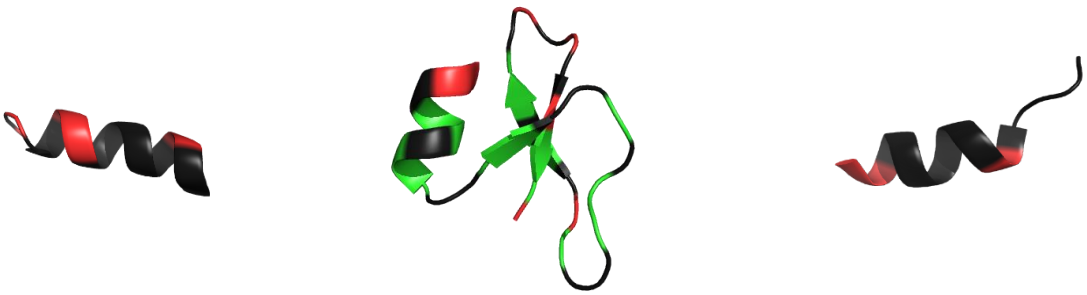

Figure 1: Structures of various AMPs. From left to right, CM-15 (hybrid, synthetic AMP), Human Beta Defensin-1 (human AMP) and Indolicidin (bovine AMP). The colors represent amino acid residues that are hydrophobic, polar or charged.

Conventional antibiotics bind to specific target molecules on the bacterial cell surface. Resistant bacteria have evolved to produce a slight different version of such target molecules that does not interact with antibiotics. This way, drugs cannot interact with bacteria and are, therefore, rendered ineffective. AMPs evade bacterial resistance because they do not have a specific target molecule on the cell surface. Instead, they bind generally to the cell wall, which consists of a mixture of layers of fats and sugar molecules. Evidently, changing the composition of the entire cell wall is a more difficult challenge for bacteria, than changing a single target molecule. Due to this, AMPs are considered as potential candidates for developing the next generation of antibiotics. Research on AMPs has accelerated over the past two or three decades.

Currently, there are only about ten AMPs in various stages of clinical trials. To improve our understanding of how AMPs work, the Weisshaar group observes their action on live bacteria using high-end scientific microscopes and related techniques.

Q4. Which type of bacteria did you study?

In my experiments, I studied the model bacterium *Escherichia coli* (*E. coli*). Our group has worked with this bacterium for several years. It is one of the most well understood species of bacteria. It was recently in the news due to an outbreak of the pathogenic strain *E. coli* O157:H7. Thankfully (!), I worked with a non-pathogenic laboratory strain, *E. coli* MG1655 and its variants. The *E. coli* cell is rod-shaped, ~3-5 µm in length and ~1 µm in diameter.

Q5. What are the major findings of your work?

We observed that AMPs kill bacteria by permeabilizing their cell membranes and halting cell growth. The AMPs preferably targeted actively dividing cells over non-dividing cells. We also observed that the membranes were permeabilized in very specific regions – close to the division plane and near the cell poles. The effects of AMPs were persistent, and once the membranes are permeabilized, cells do not recover even after the AMPs were rinsed out.

We studied AMPs that are naturally present in humans and insects (moths). We also worked with synthetic peptide and polymer analogs that were engineered to mimic natural AMPs. In our experience, each AMP causes a unique set of antimicrobial events in bacteria. There is lot of variation in the cellular responses. Using our powerful assays, we observed these various events in real time and developed a detailed understanding of antimicrobial action.

All AMPs studied in this work permeabilized the cell membranes. Some AMPs also caused additional secondary effects, such as disruption of the way DNA is wound up inside the cell. We are slowly beginning to understand that AMPs might be targeting multiple cellular processes simultaneously. And this could explain why bacteria find it harder to outsmart AMPs than conventional antibiotics, which typically have a single target.

Q6. What method did you use for your experiments?

We live-cell videography to observe the effects of AMPs on single *E. coli* cells. To characterize AMP action, we developed various assays to study membrane permeabilization, effect on cell growth, and perturbation of intracellular molecules such as the DNA.

Q7. What is the advantage of using the method over others?

Several other groups study AMP action on bacteria. However, most of them use methods that give an output signal that is averaged over all the cells in the tube (likely millions or billions of cells). This way, the diverse behavior of the various cells are blurred out. By now, we know that no two cells are identical, even those that have the same DNA! Therefore, it is likely that no two cells behave in an identical manner. It is thought that this cell-to-cell variation may be crucial to our understanding of how diseases such as cancer progress over time. Therefore, it is crucial to develop methods to watch individual cells separately. Our single-cell videography methods provide this advantage over other techniques.

Although many research groups use such single-cell imaging approaches, only a handful of them study antimicrobial action. To our knowledge, there are less than ten laboratories in the world that are studying AMPs using single-cell imaging.

Q8. What kind of microscope did you use?

Our research group assembled a microscope in-house over several years. We purchased most of the parts from various companies and built some accessories in a machine shop in our department. Briefly, the instrument consists of the following parts:

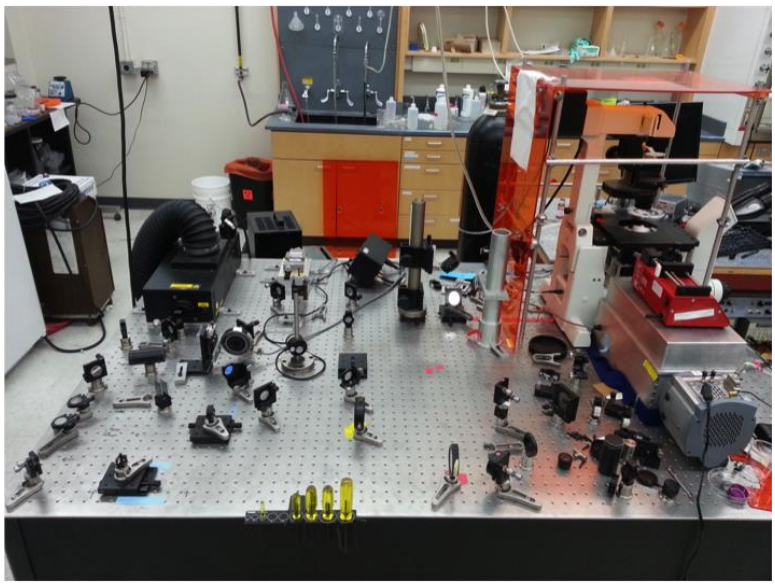

Figure 2: A picture of the microscope setup used in this thesis. In the foreground, several mirrors and lenses are arranged to direct laser beams onto the sample. The black box on the table (top left) is a laser. The eye-piece and microscope stage can be seen on top right. The gray box close to bottom right is a high-end camera.

Microscope: Part of the instrument looks similar to a table-top microscope that you may have used in high school biology laboratories. However, our setup was equipped with an optics table (Figure 2) that consists of a maze of mirrors, lenses, shutters, lasers… even a periscope! All

these widgets help to shape the path of laser beams onto the sample. The microscope is fitted with objective lenses that were selected based on their light-bending properties. Various terms used to describe details of these lenses are similar to those used for modern digital cameras (such as numerical aperture, working distance and depth of field). The whole table is floating on Nitrogen gas! This insulates the optics from any vibrations that get transmitted through the walls or floor of the building.

Camera: Our microscope is fitted with a high-end, ultra-sensitive scientific camera designed specifically to acquire images at very high frame rate. It is similar to the latest point-and-shoot cameras that you may have used to click photos, only much faster and more sensitive. The camera is connected to a computer, and operated with a software. We can save images and movies, to be watched and analyzed later.

Flow chamber. We plate live bacteria on a glass slide. The slide is part of a small chamber through which we can flow solutions containing ‘bacterial food’! We can also control the temperature of the solutions and chamber. Together, this helps to keep the bacteria alive and happy. When it is time to begin the experiment, we start flowing a solution of the AMP and watch how cells respond.

Q9. Can AMPs become marketable drugs one day?

This remains to be seen. There are no AMPs currently being used clinically. (Colistin, also known as Polymyxin E, is the closest candidate. It is a peptide-based antibiotic that has been used to treat certain bacterial infections. However, a major part of its structure is made up of

lipids, so it is not included in the larger family of AMPs). There are about ten AMP candidates in various stages of clinical trials. However, more research is needed to understand the detailed effects of AMPs. We currently do not know the steps adopted by AMPs to permeabilized membranes, how many AMP molecules are needed to kill a bacterial cell, how bacteria could develop resistance against AMPs, and how the structure of AMPs decides their function. Research directed to answer these and several other open questions will undoubtedly contribute to realizing the eventual goal of developing potent, AMP-based antibiotics.

Q10. Overall, how would you describe your graduate research experience?

Graduate research has been fun and challenging. I really enjoyed the basic experimental procedure in lab - observing live cells, shooting movies, playing the movies back, analyzing them and trying to make sense of the data. To me, this was a great way to spend my work day! Making actual progress in my research was a lot more difficult than I had initially imagined. Living cells are inherently diverse, and give varied responses under the same set of conditions. Therefore, being able to reproduce observed trends was also quite challenging. I was fortunate to get great mentorship from my advisor, and a lot of help from my colleagues in the group. Useful collaborations with other research groups also significantly contributed to the progress that I could make towards my project.

Overall, graduate research has been an inspiring, rewarding experience!